UNIVERSITY OF MODENA AND REGGIO EMILIA

Engineering Department "ENZO FERRARI"

---

Ph. D. School "High Mechanics and Automotive Design and Technology"

*Simulation methods and mechanical design - XXVII Cycle*

Ph. D. School Director: Prof. Eng. Paolo Tartarini

# SIMULATION OF ATMOSPHERIC DISPERSION OF POLLUTANT EMISSIONS FROM A TRI-GENERATION POWER PLANT BY MEANS OF A LAGRANGIAN PARTICLE DISPERSION MODEL

Tutor:

Prof. Grazia Ghermandi

Co-tutor:

Eng. Alessandro Bigi

Candidate:

Marco Michele Zaccanti

---

Academic year 2014 / 2015

# *Simulation of atmospheric dispersion of pollutant emissions from a tri-generation power plant by means of a Lagrangian Particle Dispersion Model*

*Simulazione della dispersione atmosferica delle emissioni da un impianto di tri-generazione con l'ausilio di un modello Lagrangiano a particelle.*

# Index

# Abstract

Aim of this work is the air quality impact assessment of atmospheric pollutant emissions from a tri-generation power plant through the simulation of the airborne pollutant dispersion phenomena by means of a Lagrangian Particle Dispersion Model. The facility consists of an internal combustion four-stroke engine, powered by methane gas, and heat recovery equipments. Electrical power is 3349 kWe, thermal power 3098 kWt; electric efficiency is equal to 44.2 %, thermal efficiency 40.9 %. The power plant is designed to meet the electric and thermal energy demand of Modena General Hospital. The city of Modena lies in Northern Italy, in the central Po Valley, and the plant is located within a densely populated urban area, which is mainly affected by pollutant emissions from vehicular traffic, industrial plants and household heating systems.

In the study area, where atmospheric pollution is already of public concern, air quality is affected by recurrent calm winds and thermal inversion events leading to pollutant build-up.

Pollutant dispersion was investigated by means of the software package ARIA INDUSTRY (Arianet Ltd, Milano, Italy) featuring the Lagrangian Particle Dispersion Model SPRAY, since it is able to perform reliable simulations of atmospheric dispersion in a complex topography under critical and non-stationary atmospheric conditions, e.g. during low or calm wind.

Simulations of pollutant dispersion were performed on both a local and a micro-scale spatial domain and focused on the urban air quality impacts of pollutant emissions in the surroundings of the power plant. Micro-scale simulations were performed by Micro-SPRAY model, an advanced version of SPRAY model, which is able to take into account the urban canopy effects due to the presence of buildings. Simulation results were presented in graphical form through spatial concentration maps: they mainly deal with $NO_x$ dispersion, being $NO_x$ the most critical pollutant emission from a methane-fuelled power plant. Moreover, $NO_x$ concentration in urban areas may be frequently close or higher than regulatory limit due to the co-presence of several pollutant sources. Simulated concentrations where compared with experimental observations within the urban air quality network of the Regional Environmental Protection Agency (ARPA). The comparison showed a remarkable reliability of the model to reproduce pollutant concentration fields in an urban canopy even under critical atmospheric conditions.

**Keywords**: airborne pollutant dispersion, power-plant emissions, SPRAY model, urban canopy, air quality data.

# Sommario

La ricerca riguarda lo studio d'impatto sulla qualità dell'aria delle emissioni in atmosfera da un impianto di trigenerazione mediante l'uso di un modello lagrangiano per la simulazione della dispersione degli inquinanti atmosferici. L'impianto è costituito da un motore a combustione interna a quattro tempi Jenbacher JMS 620 GS-N.L, alimentato a gas metano, e dai sistemi di recupero termico. La potenza elettrica erogata è pari a 3349 kWe, mentre la potenza termica recuperata è pari a 3098 kWt; l'efficienza elettrica è pari al 44.2 %, quella del recupero termico è pari al 40.9 %. L'impianto è installato presso l'ospedale Policlinico di Modena, città della Pianura Padana centrale, in area urbana densamente popolata e interessata dalla copresenza di diverse sorgenti inquinanti: traffico veicolare, riscaldamento domestico e impianti industriali. Il contesto, assai sensibile all'inquinamento atmosferico, è reso ancor più critico dalle condizioni meteorologiche ricorrenti, quali calme di vento e fenomeni d'inversione termica, che non favoriscono la dispersione degli inquinanti atmosferici. Nelle simulazioni è stato utilizzato il modello lagrangiano a particelle SPRAY, contenuto nella suite modellistica ARIA INDUSTRY sviluppata da Arianet s.r.l., poiché è in grado di simulare, con buona approssimazione, i fenomeni dispersivi in condizioni atmosferiche critiche (non stazionarie), con venti deboli o calma di vento, e in presenza di terreno complesso.
Le simulazioni di dispersione degli inquinanti sono state condotte sia su un dominio spaziale a scala locale che a micro-scala, focalizzando l'attenzione dello studio agli impatti sulla qualità dell'aria urbana nella zona adiacente all'impianto. Per le simulazioni a micro-scala è stata impiegata la versione avanzata del modello, Micro-SPRAY, in grado di riprodurre gli effetti dovuti alla presenza degli edifici (canopy urbana) sulla dispersione degli inquinanti. I risultati delle simulazioni sono stati presentati in forma grafica attraverso mappe spaziali di concentrazione: è stata studiata principalmente la dispersione di $NO_x$, trattandosi dell'inquinante più critico per le emissioni di un impianto alimentato a metano rispetto alla qualità dell'aria urbana, ove gli ossidi di azoto possono raggiungere valori prossimi ai limiti di legge causa la copresenza di sorgenti emettitrici.
Si è inoltre provveduto al confronto dei medesimi risultati con le concentrazioni di $NO_x$ atmosferico misurate sperimentalmente da ARPA attraverso le stazioni di monitoraggio per la qualità dell'aria urbana. Il confronto ha evidenziato una notevole affidabilità del modello nel riprodurre i campi di concentrazione anche in condizioni atmosferiche complesse e alla presenza di ostacoli urbani.

***Parole chiave***: dispersione in atmosfera, emissioni inquinanti, modello di dispersione SPRAY, canopy urbana, dati di qualità dell'aria.

# Chapter 1

# *Numerical air pollution modelling*

## 1.1 Introduction

Numerical modelling for atmospheric pollutant dispersion is a key issue for air quality assessment and management. The purpose of these models is to describe the behaviour of pollutant species released into the atmospheric environment by human activities: industry, energy production and vehicular traffic. Some of the most important air pollutant species dealing with anthropogenic sources are nitrogen oxides ($NO_x$), sulphur oxides ($SO_x$), particular matter (e.g. PM10, PM 2.5) and volatile organic compounds (VOC), which may result toxic or dangerous for natural ecosystems and human health.

Investigation of fate of pollutant emissions in the atmosphere is extremely complex, since it depends both on dispersion properties of atmosphere and physical and chemical processes. Pollutants are not only dispersed by wind and turbulence, but they can undergo chemical reactions, wet or dry deposition or removal by rainfall (rainout).

The growing public awareness towards atmospheric pollution issues has lately led to more severe air quality limits and environmental regulations. Hence, air quality models can give a great support for policies of atmospheric pollution mitigation in urban environment. Furthermore, according to the European Directive on air quality (E.U., 2008), "modelling techniques should be applied to enable point data to be interpreted in terms of geographical distribution of concentration".

Airborne pollutant dispersion is simulated on several spatial domains depending on the aim of the study. *Local scale* simulations are widely used to assess the contributions to air pollution from different anthropogenic sources, mainly vehicular traffic, industrial areas, power-plants, that are co-present on the simulation domain (from 10 km up to 100 km). Larger spatial domains are involved in *mesoscale* simulations (100-1000 km) and *synoptical* scale simulations (over 1000 km).

Simulation period for local scale models usually spans over at least a monthly period, in order to investigate the evolution of pollution scenarios in different meteorological conditions according to seasonality; otherwise short-term simulations, aimed at studying accidental pollutant releases, span over a daily or hourly period.

Due to the increasing attention on the relationship between atmospheric pollution and emissions within urban environment, innovations on modelling techniques have recently focused on urban micro-scale simulation of pollutant dispersion. The aim is to simulate dispersion phenomena within the lowest atmospheric layers in urban environment, where pollutant behaviour is mainly affected by urban canopy, i.e. the presence of building obstacles, rather than synoptic meteorological circulation. Building geometry and arrangement can give rise to turbulent eddies, especially in the narrow zones among building facades, namely urban canyons (Oke, 1987), where pollutant removal is inhibited and high pollutant concentration values are consequently expected. Such phenomena are appreciable only with a high-resolution model that takes into account the building presence. Simulation period for micro-scale models generally spans over hourly or daily time lapse, since the aim of the study is not to reproduce a common ordinary situation, but a particular and intensive pollution event due to the combination of several factors: meteorological conditions, turbulence recirculation because of urban canopy and high pollutant emissions.

Atmospheric dispersion models require meteorology, turbulence, ground elevation data, land-use, land-cover dataset, source type and pollutant emissions as input data. Meteorological databases by Local Meteorological Agencies are widely used as a reliable data source for temperature, wind speed and wind direction values, which usually come from ground experimental measurements or radio sounding profiles, mesoscale vertical wind profiles and mixing height.

Turbulent fields deeply affect pollutant dispersion, especially when low wind conditions occur. The atmospheric turbulence is quite a complex topic to be investigated, due to the multitude of features that can give rise to turbulent eddies: sensible heat exchange between ground surface and atmosphere, topography, land-use and land-surface, urban canopy. Different parameterizations were developed to simulate turbulence effects in air quality models; input data require specific parameters to be externally computed with atmospheric turbulence processors.

Ground elevation, land-use, land-surface cover data are usually provided by remote sensing images, e.g. European CORINE Land Cover 2000 dataset by European Environment Agency (EEA, 2015a).

Emission data mainly consist of pollutant emission rate, temperature of the emitted gas flow and physical or chemical parameters dealing with the pollutant species in the exhaust gas flow. Pollutant emission rates can be estimated from emission inventories or collected by means of experimental measurements of the emitted exhaust gas flow.

## 1.2 Air quality models classification

The airborne pollutant dispersion is influenced by numerous features of the atmospheric environment, including meteorology, canopy, physical and chemical behaviour of the pollutant species. The evolution of pollutant concentration fields in space and time is predictable throughout a set of differential equations, in which all the previously mentioned aspects are taken into account with a reasonable approximation.

Air quality deterministic models are generally classified in *Eulerian* and *Lagrangian* models, according to the fluid dynamic approach in simulating pollutant transport in the atmosphere.

In the *Eulerian* air quality models pollutant transport is controlled by Navier-Stokes equations and *C=C(x,y,z)* is the steady state pollutant concentration field in a fixed Cartesian reference frame *Oxyz*. Among the Eulerian models, Analytical Gaussian models are the most commonly used to simulate the atmospheric dispersion of stack emissions (plumes). The mathematical solution for *C=C(x,y,z)* was proposed by Sutton (1947) for a continuous point pollutant source (Equation 1.1). According to Sutton operating conditions, *x* axis is oriented along the prevailing wind direction, i.e. along pollutant plume mean centreline, and the cross section of the plume shows a *Gaussian* pollutant concentration profile on the *y* and *z* directions, as shown in Figure 1.

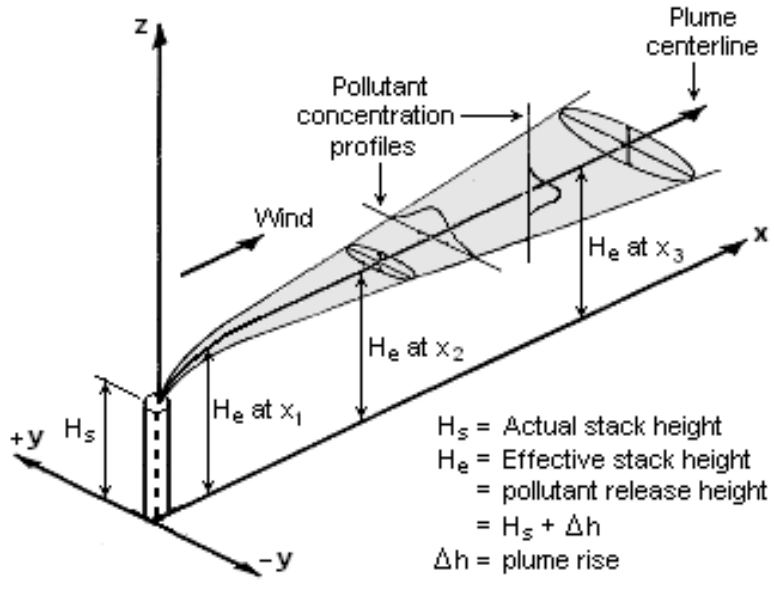


*Figure 1. Visualization of pollutant plume in Gaussian dispersion model.*

The following relation (Equation 1.1) gives pollutant concentration field surrounding the stack; the similarity with the Gaussian probability distribution, which is commonly used in statistics, is quite evident because of the exponential term.

$$C(x,y,z) = \frac{Q}{2u_h \pi \sigma_x \sigma_y} \exp\left[ -\frac{y^2}{2\sigma_y^2} - \frac{(z - H_e)^2}{2\sigma_z^2} \right] \quad (1.1)$$

In Equation 1.1 $H_e$ (m) is the *effective stack height*, i.e. the pollutant release height, above ground level (m), $\sigma_y$ and $\sigma_z$ (m) are respectively the *horizontal* and *vertical standard deviation* of the emission distribution, $u_h$ (m/s) is the *horizontal wind velocity* along the plume centreline and $Q$ is the *pollutant flow rate* in the point source. Being $Q$ a mass of a substance per unit of time it can be expressed as (kg/h), or (mg/s), or (μg/s), according to the mass flow rate for a given pollutant specie. Thus, pollutant concentration field $C = C(x,y,z)$, which is expressed as mass per unit of volume, is measured in (kg/m$^3$), or (mg/m$^3$), or (μg/m$^3$), according to the model outputs magnitude.

The meteorological data set of Eulerian Gaussian air quality models is generally limited, since only the wind speed value for the source point (0,0,$H_e$), which is assumed in steady state, is needed in Equation 1.1. The atmospheric turbulence is described by $\sigma_y$ and $\sigma_z$, which can be computed through semi-empirical laws obtained by several authors (Pasquill, 1961; Gifford, 1961; Turner, 1967; Briggs, 1973; Green, 1980), according to atmospheric stability.

Eulerian Gaussian models are suitable to describe pollutant behaviour in steady wind conditions and weak vertical mixing of the air; their main limitation is the coarse approach to the description of atmospheric turbulence. The Gaussian formulation lacks of precision in simulating pollutant dispersion in low-wind and calm conditions and in presence of thermal inversion in the atmosphere. Moreover, the pollutant concentration field is not satisfactory simulated close to the source and more than 10 km away from it. Therefore, the Eulerian Gaussian models are only suitable to describe average seasonal conditions without critical events.

On the other hand, according to the *Lagrangian* description, the moving fluid is divided in a multitude of small particles that move independently from one to each other following stochastic trajectories, and the reference frame moves with each particle. Hence, the airborne pollutant dispersion is simulated by dividing pollutant mass flow in a set of virtual particles, whose number is proportional to the mass flow, that move in the atmospheric environment. Particle emission from a given pollutant source occurs with a fixed time frequency and each particle is supposed to transport a fixed pollutant mass. Particle motion is described by a set of stochastic differential equations that take into account both mean wind and atmospheric turbulence fluctuations experienced by each particle along the trajectory.

Particle dimension is supposed to be suitably small so that, at a given point, differences between the pollutant particle motion and the turbulent flow can be overlooked; this is the basic hypothesis for

Lagrangian particle models formulation, well-known in the literature as the "Well mixed Criterion" (Thompson, 1987). The particles, however, are much larger than molecules, so that interactions among molecules are not taken into account in the particle motion equations. Since particles motion gradually follows the evolution of atmospheric conditions at any point of the trajectory, the concentration fields are rebuilt with a greater approximation than in Eulerian models, where the atmospheric transport can be simulated only in stationary atmospheric conditions. Thus Lagrangian Particle Dispersion Models are greatly reliable in simulating pollutant dispersion phenomena in highly complex meteorological conditions, i.e. low wind speed, thermal inversion and complex topography, where the contribution of mechanical and convective turbulence is often prevailing over wind transport.

Conversely, a correct and reliable reproduction of concentration fields requires high complex algorithms in order to take into account complex turbulence, with a considerable impact on computation time.

The behaviour of a given pollutant specie in the atmospheric environment involves also chemical and physical phenomena. Physical phenomena mainly consist of vertical deposition of particulate matter, which can be easily simulated assuming that pollutant concentration varies following a decay law. Conversely, chemical reactions leading to pollutant removal are quite difficult to be simulated, since particles contain a fixed quantity of each pollutant species, which is kept constant during the whole simulation period, and the molecular scale interactions are not accounted. According to the current state of the art, many different approaches to manage chemical reactions in Lagrangian Particle Models were proposed in the literature (Song *et al*., 2003; Ferrero and Alessandrini, 2009; Kaplan *et al*., 2014) with encouraging results.

## 1.3 Lagrangian Particle Dispersion Models formulation

The present section provides a brief description of the equation schemes for particle motion adopted by Lagrangian Particle Dispersion Models; attention will be focused on the general approach for atmospheric turbulence modelling. The basis assumption is that spatial and temporal evolution of turbulent field is affected by random fluctuations that cannot be adequately predicted through a deterministic approach. This implies that, starting with the same initial and boundary conditions, many different realization of turbulence field can be obtained due to random fluctuations.

According to Lagrangian approach, let us suppose that a certain number of pollutant particles have been emitted from a generic source. By following the Reynolds hypothesis for turbulence description (Reynolds, 1895), the velocity of a particle is divided in an average and a fluctuating stochastic part: the former corresponds to the mean velocity of the local wind; the latter depends on the statistical variables of turbulent flow.

Assuming that particle motion is defined according to a Cartesian reference frame *Oxyz*, particle position, at time *t* (s), is given by Equation 1.2:

$$\frac{dx_i(t)}{dt} = u_i = \bar{u}_i + u_i' \tag{1.2}$$

where $i = x, y, z$ indicates the *x*, *y* and *z* axes direction and $X(t) = [x_x(t), x_y(t), x_z(t)]$ (m) is the position of a given particle, at time *t*, with velocity vector $u(t) = [u_x(t), u_y(t), u_z(t)]$ (m/s). The Reynolds hypothesis leads to compute the generic component of particle velocity $u_i$ as the sum of a mean ($\bar{u}_i$) and a stochastic term ($u_i'$). Steady mean value, which is assumed constant over a fixed time lapse, equals the mean velocity of the local wind at any single point of particle trajectory.

Wind speed values, which are input data for the model, are structured in three-dimensional fields that are generally provided by an external meteorological model. The fluctuation term is the variation around the mean value due to the turbulent properties of the fluid motion.

The position of any single particle can be computed at discrete time steps ($\Delta t$) by means of Equation 1.3, where the fixed $\Delta t$ (s) is chosen by model user or by the model itself:

$$X(t+\Delta t) = X(t) + [\overline{u_i} + u_i'(t)]\Delta t \tag{1.3}$$

Many Lagrangian Particle Dispersion Models are based on the Brownian description for turbulent motion, which follows the Langevin equation for velocity fluctuation.

The general form of Langevin equation for random velocity term $u_i'$ has the following expression:

$$\frac{\partial u_i'(t)}{\partial t} = -\beta u_i'(t) + \alpha \tag{1.4}$$

The friction term $-\beta u_i'(t)$ ($s^{-1}$) deals with viscous interactions between particles and $\alpha$ (m/s) is a stochastic term depending on an incremental Wiener process. Following the Taylor approach to turbulence (Taylor, 1921), the deterministic coefficient can be computed by taking into account the historical evolution of particle velocity. Let $P(u_i,t)$ be the *probability density function*, i.e. $P(u_i,t)\cdot du_i$ is the probability that the value for the $u_i$ velocity component fall in the range among $u_i$ and $u_i + du_i$. The statistical correlation function $\rho_i(t, \tau)$ between random particle velocities at time $t$ and $t + \tau$, where $\tau$ is the elapsed time between two observations, is defined as in Equation 1.5 (Finzi, 2001):

$$\rho_i(t,\tau) = \frac{\overline{u_i'(t)u_i'(t+\tau)}}{\overline{u_i'^2(t)}} \tag{1.5}$$

By applying the average operation on the random velocity values $u_i'(t)$ and $u_i'(t + \tau)$, the resulting following terms are the statistical 2nd order moments, which depend on the probability $P(u_i,t)$:

- $\overline{u_i'^2(t)} = \int_{-\infty}^{\infty} P(u_i,t)u_i'^2(t)dt$ is the *variance* of the speed component $u_i'(t)$.
- $\overline{u_i'(t)u_i'(t+\tau)} = \int_{-\infty}^{\infty} P(u_i,t)u_i'(t)u_i'(t+\tau)dt$ is the *covariance* for the correlation among $u_i'(t)$ at time $t$, and $u_i'(t + \tau)$ at time $t + \tau$.

Values range for the correlation function is between 0 and 1. For $\rho_i(t,\tau) \to 0$ there is no correlation, and the velocity at time $t$ and $t + \tau$ are stand-alone. On the contrary, for $\rho_i(t,\tau) \to 1$, the two values are deeply correlated. It is worthwhile to remark that $i = x, y, z$ indicates the Cartesian coordinates in the *Oxyz* reference frame.

By applying the Taylor theory (in homogeneous and steady state conditions of the turbulence field) to Langevin equation, the term $\beta^{-1}$ is substituted with *Lagrangian time scale* $T_{Li}$ (s), which is defined as follows (Equation 1.6):

$$T_{Li} = \int_0^{\infty} \rho_i(\tau) d\tau \tag{1.6}$$

Experimental observations on turbulent motion have shown that the correlation function has the following exponential form (Equation 1.7):

$$\rho_i(\tau) = \exp\left(\frac{-\tau}{T_{Li}}\right) \tag{1.7}$$

The correlation among $u_i'(t)$ and $u_i'(t + \tau)$ becomes more significant when $\tau << T_{Li}$.
The first order Taylor series expansion for Equation 1.7 leads to Equation 1.8.

$$\rho_i(\tau) = \exp\left(\frac{-\tau}{T_{Li}}\right) \approx 1 - \frac{\tau}{T_{Li}} \tag{1.8}$$

The present scheme is applicable only under the quite simple and restrictive atmospheric turbulence conditions previously mentioned, i.e. homogeneous turbulent field and when probability density function $P(u_i, t)$ is supposed to be Gaussian.
Through the discretization of Equation 1.4, the general expression for the turbulent velocity $u_i'(t)$ is given by the following Equation 1.9, where both the position vector $X = X(t) = [x_x(t), x_y(t), x_z(t)]$ and the velocity vector $u = u(t)=[u_x(t), u_y(t), u_z(t)]$ appear.

$$du_j' = a_i(X,u)dt + b_{ij}(X,u)dW_j(t) \tag{1.9}$$

In Equation 1.9, $i$ , $j = x, y, z$; $a_i(X, u)dt$ (m/s) is a deterministic term; $b_{ij}(X, u)dW_i(t)$ (m/s) is a stochastic term and the quantity $dW_i(t)$ ($s^{-1/2}$) is the incremental Wiener process with average $0$ and variance $dt$. The *diffusion coefficient* $b_{ij} = \sqrt{C_0 \varepsilon}$ ($m/s^{1.5}$) (Monin and Yaglom, 1971; Du, 1997) describes the energy dissipation phenomenon due to the turbulence eddies according to the Kolmogorov theory for turbulence (1941). $C_0$ is a *universal empirical constant*, which is usually equal to 2, and $\varepsilon$ ($m^2/s^3$) is the *dissipation rate of turbulent kinetic energy*.
The deterministic term $a_i(X, u)$ depends on the probability density function of the turbulent velocity, $P(u_i, t)$. When $P(u_i, t)$ has *Gaussian* form the drift coefficient assumes the following general expression (Sozzi, 2003):

$$a_i(X,u) = -\left(\frac{C_0\varepsilon}{2\sigma_{ui}^2}\right)u_i'(t) + \frac{1}{2}\frac{\partial\sigma_{ui}^2}{\partial i}\cdot\left\{1+\frac{[u_i'(t)]^2}{\sigma_{ui}^2}\right\} \quad (\mathrm{m/s^2}) \tag{1.10}$$

In Eq. 1.10, the spatial derivatives take into account the non-homogeneity of turbulence field and $\sigma_{ui}$ is the variance of the speed component $u_i$.

It can be demonstrated (Tennekes, 1979) that Lagrangian time scales $T_{Li}$, with $i = x, y, z$, can be expressed as in Equation (1.11):

$$T_{Li} = \frac{2\sigma_{ui}^2}{C_0\varepsilon} \tag{1.11}$$

Through the substitution of Eq. 1.11 and 1.10 in Eq. 1.9 the general expressions for the horizontal components of the stochastic particle velocity in *Gaussian*, *stationary* and *non-homogeneous* turbulent conditions are expressed by Equations 1.12 and 1.13. When these equations are implemented in a Lagrangian particle model $\tau$ becomes the time step $\Delta t$ of integration.

$$u_x'(t+\Delta t) = \left(1-\frac{\Delta t}{T_{Lx}}\right)u_x'(t) + \frac{1}{2}\frac{\partial\sigma_{ux}^2}{\partial x_x}\cdot\left\{1+\frac{[u_x'(t)]^2}{\sigma_{ux}^2}\right\}\cdot\Delta t + u_x''(t)\sigma_{ux}\sqrt{2\frac{\Delta t}{T_{Lx}}} \tag{1.12}$$

$$u_y'(t+\Delta t) = \left(1-\frac{\Delta t}{T_{Ly}}\right)u_y'(t) + \frac{1}{2}\frac{\partial\sigma_{uy}^2}{\partial x_y}\cdot\left\{1+\frac{[u_y'(t)]^2}{\sigma_{uy}^2}\right\}\cdot\Delta t + u_y''(t)\sigma_{uy}\sqrt{2\frac{\Delta t}{T_{Ly}}} \tag{1.13}$$

where $u_x''$ and $u_y''$ are random, uncorrelated, velocity terms.

A Gaussian turbulence model commonly well approximates turbulence statistics for the horizontal components $u_x'$ and $u_y'$ in a wide range of atmospheric turbulence conditions (Equations 1.12 and 1.13). Nonetheless, for the vertical component $u_z'$, a Gaussian formulation for $P(u_z, t)$ is applicable only when high atmospheric stability occurs. It has been verified that under unstable conditions, due to the development of convective cells, the motion of the ascending and descending air eddies is characterized by inverted speeds because of the different thermal behaviour of ground surface (Figure 2, left). Thus, the statistical distribution for vertical speed is asymmetrical, as shown in Figure 2 (right), where $w^*$ (m/s) is the *convective scale velocity* that estimates the magnitude of convective turbulence under unstable conditions and which will be discussed in Chapter 3.

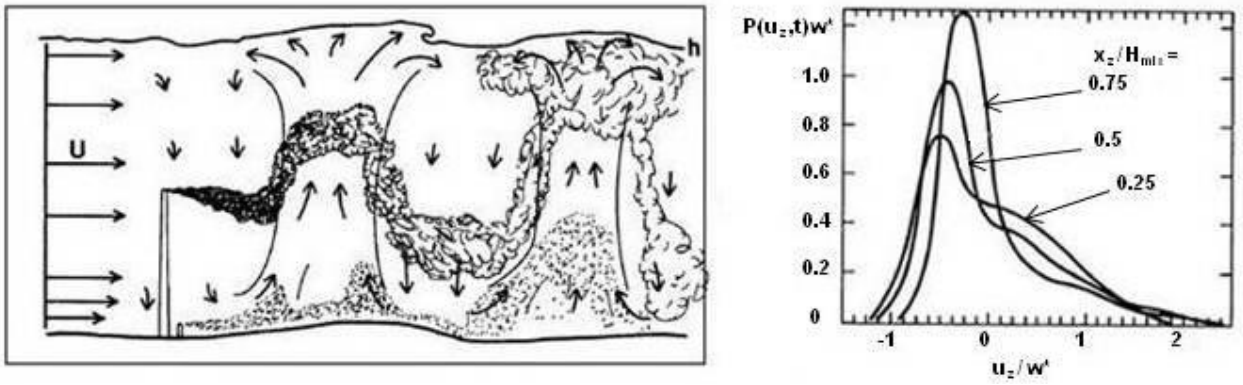


*Figure 2. Vertical ascending and descending motion for turbulence eddies under convective turbulent conditions (left); asymmetrical statistical distribution of vertical speed (right), according to the* $x_z/H_{mix}$ *ratio (*$H_{mix}$ *is the Mixed Layer Height, Chapter 3).*

In order to reproduce the asymmetrical distribution of vertical speed on unstable atmospheric conditions the $P(u_z, t)$ for $u_z'$ must be *non-Gaussian*; hence the third (skewness) and the fourth (kurtosis) order statistical moments must be taken into account to correctly describe convective situations. In the literature, several non-Gaussian statistical models have been proposed, for instance the *Bi-Gaussian* probability density function (Luhar and Britter, 1989; Weil, 1990; Anfossi *et al*., 1996), which is a combination of two Gaussian distributions. In addition, the *Gram-Charlier* series expansion (Anfossi *et al.*, 1997; Ferrero and Anfossi, 1998) provides an approximated polynomial expression for the $a_i(X, u)$ term up to the fourth or fifth order according to the order availability of statistical moments.

With the aim of applying Eq. 1.9 in *Gaussian* and *non-homogeneous* turbulence conditions for $u_x'$ and $u_y'$ (Eq. 1.12 and 1.13) and in *non-Gaussian* and *non-homogeneous* turbulence conditions for the $u_z'$ component (for instance with a *Gram-Charlier* series expansion for the $a_i(X, u)$ term), the statistical description of turbulence field is required. The involved statistical turbulence parameters consist of *Lagrangian time scales* $T_{Lx}$, $T_{Lv}$, $T_{Lz}$ and velocity variances $\sigma_{ux}$, $\sigma_{uy}$ and $\sigma_{uz}$. Such parameters horizontally vary according to complex topography and terrain land-use; furthermore, vertical profiles of such variables are strongly dependent on atmospheric stability conditions. Hence the calculation of turbulence statistics requires the two-dimensional fields of land-use data and turbulence scale variables $z_0$, $L$, $H_{mix}$, $w^*$, $u^*$ for PBL (see Chapter 3).

In the literature, many different schemes have been proposed for the calculation of vertical profiles $T_{Lx}(x_z)$, $T_{Ly}(x_z)$, $T_{Lz}(x_z)$, $\sigma_{ux}(x_z)$, $\sigma_{uy}(x_z)$ and $\sigma_{uz}(x_z)$ at a given point (Irwin, 1979; Nieuwstadt, 1980, Hanna 1982; Irwin 1983; Hanna and Chang, 1991).

The simulation of pollutant dispersion in the present study were all accomplished with the Lagrangian Particle Dispersion Model SPRAY, which is developed by Arianet Ltd, and is widely

renowned as a reliable simulation tool even in critical atmospheric conditions. SPRAY code, whose structure will be discussed in Chapter 2, embeds an equation scheme for particle motion that is based on Eq. 1.12 and 1.13 for horizontal components of velocity fluctuations $u_x'$ and $u_y'$ in *Gaussian* and *non-homogeneous* turbulence conditions. For the vertical component $u_z'$ SPRAY adopts both a *Gaussian* and a *non-Gaussian* equation scheme to be used according to the atmospheric stability conditions. The *non-Gaussian* scheme can implement both the aforesaid *Bi-Gaussian* probability density functions and the *Gram-Charlier* series expansion. SPRAY model embeds also the equation scheme suggested by Hanna (1982), which is quite versatile for different atmospheric conditions, for the calculation of vertical profiles $T_{Lx}(x_z)$, $T_{Ly}(x_z)$, $T_{Lz}(x_z)$, $\sigma_{ux}(x_z)$, $\sigma_{uy}(x_z)$ and $\sigma_{uz}(x_z)$; for the whole set of equations see the code user manual (Arianet, 2007).

# Chapter 2

# *Lagrangian Particle Dispersion Models SPRAY and Micro-SPRAY*

## 2.1 General overview

### *2.1.1 The code SPRAY*

The simulations of pollutant plume dispersion from plant stacks at local scale (see next section 2.3) were performed via the Lagrangian Particle Dispersion Model SPRAY (Brusasca *et al.*, 1994; Tinarelli *et al.*, 2000). The model is able to simulate the airborne pollutant dispersion in critical conditions due to complex topography, low wind speed, non-stationary and non-homogeneous turbulence. In order to get started with a simulation, the following input data must be assigned to the model:

- ***Meteorological fields***, consisting of the three-dimensional *mean wind speed* and air *temperature fields*, are generally stored in binary-format input files. Both meteorological wind and temperature fields are generally provided by an external model for meteorological measurement data processing (see Chapter 3).

- ***Turbulence scale variables*** consist of the two-dimensional fields for the free atmosphere parameters, i.e. *Monin-Obukhov length L*, *Mixed Layer height* $H_{mix}$, *friction velocity u** and *convective scale velocity w**. Such parameters are stored in binary-format input files and computed at ground level according to the Similarity Theory schemes (see Chapter 3).

- ***Pollutant source***. Model user must primarily chose the proper geometry for each pollutant source to be considered in the simulation: point, line, volume, or area sources. Thus, according to source geometry, different spatial parameters are required. For plant stacks, which are generally modelled as point sources, the model requires: cartographic position

(UTM coordinates), stack-hole diameter (m) and height above ground level (m). Likewise, busy roads are modelled as segments, in which the starting and ending point of the segment and the pollutant mass flow per unit length must be assigned.

- ***Exhaust gas flow***. At first, model user must indicate all the chemical species involved in the exhaust gas emission; secondly, temperature (°C) and pollutant mass flow (kg/h) at the emission point of each source must be assigned for the whole set of chemical compounds. In case of ground deposition phenomena, for particulate emissions or radioactive decay, also particle diameter (μm) and density ($kg/m^3$), washout coefficient ($s^{-1}$), and half-life time (s) must be specified.

- ***Emission chronology***, i.e. the time series of pollutant mass flow with the corresponding number of emitted particles at each time frame. The chronology is generally articulated in equal hourly time frames, at which both pollutant mass flow and the related emitted particles $N_p$ are supposed to be constant.

- ***Simulation control parameters***, through which all the available calculation schemes and options must be defined by model user. In order to choose the correct simulation parameters model user can rely on the software user guide (Arianet, 2007).

- ***Domain (spatial scale) and simulation period (time scale)***: it is worthwhile to underline that the spatial domain in which meteorological fields have been computed must be larger than SPRAY simulation domain. Besides the whole SPRAY simulation period must be shorter than the time series of wind and temperature fields; more details about spatial and temporal structure of SPRAY code will be discussed in Paragraph 2.2 and 2.3.

Both time series of pollutant emissions and simulation parameters are stored in ASCII files.
SPRAY model is provided within the software package Aria Industry that also includes the diagnostic meteorological model MINERVE and the atmospheric turbulence model SURFPRO.
The whole model package Aria Industry is developed by Arianet Ltd (Milan, Italy) and Aria Technologies Plc (Paris, France). SPRAY code is also able to simulate several physical phenomena dealing with pollutant dispersion, for instance the gravitational dry and wet vertical settling of particulate emissions (Paragraph 1.1). SPRAY model, likewise, embeds an algorithm to simulate the exponential decay of radioactive species according to its half-life time.

The main hypothesis of Lagrangian particle dispersion models is the equal subdivision of the emitted pollutant flow in a certain number of virtual particles that are emitted at fixed user-defined time intervals. Pollutant concentration values, for each pollutant species, depend upon the number of particles that are contained in the surrounding of a given point (see Eq. 2.10). Since particles are supposed to transport a fixed amount of pollutant mass, no chemical reaction can be simulated for any pollutant specie, except for radioactive decay. As previously mentioned, also plume depletion for particulate ground deposition may be simulated.

SPRAY model is able to manage several anthropogenic pollutant sources, of different shape: mainly plant stacks and vehicular traffic, that can be modelled as point, area or line sources according to the geometry. Model performances were widely tested in the literature through the comparison with other both air quality models and experimental measurements (Gariazzo *et al*., 2004; Gariazzo *et al*., 2007; Ghermandi *et al*., 2012).

SPRAY code is written in FORTRAN language and was tested on many different platforms, under both Windows and UNIX environments.

SPRAY model is inserted in the European air quality models database "Model Documentation System", run by European Topic Centre on Air Pollution and Climate Change Mitigation (ETC/ACM, 2015).

### *2.1.2 The code Micro-SPRAY*

A new version of SPRAY code has been recently developed for airborne pollutant dispersion at urban micro-scale, i.e. by taking into account the turbulence effect due to building geometry in influencing the dispersion patterns. The Micro-SPRAY model, coupled with the micro-scale wind field processor Micro-SWIFT, has been applied for the micro-scale simulations of the present study that will be discussed later (see Chapter 5). The code embeds also an algorithm for simulating the dispersion patterns dealing with denser-than-air gases, which is suitable for fast-response studies about accidental releases of inflammable or explosive gases (Tinarelli *et al*., 2008; Anfossi *et al.*, 2010; Trini Castelli *et al.*, 2010).

## 2.2 Implemented equations for particle motion

According to an *Oxyz* Cartesian reference frame, the equations of motion for each particle are a finite differences discretization of Eq. 2.1 using an "upstream" time scheme.

$$\frac{dX(t)}{dt} = u(t) = \overline{u(t)} + u'(t) \tag{2.1}$$

The position vector $X(t) = [x_x(t),x_y(t),x_z(t)]$ of a given particle at time $t$ leads to the velocity vector $u(t)=[u_x(t),u_y(t),u_z(t)]$, which can be computed as the sum of a mean ($\bar{u}$) and a stochastic term ($u'$) (Paragraph 1.3). Eq. 2.1 can be written in the following way for each component of the position vector $X(t)$ and the velocity vector $u(t)$:

$$x_i(t+\Delta t) = x_i(t) + u_i(t)\Delta t \tag{2.2}$$

In Eq. 2.2 $i = x, y, z$ indicates the $x$, $y$ and $z$ axes; similarly, for the $u_i(t)$ speed component:

$$u_i(t) = \overline{u_i(t)} + u_i'(t) \tag{2.3}$$

By substituting Eq. 2.3 in Eq. 2.2, the Eq. 1.3 (Paragraph 1.3) is found.

The mean term $\bar{u}$ equals the mean velocity of the local wind at a certain node of the three-dimensional spatial grid that divides the computation domain in three-dimensional cells (see Paragraph 2.3). The mean value of each component of the wind speed $\bar{u}_i$ is externally computed by a meteorological model and provided to SPRAY code as input data. A meteorological model is an external processor that performs spatial interpolations of on-site meteorological measurements, in order to calculate the mean wind fields over the whole computational domain that are experienced along each particle trajectory.

The stochastic fluctuation term $u'$ is otherwise computed by SPRAY model itself as solution of a system of differential stochastic equations reproducing the statistical features of local atmospheric turbulence. The equation scheme, developed by Thompson (1987), takes into account the horizontal and vertical inhomogeneities of the turbulence and the asymmetries of the vertical velocity distribution in convective conditions. The general expression for the stochastic fluctuation term $u_i'$ is given by Eq. 2.4, which derives from Eq. 1.9:

$$u_i'(t+\Delta t) = a_i(X,u) + u_i''(t)\sigma_{ui}\sqrt{2\frac{\Delta t}{T_{Li}}} \qquad (2.4)$$

In Eq. 2.4 $\Delta t$ is the time step on which the model integrates the differential equations. Eq. 2.4 shows the dependence of the stochastic component $u_i'$ both on the statistics of turbulence field and on the random character of the turbulent flow itself. The statistical parameters consist of the *Lagrangian time scale* $T_{Li}$ and the velocity variances $\sigma_{ui}$ previously discussed at Paragraph 1.3; $u_i''(t)$ is the random (uncorrelated) velocity term, such that $u_i''(t_1)$ does not depend on $u_i''(t_2)$ when $t_1 \neq t_2$. The deterministic term $a_i(X, u)$ (or drift coefficient) depends both on the position $X(t) = [x_x(t),x_y(t),x_z(t)]$ and velocity $u(t)=[u_x(t),u_y(t),u_z(t)]$ vectors.

The mathematical expression for the $a_i(X, u)$ term depends on the chosen form for the probability density function $P(u_i, t)$. The simplest turbulence model involves a *Gaussian* form for PDF; in this case the drift coefficient has the expression as in Eq. 1.10.

SPRAY code adopts a Gaussian form for the PDF $P(u_x, t)$ and $P(u_y, t)$, dealing with the horizontal components of stochastic velocities $u_x$ and $u_y$, that leads to Eq. 1.12 and 1.13 (Paragraph 1.3).

However, as previously discussed in Paragraph 1.3, a Gaussian turbulence model is only suitable for the horizontal components of stochastic velocities; the vertical behaviour of turbulent eddies, when unstable atmospheric conditions occur, cannot be properly described by extending a Gaussian formulation even for $P(u_z, t)$. Hence, different options are adopted by SPRAY code in order to compute the drift coefficient $a_z(X, u)$, such as schemes based on a *Bi-Gaussian* PDF, or the *Gram-Charlier* series expansion for the drift coefficient $a_z(X, u)$; further details can be found in the SPRAY code user guide (Arianet, 2007).

The calculation of turbulence statistical parameters, i.e. vertical profiles of $T_{Lx}(x_z)$, $T_{Ly}(x_z)$, $T_{Lz}(x_z)$, $\sigma_{ux}(x_z)$, $\sigma_{uy}(x_z)$ and $\sigma_{uz}(x_z)$, SPRAY model adopts the Hanna (1982) scheme, which is suitable for several different atmospheric conditions; the detailed set of equations is reported in the code user manual (Arianet, 2007).

## 2.3 Spatial structure of SPRAY model

Equations for particle motion and source position in the computation domain refer to a Cartesian reference frame *Oxyz*, which is generally georeferenced in UTM projection and WGS 84 Datum. The following convention is generally adopted for axis orientation:

- *Ox*: West-East axis.
- *Oy*: South-North axis.

The computation domain consists of an arrangement of three-dimensional cells of volume $\Delta V = \Delta x_x \cdot \Delta x_y \cdot \Delta x_z$ ($m^3$) which depends on the chosen subdivision for *x*, *y* and *z* axes. Model user must assign the following parameters, aimed at defining the spatial features of simulation domain:

- ***Domain size***, i.e. the length $\boldsymbol{L_x}$ (m) and $\boldsymbol{L_y}$ (m) of calculation domain along the *x* and *y* axes. $\boldsymbol{L_z}$ (m) is the domain top; for local-scale simulations, a value about $10^3$ m is suggested.

- ***Horizontal grid resolution*** for concentration computing, i.e. the horizontal cell dimensions $\boldsymbol{\Delta x_x}$ (m) and $\boldsymbol{\Delta x_y}$ (m). From the chosen values for $\Delta x_x$ and $\Delta x_y$ derives the corresponding number of horizontal grid nodes $\boldsymbol{n_x}$ and $\boldsymbol{n_y}$ in which the computational domain lengths $L_x$ and $L_y$, along *x* and *y* Cartesian axes, are divided:

$$n_x = 1 + \frac{L_x}{\Delta x_x} \tag{2.5}$$

$$n_y = 1 + \frac{L_y}{\Delta x_y} \tag{2.6}$$

  According to Eqs. 2.5 and 2.6, $n_x$ and $n_y$ include the origin of the reference frame.

- ***Vertical grid resolution***, i.e. the point number $\boldsymbol{n_z}$ along *z* axis.

- ***Height above ground level*** $\boldsymbol{h_1}$ (m) of the first layer for concentration computing.

It is worthwhile to notice that, while $\Delta x_x$ and $\Delta x_y$ are kept constant along $x$ and $y$ axes, the distribution of vertical levels is not homogeneous, but follows a parabolic progression from ground level towards the domain top. According to this approach, the number of vertical layers is increased close to the ground surface, in order to attain a better approximation in simulating the dispersion phenomena in the Surface Layer, i.e. the part of the atmosphere near ground level where the wind field is more affected by surface roughness. The height above ground level of the first layer is user defined and 10 meters is the suggested value in case of *local-scale* simulations.

Topography has a great relevance on atmospheric circulation leading to slope flows and channelling effects. Such phenomena must be taken into account by air quality models in order to correctly simulate pollutant dispersion. With the aim of describing the land topography within the computational domain, ground elevation input data are required by SPRAY model; Digital Terrain Models (DTM), which give a 3D representation of a terrain surface, are the most commonly used source for ground altimetry data, i.e. altitude above sea level.

The first step is to assign a terrain elevation $x_{z,g}$ (altimetry) value to each node of the horizontal grid. The second step involves the interpolation of a continuous bilinear function $x_{z,g}(x;y)$ that represents the inferior boundary for particle dispersion. Let $P(x_{x,i},x_{y,j})$, $P(x_{x,i},x_{y,j+1})$, $P(x_{x,i+1},x_{y,j})$ and $P(x_{x,i+1},x_{y,j+1})$ be four distinct nodes delimiting the vertices of a square mesh, whose altitude elevation values are $x_{z,g}(x_{x,i},x_{y,j})$, $x_{z,g}(x_{x,i},x_{y,j+1})$, $x_{z,g}(x_{x,i+1},x_{y,j})$ and $x_{z,g}(x_{x,i+1},x_{y,j+1})$ respectively. A possible $x_z(x_x,x_y)$ function that well approximates points altimetry within the mesh is shown in Figure 3.

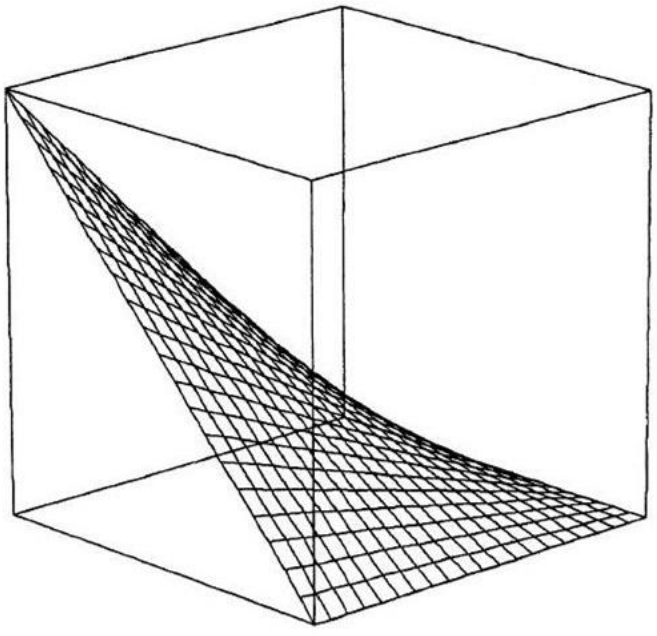

*Figure 3. Example of bilinear function* $x_z(x_x,x_y)$ *among four points.*

The general form of the bilinear function $x_z(x_x,x_y)$ is given in Eq. 2.7:

$$x_z = x_z(x_x,x_y) = ax_x + bx_y + cx_xx_y + d \tag{2.7}$$

and the $a$, $b$, $c$ and $d$ parameters are determined by imposing the passage for the points $P(x_{x,i},x_{y,j})$, $P(x_{x,i},x_{y,j+1})$, $P(x_{x,i+1},x_{y,j})$ and $P(x_{x,i+1},x_{y,j+1})$, of the topographic surface $x_z = x_z(x_x,x_y)$, since the respective elevation values $x_{z,g}(x_{x,i},x_{y,j})$, $x_{z,g}(x_{x,i},x_{y,j+1})$, $x_{z,g}(x_{x,i+1},x_{y,j})$ and $x_{z,g}(x_{x,i+1},x_{y,j+1})$ are known.

$$x_z(x_{x,i},x_{y,j}) = x_{z,g}(x_{x,i},x_{y,j}) \quad , \quad x_z(x_{x,i},x_{y,j+1}) = x_{z,g}(x_{x,i},x_{y,j+1}) \tag{2.8}$$

$$x_z(x_{x,i+1},x_{y,j}) = x_{z,g}(x_{x,i+1},x_{y,j}) \quad , \quad x_z(x_{x,i+1},x_{y,j+1}) = x_{z,g}(x_{x,i+1},x_{y,j+1})$$

The same operation is repeated for the four vertexes of each square horizontal cell of the computational domain, in order to cover the whole topographic surface of the study area.

Particles are allowed to move within the computational domain according to wind and turbulent forcing terms. For what concerns the lateral boundaries of domain, i.e. particles reaching the planes $x_x = 0$, $x_x = L_x$, $x_y = 0$, $x_y = L_y$, $x_z = L_z$ where $L_z$ is the domain top, the model assumes that such particles move across the boundaries and are definitely lost outside the calculation domain. On the contrary particles that reach the inferior boundary of the domain, i.e. the topographic surface, undergo an elastic collision and thus bounce back with a direction that depends on the inclination of the surface topography at a given point.

In order to take into account complex topography SPRAY code adopts a *terrain following* coordinate system in which the variable $x_z$ is modified in $x_z^*$ (m) as in Eq. 2.9:

$$x_z^* = L_z \frac{x_z - x_{z,g}}{L_z - x_{z,g}} \tag{2.9}$$

where:

- $L_z$ (m) is the height of the domain top;
- $x_{z,g}$ (m) is the altimetry of the given point on ground surface;
- $x_z$ (m) is the height of vertical levels along the $z$ axis.

Values for $x_z$ and $x_{z,g}$ are computed from a reference horizontal plane at the bottom of the simulation domain. The maximum value of $x_z$* is when the point lies at domain top $x_z = x_z* = L_z$ (m); the minimum value is for $x_z* = 0$ (m) when the point lies on the ground ($x_z = x_{z,g}$).

Figure 4 (left) shows a possible $x_x,x_z$ plane section in a $x_x,x_y,x_z$ spatial domain that takes into account complex topography. Vertical lines represent $x_x$=*constant* coordinates, whereas the crossing irregular ones would represent $x_z* = constant$ lines that appear to be regular in the $x_x,x_y,x_z*$ "terrain following" coordinate system (Figure 4, right).

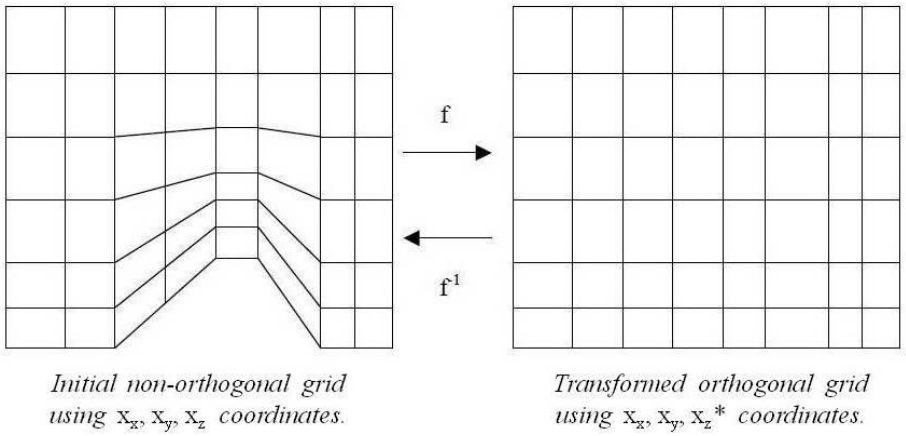


*Figure 4. Plane section $x_x,x_z$ in a $x_x,x_y,x_z$ spatial domain (left) and in a $x_x,x_y,x_z*$ "terrain following" coordinate system (right) respectively.*

The so-obtained three-dimensional "terrain-following" grid is the reference for concentration computing, i.e. $C=C(x_x,x_y,x_z*)$ concentration values are assigned to each node of the $x_x,x_y,x_z*$ three-dimensional grid. By consequence, the computed concentration field consists of an $n_x \cdot n_y \cdot n_z$ array of concentration values, according to the spatial resolution of computational domain.

The concentration value at each node of the grid refers to the South-West vertex of the horizontal cell, which is also the low left point of the cell itself, as shown in Figure 5.

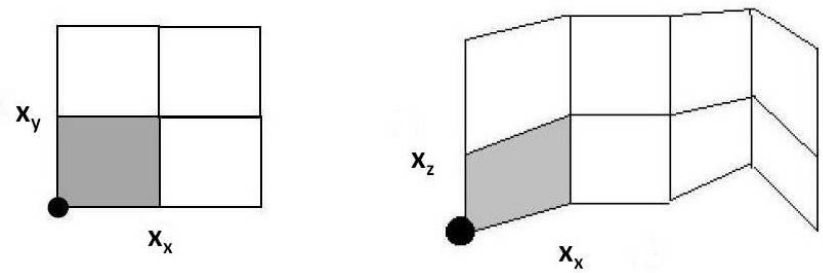


*Figure 5. Plane sections $x_x,x_y$ and $x_x,x_z$ of a domain cell for concentration computing; the concentration value refers to the black dot.*

In order to achieve a high resolution in output concentration fields the user should use a spatial grid with a large amount of nodes, but the main constrain is the required computational time. For the local-scale simulations of the present study, according to the suggestions of model developers, the following values were chosen with the aim of finding a compromise between a good representation of concentration fields and the computational time of the simulation:

$L_x = L_y = 20$ km;
$n_x = n_y = 81$ (the Cartesian origin is included);
$\Delta x_x = \Delta x_y = 250$ m;
$L_z = 1800$ m above ground level;
$n_z = 30$.
$h_1 = 10$ m.

Computational time depends also on other three parameters: numbers of emitted particles in a time lapse, number of pollutant sources and the integration time step for the differential equations of particle motion that will be discussed later.
However, since the aim of the present study is to perform local-scale simulation for the 2010 winter season (see Chapter 5), the expected computational time is about of three-four hours.

## 2.4 Temporal structure of SPRAY model

The following time frames must be defined before starting a new simulation:

• ***Emission time frame $\Delta t_{em}$*** (s) defines a time interval during which a certain number of particles, all containing a fixed mass of each pollutant species, are supposed to be emitted. The $\Delta t_{em}$ is the same for all the considered pollutant sources and it is kept constant for the whole simulation period; conversely, the number of the emitted particles within each $\Delta t_{em}$ is generally variable during the simulation according to the time variability of the emitted pollutant mass flow from each source.

• ***Synchronization time frame $\Delta t_{sync}$*** (s). Since the physical properties of turbulent fields are not homogeneous in space and time, the time step $\Delta t$ on which SPRAY model integrates the differential equations for particle motion (Eqs. 2.2 and 2.4) is not defined a priori, but it is periodically changed according to the evolution of turbulence fields that each particle experiences along its trajectory. Thus the time history of each particle deals with a proper time reference.
Therefore, SPRAY model requires the user to define the $\Delta t_{sync}$ time lapse, i.e. the synchronization frequency $1/\Delta t_{sync}$ at which all the equations for particle motion are re-synchronized at the same univocal time reference. Moreover SPRAY model manages the aforesaid variable time step $\Delta t$ adopting $\Delta t_{sync}$ as a superior boundary ($\Delta t < \Delta t_{sync}$).

• ***Sampling time frame $\Delta t_{samp}$*** (s) defines the time frequency ($1/\Delta t_{samp}$) at which all the information about particle positions is gathered and the concentration value $C_{i,j,k}$, at a given *k-cell*, for the *i-pollutant specie*, emitted from the *j-source*, is computed according to the following formula:

$$C_{i,j,k} = \frac{N_{j,k}}{N_{p,j}} \frac{\dot{m}_{i,j}\,\Delta t_{em}}{\Delta V_k} \tag{2.10}$$

In Eq. 2.10 $N_{j,k}$ is the number of counted particles within the k-cell at a given sampling time, $N_{p,j}$ is the number of the emitted particle within the $\Delta t_{em}$ (s) time frame by the j-source, $\dot{m}_{i,j}$ (kg/s) is the pollutant mass flow from the j-source and for the i-pollutant specie and $\Delta V_k$ ($m^3$) is the volume of the k-cell. Such formula is applied at each node of the grid (Paragraph 2.3) in order to build up the $n_x \cdot n_y \cdot n_z$ array of concentration values. The so-computed concentration fields, which are produced with a time frequency equal to $1/\Delta t_{samp}$, are averaged over a fixed period (generally one hour) and

stored in the output concentration file. As shown in Paragraph 1.2, model concentration outputs are expressed as mass per unit of volume; thus, the measurement unit is allowed to be ($kg/m^3$), or ($mg/m^3$), or ($\mu g/m^3$), according to the model outputs magnitude.

In order to achieve a great approximation of the dispersion phenomena, as previously seen for the spatial structure of the model, even a good time resolution is required; this implies that particle positions within the computational domain should be sampled frequently. Moreover, a large amount of particles $N_{p,j}$ should be emitted within the $\Delta t_{em}$ in order to better appreciate the shortest differences among concentration values between two cells.

Following model developers suggestion, a $\Delta t_{em}$ = 30 s and a $\Delta t_{sync} = \Delta t_{samp}$ = 60 s were chosen.

In SPRAY model particles are generated at fixed user defined times intervals ($\Delta t_{em}$); at the beginning of the simulation no particle are contained within the simulation domain. Therefore, in order to avoid possible underestimation of pollutant concentration values due to the lack of particles in the first part of the simulation, the first particle sampling can be delayed from the beginning of the simulation. Moreover SPRAY model embeds a flag parameter that allows at starting a new simulation at the end of a previous simulation, by reading the last particle positions stored. Hence, despite of the interruption, the new simulation restarts as the continuation of the last one.

## 2.5 Modelling plume rise effect

The routine of plume rise controls pollutant plume elevation due to the buoyancy force that occurs when exhaust gas are warmer than atmospheric air. The vertical position of a generic i-particle at time $t + \Delta t$ is given by the following formula that modifies Eq. 2.2 for the $x_z$ coordinate:

$$x_z(t+\Delta t) = x_z(t) + [u_z(t) + u_z^p(t)]\Delta t \tag{2.11}$$

The $\Delta t$ in the Eq. 2.11 is the same adopted for the integration for particle motion equations (Eqs. 2.2 and 2.4); the time $t$ is the "life-time" of a particle, i.e. the elapsed time since a particle was emitted.
In the Eq. 2.11 there are two contributions to the upward thrust of a particle; the former contribution is the particle velocity along the $z$ axis $u_z(t) = \overline{u_z(t)} + u_z'(t)$, that depends both upon the vertical ascent of air flow due to the interferences with complex topography ($\overline{u_z(t)}$, see also Paragraph 3.2.4) and upon the convective turbulence in unstable conditions ($u_z'(t)$, see also Paragraph 1.3); the latter, $u_z^p(t)$, is the particle rise depending on its buoyancy.
Following an approach suggested by Anfossi *et al.* (1993), whom revised the Briggs formula (Briggs, 1984) for buoyant plume rise, the particle ascent $\Delta x_z^p$ is computed according to Eq. 2.12, where $t$ is the particle life-time and $\bar{u}_h$ (m/s) is the *average horizontal wind speed* at the stack exit.

$$\Delta x_z{}^p(t) = 2.6 \cdot \left( \frac{F_b t}{\bar{u}_h} \right)^{1/3} \cdot (t^2 s + 4.3)^{-1/3} \quad \text{(m)} \tag{2.12}$$

In Eq. 2.12, the buoyancy parameter $F_b$ was introduced with the following expression, which can be found by applying the mass and thermal energy balance equations on an infinitesimal air volume of exhaust gas at stack exit (Sozzi, 2003):

$$F_b = g w_0 r^2 \frac{T_f - T_a}{T_a} \quad (\text{m}^4/\text{s}^3) \tag{2.13}$$

The symbols appearing in the Eq. (2.13) are the following:

- ***r*** is the ***stack radius*** (m).
- ***$w_0$*** is the ***smoke exit speed*** from the stack (m/s).

• ***g*** is the ***gravity acceleration*** (m/s$^2$).

• $\boldsymbol{T_f}$ is the ***smoke exit temperature*** from the stack (°C).

• $\boldsymbol{T_a}$ is the ***atmospheric air temperature*** near the stack exit (°C).

In addition, the ***stability parameter s*** is also introduced according to the following expression:

$$s = \frac{g}{\vartheta}\frac{\partial \vartheta}{\partial x_z} \quad (s^{-2}) \tag{2.14}$$

The ***potential temperature $\theta$*** is the temperature that would be attained by an air parcel, which is initially at *pressure P*, if adiabatically brought to the *standard pressure value $P_0$ = 1 000 hPa*.
The importance of the potential temperature is that $\theta$ enables to estimate atmospheric stability conditions at a reference pressure $P_0$ for all the air particles, even if the actual value of atmospheric pressure is variable due to the lifting or sinking motion of the particle, the topographic obstacles, or the large-scale atmospheric turbulence. The stability parameter *s* provides an estimation of the atmospheric stability conditions according to this range of values:

- $s < 0$ (s$^{-2}$): unstable conditions;
- $s > 0$ (s$^{-2}$): stable condition;
- $s = 0$ (s$^{-2}$): neutral conditions.

The final expression for $u_z^p(t)$ to be substituted in Eq. 2.11 is given by Eq. 2.15:

$$u_z^p(t) = \frac{[\Delta x_z{}^p(s, \bar{u}_h, t + \Delta t) - \Delta x_z{}^p(s, \bar{u}_h, t)]}{\Delta t} \tag{2.15}$$

By means of *s* parameter, SPRAY model controls the duration of each particle ascent involved in the plume rise effect by taking into account the <u>*entrainment phenomenon*</u>, i.e. the mixing of pollutant plume with cooler atmospheric air that lead particles to lose its buoyancy and the plume rise phenomenon to fade out. In order to take into account the inhibition of plume rise due to the entrainment phenomenon, SPRAY model starts to neglect the plume rise algorithm after a specific value for time *t* of particle life-time, according to the following rule:

$$t > \min\left(\frac{10H_s}{u_s}; t_s\right) \tag{2.16}$$

where $H_s$ is the stack height, $u_s$ is the horizontal wind speed at stack height position and $t_s$ (s) assumes the following value according to atmospheric stability:

$$t_s = \frac{2}{\sqrt{s}}, \quad \text{when s < 0;} \tag{2.17}$$

$$t_s = \frac{49F_b^{5/8}}{u_s}, \quad \text{when s = 0 and } F_b < 55 \text{ m}^4/\text{s}^3;$$

$$t_s = \frac{119F_b^{2/5}}{u_s}, \quad \text{when s = 0 and } F_b > 55 \text{ m}^4/\text{s}^3;$$

$$t_s = 1.72u_s^{3/5}F_b^{2/5}H_{mix}^{3/5}w_*^{9/5}, \quad \text{when s > 0.}$$

In the last formula also *Mixed Layer height* $H_{mix}$ and *convective scale velocity* $w^*$ that will be discussed in Chapter 3 are considered.

In Eulerian Gaussian models plume rise is managed with a simple vertical translation of the plume horizontal axis along *z* axis according to the well-known Briggs formula (Briggs, 1984). On the contrary, the Anfossi approach for Lagrangian particle models focus the attention on each single particle and enable to investigate the plume rise phenomena more in detail since the whole atmospheric properties experienced by each particle trajectory are taken into account.

## 2.6 Modelling pollutant emission sources

In order to simulate particles emission from pollutant sources, SPRAY model requires several input data, already listed in the previous Paragraph 2.1: Pollutant source, Exhaust gas flow, Emission chronology.

All the aforesaid input data are sorted in ASCII input files for SPRAY model. Such files can be generated via the *Emission Manager* tool (Arianet, 2008), which is included in the Aria Industry software package. Emission Manager sorts the required data, for each pollutant source and each chemical compound, and builds the emission chronology according to the user-defined starting and ending date; the emission chronology must cover the whole simulation period.

In case of variable pollutant mass flow along the simulation period, a temporal modulation of the emission pattern can be achieved with a different temporal resolution, e.g. monthly, weekly, daily or hourly depending on the duration of the simulation period. The modulation pattern consists of a time series of coefficients that are used to amplify or reduce the emitted pollutant mass, according to the fluctuations experienced by pollutant flow rate at a specific source.

According to the source geometry and the user-defined pollutant mass flow, the model defines how many particles must be emitted in the $\Delta t_{em}$ time frame (Paragraph 2.4).

$N_{p,j}$, which is the number of the emitted particle within the $\Delta t_{em}$ (s) time frame by the j-source (Eq. 2.10, Paragraph 2.4), highly influences the spatial resolution of the concentration fields (Paragraph 2.3). $N_{p,j}$ is automatically computed by the code, for each considered emission j-source, according to the following formula.

$$N_{p,j}(\Delta t_{em}) = \frac{\dot{m}_{s,j}\,\Delta t_{em}}{\Delta V \cdot f_{samp} \cdot RES} \tag{2.18}$$

where the following parameters must be assigned by model user:

- $\boldsymbol{\Delta V = \Delta x_x \cdot \Delta x_y \cdot h_1}$ ($m^3$) is the volume of the computational cell close to the ground level. $\Delta x_x$ and $\Delta x_y$ are the horizontal dimensions of the computation cell and $h_1$ is the height above ground level of the first layer for concentration computing. $\Delta x_x$, $\Delta x_y$ and $h_1$ terms must be consistent with the previously defined values for the computational grid resolution (Paragraph 2.3).

- ***RES*** (μg/m$^3$) is the minimal concentration resolution required, i.e. the concentration value that the model appreciates when only one particle is found within a computational cell.

- $f_{samp}$ is ratio among the frequency of particle samplings and the frequency of concentration computing repetitions. Such non-dimensional parameter, which depends upon the value of $\Delta t_{samp}$, is an index of the quality for temporal resolution in concentration computing.

- $\dot{m}_s$ (μg/s) is the emitted mass flow of the pollutant specie for which the maximum concentration value in the exhaust gas is observed.

It is worthwhile to notice that, the larger is $N_{p,j}$ the higher is the spatial resolution achieved for concentration computing, since the pollutant mass flow is subdivided in a greater amount of particles that can represent more in detail the shortest differences among concentration values between two adjacent cells. The choice of spatial parameters $\Delta x_x$, $\Delta x_y$ and $h_1$, as well as *RES*, $\Delta t_{em}$ and $f_{samp}$ depends upon the pollutant concentration values that are expected from model outputs.
By shifting from local-scale to micro-scale simulations the $\Delta V = \Delta x_x \cdot \Delta x_y \cdot h_1$ value is reduced by several orders of magnitude, as well as the size of the computational domain and the frequency of time repetitions for concentration computing. Moreover, at urban micro-scale, higher concentration values are expected due to the vicinity to pollutant sources; hence, the resolution of concentration value is increased. Therefore, for micro-scale simulations, according to Eq. 2.18, an increase of the number of the emitted particles $N_{p,j}$ is noticeable. On the other hand, due to the reduction of domain dimensions, the model loses a greater amount of particles through the domain boundaries. Hence the code must handle more particles than in case of a local-scale simulation, in order to counterbalance the losses.
Table 1 summarizes, both for local-scale and micro-scale simulations, the suggested options for the parameters in Eq. 2.18 according to model developers (Arianet Ltd).

| **Variable name** | **LOCAL-scale** | **MICRO-scale** |
|---|---|---|
| **$\Delta V$ (m$^3$)** | $10^5$-$10^6$ | $10^0$-$10^1$ |
| **$f_{samp}$** | $10^1$ | $10^2$ |
| **$\Delta t_{em}$ (s)** | $10^1$ | $10^0$ |
| **RES (μg/m$^3$)** | $10^{-2}$-$10^{-1}$ | $10^{-1}$-$10^0$ |
| **$N_p$** | $10^0$-$10^1$ | $10^1$-$10^2$ |

*Table 1. Summary of the suggested values for the parameters in Eq. 2.18.*

# Chapter 3

# *MINERVE and SURFPRO models*

## 3.1 Introduction

According to Eq. 2.3 (Paragraph 2.2), SPRAY model computes particle velocity as the sum of two terms: the mean velocity of the local wind and the stochastic fluctuation due to atmospheric turbulence that each particle experiences during the motion. The mean wind speed values are embedded in the three-dimensional wind fields, which are provided by an external meteorological processor that interpolates wind speed measurements by taking into account complex topography. The stochastic fluctuation terms, which are directly computed by SPRAY code (Eq. 2.4), depend on the statistical properties of turbulence field, i.e. the vertical profiles of $T_{Lx}(x_z)$, $T_{Lv}(x_z)$, $T_{Lz}(x_z)$, $\sigma_{ux}(x_z)$, $\sigma_{uy}(x_z)$ and $\sigma_{uz}(x_z)$ parameters. Variances, Lagrangian time scales and higher order statistical moments are computed, in turn, by means of the Hanna scheme (1982), that requires the two-dimensional fields of atmospheric turbulence scale variables: Monin-Obukhov length $L$, Mixed Layer height $H_{mix}$, friction velocity $u^*$ and convective scale velocity $w^*$.

As well as the meteorological fields, also turbulence scale variables must be externally computed by means of a turbulence processor for the free atmosphere.

The software package Aria Industry, by Arianet Ltd (Milan, Italy) and Aria Technologies Plc (Paris, France), in addition to SPRAY code, includes the diagnostic meteorological model MINERVE and the turbulence model SURFPRO. Hence the preparation of meteorological and turbulence input data for SPRAY simulations can be easily achieved by using MINERVE and SURFPRO models. The following section provides a brief description of such simulation tools and introduces the Similarity Theory for the aforesaid turbulence scale variables formulation.

## 3.2 Meteorological model MINERVE

### *3.2.1 Overview of the code*

MINERVE (Geai, 1987; Desiato *et al.*, 1998; Finardi *et al.*, 1998; Cox *et al.*, 1998; Cox *et al.*, 2005) is a mass - consistent diagnostic model that is designed to generate meteorological fields.
The calculations are performed on a three-dimensional grid, by interpolating on-site meteorological observations, in order to compute the three scalar components $\bar{u}_x$, $\bar{u}_y$ and $\bar{u}_z$, and the scalar values for temperature and relative humidity. Such values are computed at each node of the grid according to the chosen interpolation method.
All the interpolation methods supported by MINERVE model take into account the influence of complex topography and soil roughness on wind speed and temperature values. Interpolations can be performed both at mesoscale (50 -100 km) and at local-scale (5-50 km).
The outcome fields are stored in a binary format file that can be directly provided to SPRAY model. Figure 6 shows the flow chart of MINERVE input and output data (Aria Technologies, 2001).

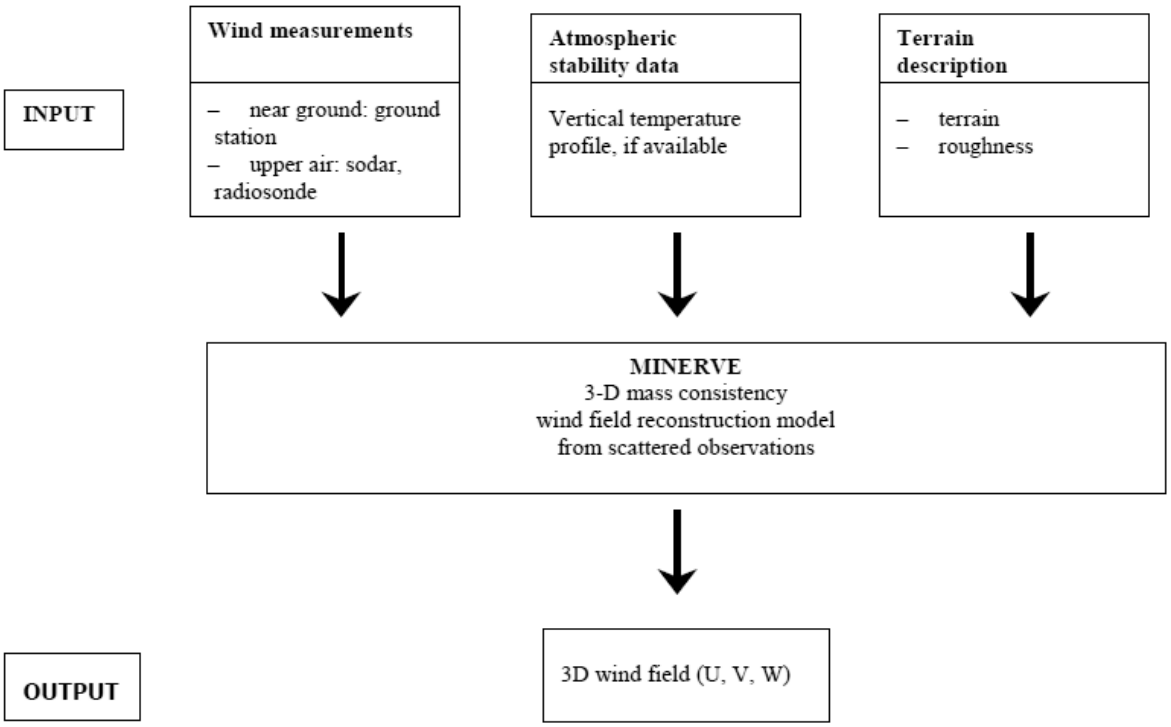


*Figure 6. MINERVE model flow chart for input and output data.*

Figure 7 shows the graphical interface of the code, thanks to which the user can manage the path for input data files and calculation options.

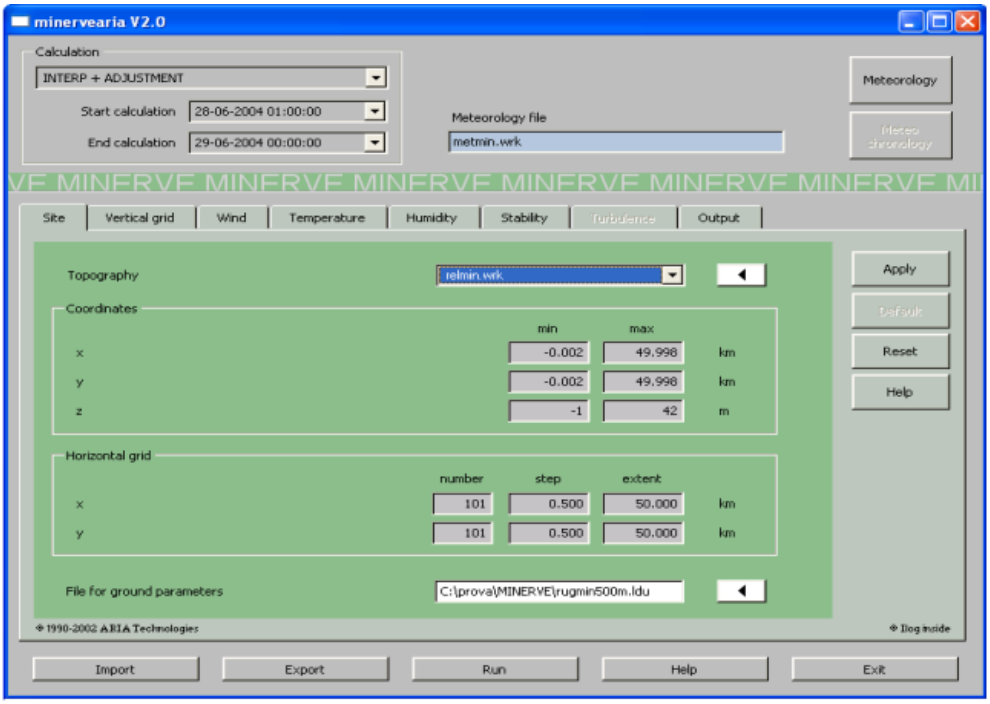


*Figure 7. Graphical user interface of MINERVE code.*

### *3.2.2 MINERVE input data*

MINERVE code requires the following input data that are generally provided through ASCII files:

- **Meteorological data** consist in time series of wind speed, wind direction, air temperature and relative humidity from on-site measurements, which must be provided to MINERVE model. The dataset must cover the whole simulation period.

  All the assigned input data must be georeferenced; thus, the geographical position of measurement points, i.e. the cartographic UTM coordinates, must be specified for the whole network of measurement stations. In addition, the height above ground level at which a measure is collected, which will be discussed in Paragraph 3.2.3, is a key parameter to be specified.

- **Surface roughness**: the roughness length $z_0$ is an important parameter for the calculation of turbulence variables close to the terrain surface; it depends on land-use and land-cover.

- **Topography**. Similarly to SPRAY code, also MINERVE model operates on a three-dimensional grid and on a Cartesian reference frame *Oxyz*. Cartographic coordinates of grid nodes are usually assigned in UTM projection and WGS 84 Datum; *Ox* is the West-East axis and *Oy* is South-North axis. Besides, model user must assign the altimetry (in meters) above sea level of each node of the horizontal grid, in order to define the topographic surface.
  All the spatial interpolations are performed from the ground surface towards the domain top. The vertical grid consists of a $x_x,x_y,x_z$* *"terrain-following"* coordinates system, whose properties are the same described in Paragraph 2.3 for SPRAY model.

All the required data for surface roughness and terrain elevation (topography) can be outlined from remote sensing images. In the present study raster images from European CORINE Land Cover 2000 dataset (EEA, 2015a), with a spatial resolution of 100 x 100 m, were adopted for land-use surface data. Ground elevation data were provided by Shuttle Radar Topography Mission through United States Geological Service (USGS), sampled at 3 arc-seconds.

The input meteorology is assigned to MINERVE code as local *near-ground* data or *upper-air* data. Local near-ground data generally consist of on-site measurements from meteorological stations. Upper-air data consist of vertical profile of wind speed, wind direction, temperature and relative humidity; vertical profiles provide a description of vertical atmospheric stratification, which has to be taken into account in the interpolation operations. Model developers suggest using measured data also for vertical profiles, i.e. from radio-sounding measurements. In case of unavailability of radio-sounding measurements, vertical profiles can be obtained by means of vertical interpolations of atmospheric variables, which have to be performed via an external processor. However, for a reliable three-dimensional interpolation of meteorological fields, MINERVE code requires data from at least one ground measuring site and, at least, one vertical profile for temperature.

In the present study, meteorological fields were simulated by using both simulated and measured meteorological data. Meteorological on-site measurements were collected at the ground stations of the Osservatorio Geofisico of the University of Modena and Reggio Emilia (Modena, Italy) and of the Local Environmental Agency (ARPA). Mesoscale vertical profiles were simulated and provided by ARPA by means of CALMET model (Deserti *et al.*, 2001). CALMET (Scire *et al*., 2000) is a meteorological mesoscale model that can be coupled with larger-scale air quality models (Yim *et al.,* 2007; Cox *et al*. 2005; Chandrasekar *et al*. 2003; Jackson *et al*. 2006). The CALMET simulations for the present study were accomplished by using a meteorological dataset, consisting of ground measurements and radio sounding profiles of temperature and wind speed from the whole area of Northern Italy.

### *3.2.3 MINERVE interpolation methods*

For wind speed and temperature interpolation two different approaches can be followed:

- ***Two-dimensional*** *interpolation*; is the simplest and most approximate method, but also the faster from a computational point of view. Once the vertical grid structure is defined, the horizontal components of wind velocity $\bar{u}_x$ and $\bar{u}_y$ are gradually interpolated on each level $x_z$*=*constant*, by starting at ground level towards the domain top. Therefore, the model firstly uses ground measured data; secondly, vertical interpolations in altitude are performed by using vertical wind profiles.

- ***Three-dimensional*** *interpolation* is directly performed by taking into account all three spatial directions; hence both ground data and vertical profiles are simultaneously used.

Three-dimensional interpolation is suitable only if a large amount of vertical profiles is available.
In the present study, since only one vertical profile is accessible, the two-dimensional Mac Lain interpolation method was applied.
Mac Lain procedure (1976) is based on a triangulation of the horizontal domain in which vertexes correspond to the ground measuring stations where on-site measurements were collected.
The interpolation is performed at each level $x_z$*=*constant*; $\bar{u}_x$ and $\bar{u}_y$ horizontal components are firstly computed at each triangle vertex, and secondly at each grid node by means of Eq. 3.1:

$$U_i(x_x, x_y) = \frac{\sum_{k=1}^{k=3} \Phi_k(x_{x,k}, x_{y,k}) d_k}{\sum_{k=1}^{k=3} d_k} \tag{3.1}$$

In Eq. 3.1 $d_k$ (m) is the distance of the grid node from the k-vertex of the triangle; the parameter $\Phi_{k,i}(x_{x,k};x_{y,k}) = U_{k,i}(x_{x,k};x_{y,k})$ (m/s) is the horizontal wind speed component at the aforesaid *k*-vertex along the *x* and *y* Cartesian axes (*i* = *x*, *y*). $\Phi_{k,i}(x_{x,k};x_{y,k})$ can be a measured value, if the vertex corresponds to a measuring station, or a previously computed value if no meteorological station takes place at the k-vertex. $\vec{U}(x_x, x_y) = (U_x, U_y, U_z)$ is the interpolated wind speed vector at a given point $P(x_x,x_y)$ of the computational grid. The vertical component $U_z(x_x;x_y)$is equal to 0 (m/s)because

all the input measurements are supposed to be collected with anemometers that operate on the horizontal plane; hence only $U_x(x_x;x_y)$ and $U_y(x_x;x_y)$ components are involved in the calculation.

Meteorological observations refer to a specific height above ground level depending on the site of the measurement instrument; hence, prior to interpolate calculated and observed values, these are referred to the same vertical layer. Vertical corrections, at a given *k*-meteorological station of Cartesian coordinates $(x_{x,k};x_{y,k})$, of measured horizontal wind speed values are based on the following formula:

$$u_k(x_z) = \frac{u^*}{C_k} \log\left(\frac{x_z}{z_0}\right) \tag{3.2}$$

where $u_k=u_k(x_z)$ (m/s) is the corrected value for horizontal wind speed, $u^*$ (m/s) is the friction velocity and $C_k=0.4$ is the von-Karman constant. Let $h_1$ be the altitude above ground level of the first vertical layer in correspondence of the meteorological given station; let $h_m$ be the height above ground level at which the measurements were collected. Thus, the correct value of wind speed $u_k=u_k(h_m)$ to be used in the interpolation procedure is given by the following formula:

$$u_k(h_m) = u_k(h_1) \frac{\log\left(\frac{h_m}{z_0}\right)}{\log\left(\frac{h_1}{z_0}\right)} \tag{3.3}$$

It is worthwhile to notice that, before applying the chosen interpolation procedure, the $u_k=u_k(h_m)$ value is divided in the two horizontal components $U_{k,x}(x_{x,k};x_{y,k})$ and $U_{k,y}(x_{x,k};x_{y,k})$ by applying the trigonometric functions of the measured wind direction angle.

The numerical interpolation over the first layer above ground level is performed using ground measured data only. On the contrary the interpolation at the higher layers depends on wind speed values from vertical profiles. These latter values are assigned at specific heights along the vertical profile and must be referred to each $x_z^*=constant$ layer by applying again Eq. 3.2 and 3.3.

This methodology here described for wind speed components interpolation, it is similarly applied for air temperature data.

### *3.2.4 Wind field adjustment procedure*

Since the atmosphere is assumed as a non-compressible fluid, the interpolated wind field $\vec{U}(x_x, x_y) = (U_x, U_y, U_z)$ must satisfy the Eq. 3.4 for mass conservation over the whole domain:

$$div\vec{U} = 0 \tag{3.4}$$

Nevertheless the interpolated wind field has been estimated geometrically using only vector components without taking into account air density.

Hence, in order to perform pollutant dispersion simulation with a more reliable input wind field, some corrections are required. The problem is approached by MINERVE model by imposing both the satisfaction of the mass conservation and, on the other hand, the minimization of the differences between the "geometrically" interpolated wind field and the mass-consistent "adjusted" wind field. According to this methodology the outcomes maintains a certain consistency with both wind measurements and mass conservation (Eq. 3.4). Let $\Omega$ be the set of points inside the computational domain and $\Gamma$ the set of border points; by applying the Lagrange multipliers method, the air incompressibility constraint is introduced by means Eq. 3.5 (Ratto *et al*., 1994; Homicz, 2002):

$$J(\vec{U},\lambda) = \int_{\Omega} (\overline{u_x} - U_x)^2 + (\overline{u_y} - U_y)^2 + (\overline{u_z} - U_z)^2 + \frac{(\overline{u_z} - U_z)^2}{\chi} d\Omega + \int_{\Omega} \lambda(\frac{\partial \overline{u_x}}{\partial x} + \frac{\partial \overline{u_y}}{\partial y} + \frac{\partial \overline{u_z}}{\partial z}) d\Omega + \beta \int_{\Gamma} (\vec{n}(\vec{u} - \vec{U}))^2 d\Gamma \tag{3.5}$$

The functional $J(\vec{U},\lambda)$ is the sum of three integrals: the first integral quantifies the deviation between the final adjusted wind field, with components $\overline{u}_x$, $\overline{u}_y$, $\overline{u}_z$, and the interpolated wind field, with components $U_x$, $U_y$ and $U_z$. The second is the integral of wind field divergence: according to the *Gauss - Green Theorem* (or divergence theorem) it should be equal, unless the sign, to the third integral, which represents the wind field, flow through the border of the domain. Parameters $\lambda$ and $\beta$ are called *Lagrangian multipliers*. In Eq. 3.5 appear the $U_x = U_x(x,y)$ and $U_y = U_y(x,y)$horizontal components of the interpolated wind field $\vec{U}$, which were previously computed by means of Eq. 3.1; it is worthwhile to remind that the vertical component $U_z = U_z(x,y) = 0$.

The final adjusted wind field $\overline{u}$ is characterized by $\overline{u}_x$, $\overline{u}_y$ and $\overline{u}_z$ components; as previously discussed in Paragraph 2.2, the $\overline{u}_x$, $\overline{u}_y$ and $\overline{u}_z$ components are equal to the mean velocity of the local wind to be used by SPRAY model (Eq. 2.3, Paragraph 2.2) to compute particle trajectories.

The non-dimensional parameter $\chi$ is a weighting function for the vertical component of wind velocity $\bar{u}_z$ with respect to the two horizontal $\bar{u}_x$ and $\bar{u}_y$; since $U_z$ cannot be computed with measured data ($U_z = 0$; see also Paragraph 3.2.3), $\bar{u}_z$ component is calculated during the adjustment process within the domain areas where the air flow rises up due to the simulation domain topography. The velocity $\bar{u}_z$ varies according to thermal stability of the atmosphere that enhances or inhibits the vertical turbulent transport, and that is mainly related to the temperature field. The dependence of $\bar{u}_z$ on the atmospheric stability can be expressed by means of the *χ-weighting* factor; moreover, $\chi$ can be related, as shown by Moussiopoulos *et al*. (1988), to the *stability parameter s* (Eq. 2.14, Paragraph 2.5). Two main boundary conditions may occur:

• ***χ→0*** in ***stable conditions (s > 0)***, when the thermal convection is almost totally inhibited. In this case, wind flow tends to bypass the obstacles by turning around. Hence the $\bar{u}_z$ component has a negligible weight, if compared to horizontal components $\bar{u}_x$ and $\bar{u}_y$.

• ***χ→1*** in ***unstable conditions (s < 0)***. In this case wind tends to bypass obstacles "from above" and the $\bar{u}_z$ component has a very significant weight if compared to horizontal components $\bar{u}_x$ and $\bar{u}_y$.

For the calculation of $\chi$ MINERVE is able to implement different schemes (Louis, 1979; Moussiopoulos *et al*., 1988). The adjusted wind field must satisfy the following conditions:

$$\frac{\partial J}{\partial \bar{u}_x} = \frac{\partial J}{\partial \bar{u}_y} = \frac{\partial J}{\partial \bar{u}_z} = \frac{\partial J}{\partial \lambda} = 0 \qquad (3.6)$$

that leads to a matrix system which can be solved according to the *Gauss – Siedel method*; further details are given in the code user guide (Aria Technlogies, 2001).

## 3.3 Turbulence processor SURFPRO

### *3.3.1 The Similarity Theory for Planetary Boundary Layer*

Pollutant dispersion phenomena in the atmospheric environment are generally bounded within the atmospheric layer close to the ground surface, well-known as Planetary Boundary Layer (PBL). According to Stull (1989) the PBL thickness extends up to the ground surface to a height of 100-3000 m. The daily evolution of PBL strictly depends on turbulence phenomena occurring close to the ground surface, as a consequence of *"the forcing effects dealing with frictional drag, solar heating, and evapotranspiration"* (Stull, 1989). With the aim of describing such complex phenomena and their influence on pollutant dispersion patterns, some physical variables have been developed, according to the *Similarity Theory* for PBL by Monin and Obukhov. The Similarity Theory is based on the following parameters that give an approximated estimation of turbulence in the PBL, according to the aforesaid forcing effects:

- **Friction velocity *u**** (m/s): it estimates the mechanical turbulence effect due to the friction drag by ground surface to wind motion. According to the horizontal fluctuations of wind speed $u_x'$ and $u_y'$, the $u^*$ value can be estimated with the following formula:

$$u^* = \left(\overline{u_x' u_y'}\right)^{0.5} \tag{3.7}$$

  Alternatively, since an estimation of $u_x'$ and $u_y'$ can be quite difficult, the following relation estimates the $u^*$ value as a function of the vertical gradient of wind speed $\bar{u}$:

$$u^* = C_k x_z \frac{\partial \bar{u}}{\partial x_z} \tag{3.8}$$

  where $C_k=0.4$ is the empirical Von-Karman constant. The $u^*$ value increases when mechanical turbulence is enhanced; $u^*$ varies in the range between 0.05 and 0.3 m/s.

- **Convective scale velocity *w**** (m/s): estimates the vertical speed for the ascent of air particles due to the buoyancy forcing. Convective turbulence depends on the sensible heat flux exchanged at the soil-atmosphere interface $H_0$ (W/m$^2$), which is strictly related to the

solar heating at ground surface (Eq. 3.14). The following formula, in which also the absolute *air temperature* $T$ (K), the *gravitational acceleration* $g=9.81$(m/s), the *air density* $\rho=1.3$ (kg/m$^3$), the *air specific heat* at constant pressure $c_p=1.005$ (J/kg·°C), and the *Mixed Layer height* $H_{mix}$, provides an estimation of the $w^*$ parameter:

$$w^* = \left( \frac{g}{T} \frac{H_0}{\rho c_p} H_{mix} \right)^{1/3} \tag{3.9}$$

It is worthwhile to remark that the Mixed Layer height $H_{mix}$ is the height above ground level to which particle rise due to the buoyancy forcing. Generally $w^*$ varies from 0 to 1-2 m/s, according to the intensity of convective turbulent motion.

- ***Monin-Obukhov length L*** (m) is defined according to the following equation:

$$L = -(u^*)^3 \frac{\rho c_p T}{C_k g H_0} \tag{3.10}$$

$L$ is the height within PBL at which the contribution of mechanical turbulence is equal to the contribution due to convective turbulence. On sunny days, when convective fluxes are enhanced due to the solar radiation, ground surface temperature increases, as well as the sensible heat exchange between soil and atmosphere. Therefore $H_0>0$ and $L<0$ when unstable atmospheric conditions occur (heat flux from ground surface to atmosphere is assumed as positive).

SURFPRO (SURface-atmosphere interface PROcessor) (Arianet, 2006) is an atmospheric turbulence processor designed to estimate the two-dimensional fields of turbulence scale variables in the Planetary Boundary Layer (PBL) according to the Similarity Theory. The computation can be performed over a user-defined simulation domain by taking into account complex topography and land-use data. The output two-dimensional fields can be assigned to air quality models to simulate the PBL turbulent fields where pollutant dispersion occurs. SPRAY model requires $z_0$, $L$, $H_{mix}$, $w^*$, $u^*$ in order to compute the vertical profile of the statistical variables $T_{Lx}(x_z)$, $T_{Lv}(x_z)$, $T_{Lz}(x_z)$, $\sigma_{ux}(x_z)$, $\sigma_{uy}(x_z)$ and $\sigma_{uz}(x_z)$ that describe the stochastic fluctuations of particle motion (Eq. 2.4).

### *3.3.2 Surface parameters and land-use data*

For the computation of the aforesaid PBL scale variables SURFPRO requires the following input data: land-use, roughness length $z_0$, topography, cloud cover, relative humidity, pressure, precipitation, total and net solar radiation. Figure 8 summarises the whole input dataset for SURFPRO, including measurement units and options for variable format (time series or two/three-dimensional fields) and when a variable is required as input data or when it can be internally computed by SURFPRO algorithms:

**Table 3. Levels of meteorological data availability.**

| Level | |
|---|---|
| -1 | variable is internally computed by code; |
| 0 | assigned scalar value: variable is constant and uniform over whole domain; |
| 1 | Time series: variable is uniform over whole domain but varying in time; (free-format ASCII file - the column index of the variable has to be specified); |
| 2 | 2D fields (ADSO/bin-netCDF archive); |
| 3 | 3D fields (ADSO/bin-netCDF archive) |
| 4 | Time series: variable is uniform over whole domain and is used to adjust internally computed vales, e.g. to take into account the influence of clouds on incoming radiation; (free-format ASCII file - the column index of the variable has to be specified); |

**Table 4. Units for meteorological data.**

| | Level | | | | | | | | |
|---|---|---|---|---|---|---|---|---|---|
| **Variable** | **-1** | **0** | **1** | **2** | **3** | **4** | **Units** | | |
| Wind | | | | | ✓ | | m $s^{-1}$ | | |
| Temperature | | | ✓ | | ✓ | | K; °C | | |
| Cloud cover | | ✓ | ✓ | ✓ | | | *octals* {0, 1, ... 8} | *tenths* {0, 1, ... 10} | *fractions* {0, 0.1, ... 1} |
| Relative humidity | | ✓ | ✓ | | ✓ | | % | | |
| Precipitation | | ✓ | ✓ | ✓ | | | mm h-1 | | |
| Pressure | | ✓ | ✓ | | ✓ | | hPa | | |
| Total radiation | ✓ | | ✓ | | | ✓ | W $m^{-2}$ | | |
| Net radiation | ✓ | | ✓ | | | | W $m^{-2}$ | | |
| Mixing height | | ✓ | | ✓ | | | {0 = no; 1 = yes} | | |

*Figure 8. Overview of atmospheric variables managed by SURFPRO code.*

Moreover, the computational schemes for PBL scale variables also require values for the following parameters, which depend on the land-use of ground surface:

- ***Leaf Area Index (LAI)*** is a dimensionless quantity that characterizes plant canopies. In broadleaf canopies *LAI* is defined as the one-sided green leaf area per unit ground surface area, i.e. *LAI = leaf area / ground area* ($m^2_{leaf}$ / $m^2_{ground}$). In conifers, three definitions for *LAI* have been used:

- Half of the total needle surface area per unit ground surface area.
- Projected (or one-sided, in accordance to the definition for broadleaf canopies) needle area per unit ground area.
- Total needle surface area per unit ground area.

*LAI* values range from 0 (bare ground) to over 10 (dense conifer forests).

- ***Bowen ratio (B)***: is defined as the non-dimensional ratio between sensible $H_0$ (W/m$^2$) and latent $H_L$ (W/m$^2$) heat flux. *B* increases for dry surfaces and vice versa for wet surfaces.

$$B = \frac{H_0}{H_L} \tag{3.11}$$

- ***Albedo (a)*** represents the ratio between the reflected radiation and the whole incident radiation for a given surface; it is strictly dependent on land-cover.

- ***Mixed Layer height ($H_{mix}$)*** is the height above ground level to which particle rise due to the convective turbulence (buoyancy forcing). $H_{mix}$ value mainly depends upon the incident solar radiation at ground level; hence $H_{mix}$ shows a strong daily variation from dawn to nightfall, according to the presence of cloud cover. Moreover, due to the dependence on solar radiation, $H_{mix}$ is strongly variable also on seasonality.

Mixed Layer height ($H_{mix}$), net radiation, sensible and latent heat fluxes are internally computed by SURFPRO algorithms. In order to define values for *Leaf Area Index, Bowen ratio* and *Albedo*, land-use classification data for the study domain must be assigned to SURFPRO model.
For the present study land-cover images from CORINE database were adopted.
The Coordination of Information on the Environment (CORINE) programme started in 1985. CORINE was a European project working on remote sensing and monitoring activities for land-use and land-cover data for environmental protection purposes. First realization of the project goes back to 1990 (CLC90); subsequent updates refer to the year 2000 and 2006. As part of the CORINE project, a database of remote sensing images has been produced in order to release a classification of land-use for most European areas. Such database was released as a cartographic product, at a scale of 1:100 000; the classification scheme is articulated in 44 land-use classes.

SURFPRO embeds a library of values for the land-use variables, i.e. *Leaf Area Index*, *Bowen ratio* and *Albedo*, which are associated with a specific land-use class of CORINE classification scheme.

The land-use classification for the study domain is outlined from remote sensing images by means of a software tool for image processing. At first the user must select and clip the land portion dealing with the simulation domain; secondly land-use data are processed and exported in ASCII format file that must be provide to SURFPRO model as input data.

For the present study, remote sensing images from CORINE database were managed with the ENVI (ENVI, 2004) software tool. Further details about CORINE project can be found on line (EEA, 2015a) and Italian Major Institute for Environmental Research and Protection (ISPRA, 2015).

As well as MINERVE code, all the calculation options and paths for input data files can be managed through the graphical user interface, as shown in Figure 9: red circles show the starting-ending date and time of the simulation and the path for the input files.

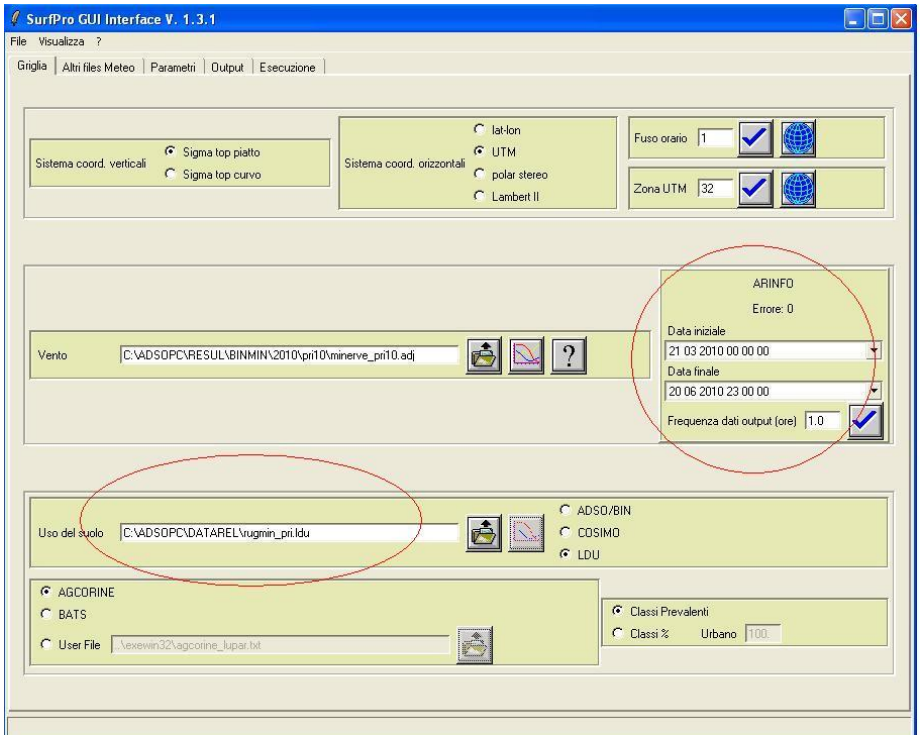


*Figure 9. Graphical user interface of SURFPRO code.*

### *3.3.3 Calculation workflow*

The whole computational procedure of SURFPRO involves the following steps:

1. Definition of surface parameters *Leaf Area Index*, *Bowen ratio* and *Albedo* according to the land-use classification. The input file for land-use classification embeds also *roughness length* values for each spatial cell. Surface parameters can be quite different within the study domain if land-use is heterogeneous.

2. Calculation of *net radiation* $R_N$ and *sensible heat flux* $H_0$ according to the following energy balance equation at ground surface:

$$R_n = H_0 + H_L + G \tag{3.12}$$

where $R_n$ is net solar radiation, $H_0$ is the sensible heat flux, $H_L$ is the latent heat flux and $G$ is the *heat flux into the ground*. All the aforesaid parameters are expressed in W/m$^2$. The calculation is performed by SURFPRO model according to the Holtslag and Van Ulden (1983) equation scheme, which is reported in the followings:

$$R_n = \frac{[(1-a)Q' + c_1 T^6 - \sigma_{SB} T^5 + c_2 C]}{(1+c_3)} \tag{3.13}$$

$$H_0 = \frac{(\iota - \psi)}{\iota} Q_{\uparrow} - \beta \cdot \psi \tag{3.14}$$

$$G_0 = K R_n \tag{3.15}$$

where:

- $a$ is the previously defined *albedo* parameter.
- $\sigma_{SB}$ is the *Stefan-Boltzmann constant* which is equal to $5.67 \cdot 10^{-8}$ ($W \cdot m^{-2} \cdot K^{-4}$).
- $K$ is a non-dimensional constant parameter varying in the range between 0.1 and 0.4 according to the land-use class.

- $c_1 = 5.31 \cdot 10^{-13}$ ($W \cdot m^{-2} \cdot K^{-6}$), $c_2 = 60$ ($K^4$), $c_3 = 0.12$, $\beta = 20$ ($W/m^2$), $\iota$ and $\psi$ are *empirical non-dimensional constants* that can be estimated according to the following equations:

$$\iota = 1 + \frac{\gamma}{\xi} \tag{3.16}$$

$$\psi = \frac{\iota \cdot Q_{\uparrow}}{[(1+B)(Q_{\uparrow} + \iota \cdot \beta)]} \tag{3.17}$$

where:

  - $Q_{\uparrow} = R_n - G_0$ ($W/m^2$);
  - $\gamma = 4 \cdot 10^{-4}$ [$(g_{water}/g_{air}) \cdot K^{-1}$] is the <u>*psychrometric constant*</u>, i.e. the ratio between the *specific heat* of dry atmospheric *air* and the *latent heat of water.*
  - The parameter $\zeta$ is defined in Holtslag and Van Ulden (1983) as $\zeta = \frac{\partial q_s}{\partial T}$ [$(g_{water}/g_{air}) \cdot K^{-1}$] and quantifies the variation of the *air specific humidity* $q_s$ $g_{water}/g_{air}$) with the *air temperature T* (K).
  - $Q' = R_N \left(1 - 0.75 \cdot C^{0.4}\right)$ ($W/m^2$) is the corrected value for net solar radiation $R_n$ according to the <u>*total fractional cloud cover*</u> *C* expressed in eighths of covered sky (*okta* is the common ordinary measurement unit).

3. Estimation of Mixed Layer height $H_{mix}$ according to the method proposed by Carson (1973) in which the daily evolution of $H_{mix}$ is computed by taking into account the development of convective turbulence. Others algorithms (Venkatram, 1980) are available in order to estimate $H_{mix}$ when convective turbulence is inhibited, i.e. at night time or when mechanical turbulence is predominant.

4. Calculation of two-dimensional fields for PBL scale parameters *u**, *L*, *w** according to the Similarity Theory. The outputs are stored in a binary output file that embeds also the meteorological fields (previously computed with MINERVE code), topography and roughness length $z_0$. It is worthwhile to remind that the output file must cover at least the whole spatial domain for SPRAY simulation.

# Chapter 4

# *Micro-Swift-Spray model*

## 4.1 Introduction

Micro-SWIFT-SPRAY (MSS) is a micro-scale atmospheric dispersion model aimed at taking into account urban canopy, i.e. buildings influence on pollutant dispersion patterns; the horizontal domain dimension is between 1-2 km and the horizontal grid step is of 1-5 m.

MSS was developed by coupling two originally distinct modelling tools: Micro-SWIFT and Micro-SPRAY. The former is a mass-consistent wind field model that was developed as new version of MINERVE code for micro-scale investigations; the latter, Micro-SPRAY, is a modified version of Lagrangian particle dispersion model SPRAY (Chapter 2) to be applied at urban micro-scale. Micro-SWIFT interpolates meteorological measurements and builds up the three-dimensional air circulation fields in presence of urban obstacles; Micro-SPRAY simulates the airborne pollutant dispersion patterns among buildings, according to the flow fields provided by Micro-SWIFT.

Simulation of airborne pollutant dispersion at urban micro-scale is a challenging task, because air circulation near buildings is affected more by turbulent fields, due to urban canopy, than by mesoscale meteorology (Hunter *et al.*, 1992).

Currently, state of the art of pollutant dispersion modelling at urban micro-scale is represented by Computational Fluid Dynamic (CFD) models. Nonetheless, despite of the reliability in reproducing turbulence features due to urban obstacles, CFD models are extremely demanding in computational resources, especially for two noteworthy applications: emergency response and long-term impact of ground-based emission source , as is the case of the present study.

MSS modelling system was developed as an intermediate quick response model to simulate flow field and dispersion processes at urban micro-scale, namely in presence of obstacles. MSS comparison with CFD numerical results and field experimental data (Armand *et al.*, 2006; Tinarelli *et al.*, 2008; Hanna *et al.*, 2011) shows a good reliability of the modelling system, and a considerable reduction of the required computational time. Tinarelli *et al.* (2008) showed that, in order to perform a simulation spanned over a period of 10 minutes, the required computational time is of hours (CFD) against minutes (MSS), with a negligible loss of result accuracy.

## 4.2 Micro-SWIFT

### *4.2.1 Overview of the code*

Micro-SWIFT is a mass-consistent micro-scale model for wind fields and turbulence computations. Similarly to the model MINERVE (Chapter 3), Micro-SWIFT generates the three-dimensional fields of wind speed, air temperature and relative humidity, by interpolating on-site measurements and vertical profiles. Wind field interpolation and adjusting techniques are the same as in MINERVE code (Paragraphs 3.2.3 and 3.2.4). In addition, Micro-SWIFT embeds some analytical schemes aimed at computing turbulence parameters and at modifying flow fields according to the urban canopy. The calculation procedure involves the following main steps:

1. *Interpolation of wind fields* <u>*without obstacles*</u>, by applying a two or three-dimensional interpolation method as described in Paragraph 3.2.3.

2. *Definition of zones* surrounding buildings, where flow fields are affected by urban obstacles.

3. *Wind field modification* within the perturbation zones.

4. *Adjustment of modified wind field*, by imposing mass conservation (Eq. 3.4 and 3.5) and impermeability conditions on both walls and rooftops of buildings.

In order to accomplish Step 2 and 3, Micro-SWIFT requires a block-shaped building arrangement within the simulation domain, in order to perform both perturbation zones definition and wind field modification, according to obstacle geometry.
When airborne pollutant dispersion is simulated in absence of urban obstacles, the statistical features of turbulent field, which are expressed by $T_{Lx}$, $T_{Lv}$, $T_{Lz}$, $\sigma_u$, $\sigma_v$ and $\sigma_w$ parameters (Paragraph 1.3), depend only upon land-use data, topography and thermal atmospheric stability, according to the PBL scale variables $L$, $H_{mix}$, $w^*$ and $u^*$ (Paragraph 3.3.1).
In presence of buildings, in order to take into account the contribution of urban canopy, the description of turbulence features requires the *diffusion turbulent coefficients* $K_x$, $K_y$ and $K_z$ ($m^2/s$) and the *dissipation rate of turbulent kinetic energy* $\varepsilon$ ($m^2/s^3$). Such parameters depend on how urban

obstacles affect the diffusion conditions and energy transfer between turbulent eddies at different spatial scales, according to the Kolmogorov theory (Kolmogorov, 1941).

Turbulence parameters $K_x$, $K_y$, $K_z$ and $\varepsilon$ are internally computed by Micro-SWIFT and then assigned in input to Micro-SPRAY. Figure 10 shows the Micro-SWIFT flow chart for input and output data.

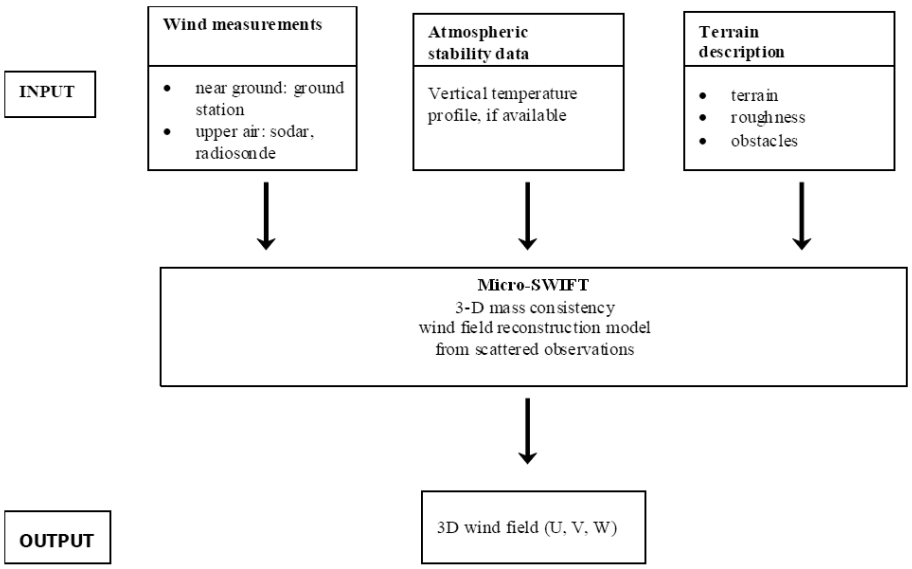


*Figure 10. Micro-SWIFT model flow chart for input and output data.*

### *4.2.2 Modelling building geometry*

Micro-SWIFT-SPRAY models buildings as vertical blocks with rectangular (parallelepipeds) or triangular footprint shape. Thus, the spatial definition of a given obstacle requires both the cartographic coordinates for the base vertices and the height above ground level of the obstacle rooftop. If the simulation is performed over a flat topography, the height of the rooftop above ground level corresponds to the rooftop height above the bottom of the simulation domain.

The rooftop of a building is modelled as a flat surface, and Micro-SWIFT code detects the correct geometry for an obstacle footprint shape (rectangular or triangular) as the best approximation for the plan view of a given building. The case of buildings with rectangular footprint shape, which is the most frequent, will be discussed in the followings; however, the computation schemes for rectangular footprint shapes are extendible also to the case of a triangular footprint shapes.

Urban Digital Elevation Models (UDEMs) are the main source for the geometrical features of building arrangement. UDEMs are generally obtained from Very High Resolution (VHR) satellite

stereo images, as provided e.g. by Ikonos, QuickBird or WorldView; ground sampling distance of VHR images is of about 1 m and spatial resolutions is of about 3-10 m (Krauss and Reinartz, 2011). Currently, more and more cities are moving towards the creation and the adoption of three-dimensional virtual city models, as a tool for data integration, harmonisation and storage (Agugiaro, 2014). UDEMs usually integrate detailed information about building characteristics, i.e. geometry, construction type and materials, with relevant data dealing with other geographical entities: hydrography, vegetation, power lines, street network, land-use and land-cover.

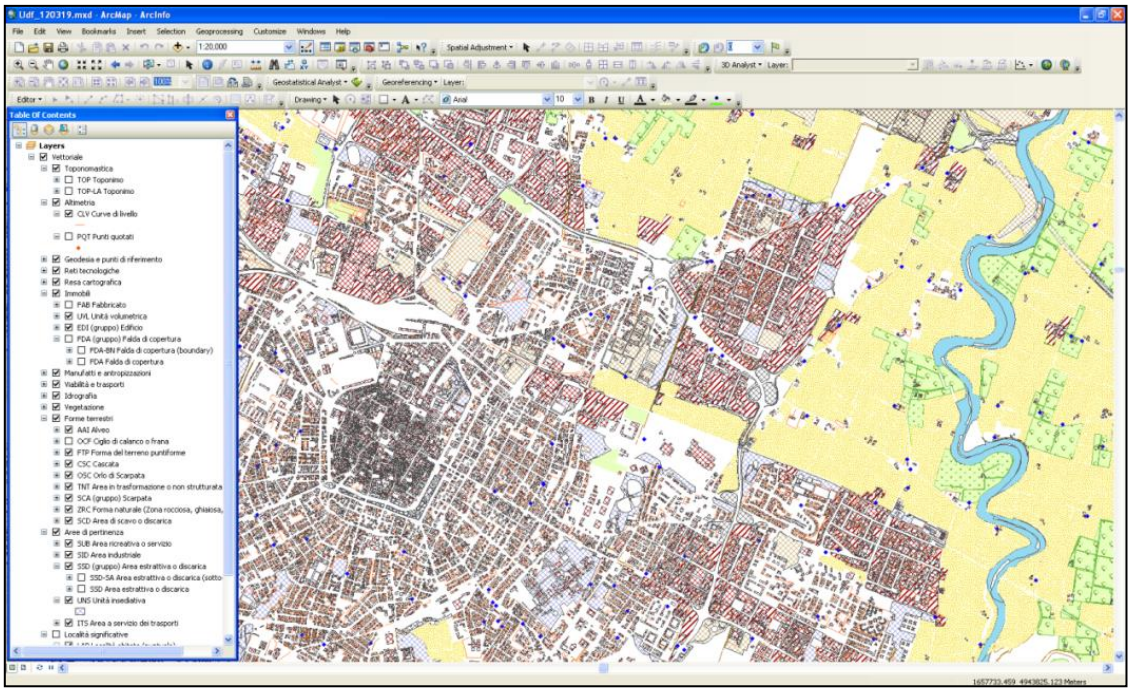

*Figure 11. Example of urban digital model in GIS environment: geographical data are organized according to different thematic layers.*

Several disciplines focussing on urban regeneration and sustainable development can benefit from the integrated management of territorial data from different kind of sources: land-use and urban and landscape planning, building energy improvement, hydro-geological risk assessment, etc.

UDEMs are generally supported by Geographical Information Systems (GIS) software tools; GIS allow to store, manage and analyse geographical data according to thematic layers, as shown in Figure 11; each layer embeds detailed information about a given territorial topic, e.g. hydrology, land-use, land-cover, infrastructures, building characteristics, terrain elevation, etc.

In order to provide the required building data to Micro-SWIFT code, user must firstly detect the study area in the digital cartographic support, by introducing the cartographic UTM coordinates of point corners for the simulation domain. The procedure allows at defining the South-West corner of

the simulation domain, which is also the origin of the Cartesian reference frame to be adopted both in Micro-SWIFT and in Micro-SPRAY models.

Secondly, the three-dimensional features of buildings are exported in a polygon vector shapefile, which must be converted in an ASCII-format file before being supply as input to Micro-SWIFT.

The geometry of the building array is embedded in the binary output file from Micro-SWIFT simulation, in addition to the interpolated and adjusted flow fields and temperature fields, and then assigned to Micro-SPRAY model.

In Micro-SPRAY pollutant particles are allowed to move in the gaps among buildings, and are supposed to bounce when crushing on building rooftops or fronts; each building is modelled by filling the grid cells that are occupied by the building itself (Figure 12). Therefore, the spatial grid resolution for the simulation domain is a key-element in order to achieve a good approximation of obstacles shape and arrangement.

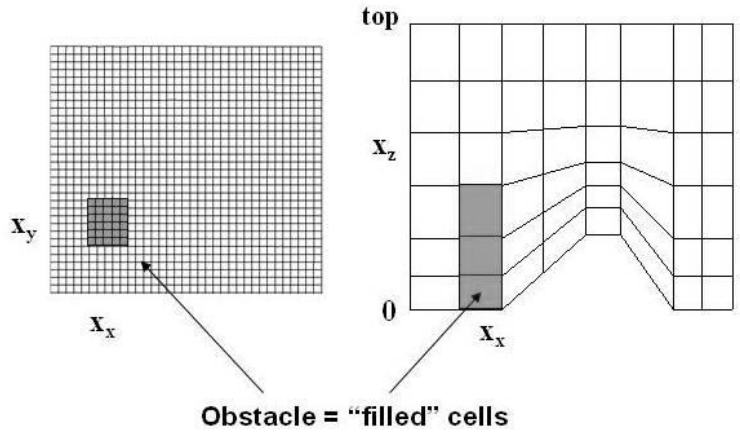


*Figure 12. Plan view (left) and vertical section (right) of Micro-SPRAY simulation grid; green "filled" cells reveal the presence of one obstacle.*

For the present study, building geometry was drawn out from an urban digital model, provided by Local Office for Cadastre and Topography (E. R., 2011) on a GIS support. The shapefile exportation, for building arrangement in the study area, was performed by means of the ArcGIS software package, developed by ESRI Company (ESRI, 2015); shapefile conversion was accomplished using a specific routine (Shaft programme), provided by Arianet Ltd and included in the AriaIndustry software package.

According to model developers advises (Arianet Ltd), the horizontal resolution of the simulation domain must be of 3 m at least, in order to attain an adequate approximation both for pollutant concentration fields and for building shape. Moreover, spatial features for Micro-SWIFT and Micro-SPRAY simulation domains are required to match, and the following values were adopted:

$L_x = L_y = 500$ m;

$n_x = n_y = 251$ (the Cartesian origin is included);

$\Delta x_x = \Delta x_y = 2$ m;

$L_z = 1000$ m above ground level;

$n_z = 30$.

$h_1 = 2$ m.

Symbol notation, which has been defined in Paragraph 2.3 for SPRAY model, is the same also for Micro-SWIFT-SPRAY modelling system. Figure 13 shows the plan view (left) and the three-dimensional block-shaped structure (right) of a building array; the study area is related to an urban district near the General Hospital of Modena, as will be discussed in Chapter 5.

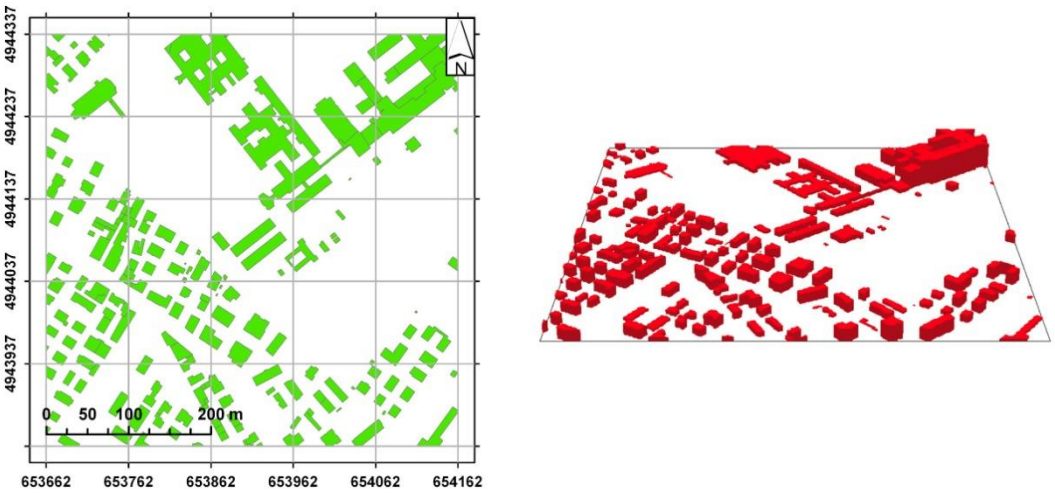


*Figure 13. Plan view (left) and the three-dimensional block-shaped structure (right) of the buildings within the study urban area.*

### *4.2.3 Zones definition around obstacles*

According to Step 2 (Paragraph 4.2.1), when the undisturbed wind flow interacts with an isolated building, Micro-SWIFT distinguishes three different perturbation zones attached to the obstacle: the ***displacement***, the ***cavity*** and the ***wake zone*** (Figure 14).

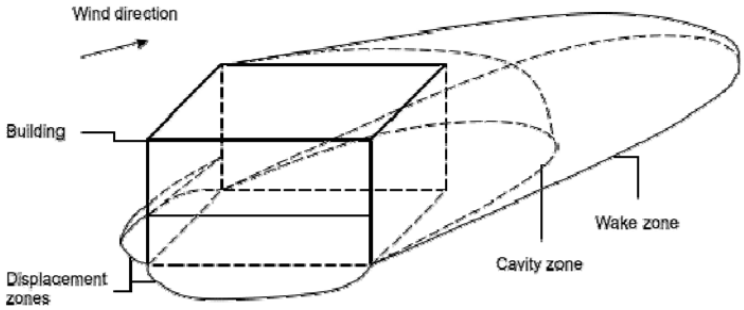


*Figure 14. General overview of zones attached to a building.*

In the *displacement zone*, which forms upwind the obstacle, atmospheric pressure increases and wind velocity decreases. Because of the turbulent recirculation eddy establishing in front of the building, the main wind flow is displaced from the ground and moved upward at a height of about $0.6H_b$, where $H_b$ is the upwind obstacle height. In the displacement zone the average wind field is supposed to be zero; thus, only turbulence is involved in pollutant dispersion.

Downwind the obstacle, two different zones are established: the *cavity zone*, where air circulation is reversed and the flow has a vortex shape, and the *wake zone*, which is a transition zone between the cavity zone and the undisturbed wind flow. Out of the wake zone, building influence on wind flow becomes negligible, and the undisturbed flow condition is re-established.

Figure 15 shows the main features of air circulation in the three zones, highlighting reversed flow circulation in the cavity zone.

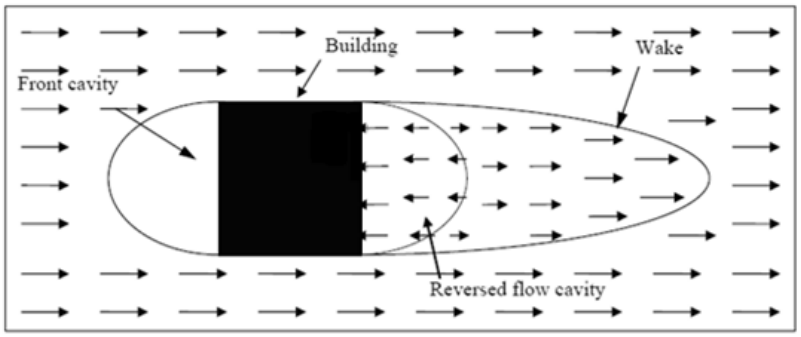


*Figure 15. Schematic plan view of airflow in the* displacement*, in the* cavity *and in the* wake *zones.*

### *4.2.4 Flow modification around obstacles*

Both zone definition and wind field modifications (step 2 and 3, Paragraph 4.2.1) are accomplished in Micro-SWIFT according to the analytical relations of Kaplan and Dinar (Kaplan and Dinar, 1996), who revised the historical study of Rockle (Rockle, 1990) about wind-obstacles interactions. Such scheme, which will be briefly described in the present section, was developed for the simplest case of a single isolated obstacle. More details about zone definition and flow modification for aggregates of buildings will be given in Paragraph 4.2.5.
Figure 16 shows the transversal section of a single building and of the relative attached zones.

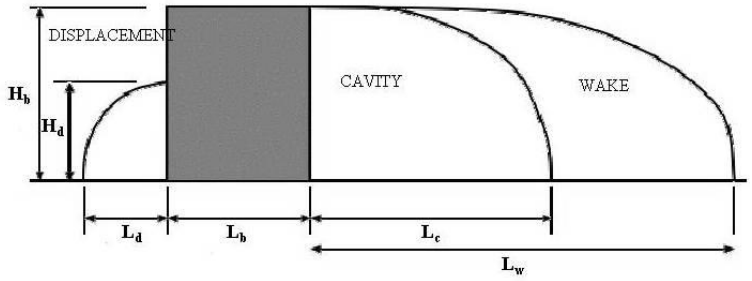


*Figure 16. Transversal section for* displacement, cavity *and* wake *zones.*

The symbols refer to the following dimensions (m):

- $L_d$, $H_d$, *length* and *height* of the ***displacement zone***.
- $L_c$, *length* of the ***cavity zone***.
- $L_w$, *length* of the ***wake zone***.
- $L_b$, $H_b$ building *length* and *height*.

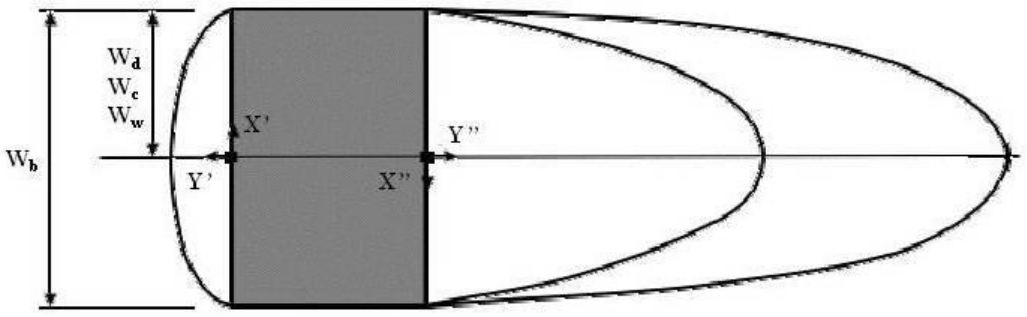


*Figure 17. Definition of dimensions and frames for* displacement, cavity *and* wake *zones.*

According to Figure 17, two Cartesian reference frames *x'y'z'* and *x''y''z''* are introduced, in order to define the analytical equations for the boundary surfaces of the three zones.
Equation for the boundary surface of displacement zone is defined in the *x'y'z'* reference frame; equation for the cavity and wake zones are defined in the *x''y''z''*. The following expression (Eq. 4.1) is valid for both the reference frames and shows an ellipsoidal shape.

$$\frac{X^2}{\left[W_i^2\left(1-\frac{Z^2}{H_i^2}\right)\right]}+\frac{Y^2}{L_i^2}=1 \tag{4.1}$$

Being $W_i$, $H_i$ and $L_i$ (m), with $i = d, c, w$, the *width*, the *height* and the *length* of the displacement, the cavity and the wake zones respectively, the related values are shown in Table 2.

| **Zone** | $L_i$ | $H_i$ | $W_i$ |
|---|---|---|---|
| ***Displacement*** | $L_d=\frac{2W_b}{[1+0.8(W_b/H_b)]}$ | $H_d=H_b$ | $W_d=0.5W_b$ |
| ***Cavity*** | $L_c=\frac{1.8W_b}{[(L_b/H_b)^{0.3}\cdot(1+0.24(W_b/H_b))]}$ | $H_c=H_b$ | $W_c=0.5W_b$ |
| ***Wake*** | $L_w=3L_c$ | $H_w=0.6H_b$ | $W_w=0.5W_b$ |

*Table 2. Summary of* $W_i$, $H_i$ *and* $L_i$ *for the* width, *the* height *and the* length *of* displacement, cavity *and* wake *zones respectively.*

Let $U_x(H_b)$ and $U_y(H_b)$ be the horizontal components of wind speed at the building top $H_b$, previously interpolated at Step 1 (Paragraph 4.2.1) in absence of obstacles. The corresponding modified values $U^m_x(x_z)$ and $U^m_y(x_z)$, at a height $x_z$ above ground level, are computed by means of Eq. 4.2, for the <u>*cavity zone*</u>, and Eq. 4.3, for the <u>*wake zone*</u> respectively.

$$U^m_{x,y}(x_z)=-U_{x,y}(H_b)\cdot\left(1-\frac{DL}{DN}\right)^2, \text{ for the } \textbf{\textit{cavity zone}}. \tag{4.2}$$

$$U^m_{x,y}(x_z)=U_{x,y}(H_b)\cdot\left(1-\frac{DL}{DN}\right)^{1.5}, \text{ for the } \textbf{\textit{wake zone}}. \tag{4.3}$$

In the displacement zone, according to the original Rockle formulation (Rockle, 1990), the average wind is supposed to be zero. Wind field inversion in the cavity zone (Paragraph 4.2.3) is obtained through the "-" sign in Eq. 4.2. Spatial parameters *DL* and *DN* are defined as in Figure 18.

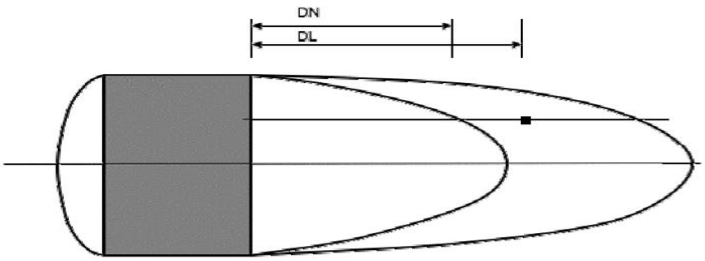


*Figure 18. Top view of an obstacle with definition of* DL *and* DN *parameters to be used in the* cavity *and* wake *zones computations.*

*DL* is the plan projection of the distance between a given grid node where Eqs. 4.2 and 4.3 are applied and the downwind front of the obstacle; *DN* is computed in the *x''y''z''* Cartesian reference frame according to Eq. 4.4.

$$DN(y'',z'') = L_c\sqrt{\left[1-\left(\frac{z''}{H_b}\right)^2\right]\cdot\left[1-\left(\frac{y''}{W_b}\right)^2\right]} - 0.5L_b \tag{4.4}$$

In Eq. 4.4 $L_b$ is the building length along wind direction, *DL* and *DN* parameters vary according to the *y''* and *z''* coordinates in the *x''y''z''* reference frame and *DN* is not dependent on *x''*.

In the <u>*wake zone*</u>, the wind is smoothly transitioned from the 0 value at the limit of the cavity zone (*DN = DL*) up to the value of the incoming undisturbed wind flow, when reaching the boundary of the wake zone.

In case of a wind not parallel to the obstacle, or in case of a triangular footprint shape, dimensions to be considered in equations for cavity and wake zone instead of $L_{c,w}$ and $W_{c,w}$ (Table 2) are length along wind direction and width along crosswind direction. Even the extension of the displacement zone is modified by multiplying $L_d$ for the squared cosinus of the angle between the normal to the side and the wind direction. In this case, only the wind component perpendicular to the building side is modified; the wind component parallel to the building side remains unchanged.

### *4.2.5 Zone definition and wind modification for group of obstacles*

The methodology described in Paragraphs 4.2.3 and 4.2.4, respectively for zone definition and wind modification, considers the simplest case of an isolated building.

The same approach is extended to the case of a building aggregate, which is a more frequent situation in urban environment. Therefore, Micro-SWIFT model detects the perturbation zones and perform wind field modifications for each single obstacle as in the case of an isolated building (Figure 14); in the case of two buildings that are aligned upwind, the displacement zone is defined along the sum of the building edges, and not for each single edge independently.

Nonetheless, when obstacles are very close, the main flow no longer penetrates into the gaps between buildings, but skims over the top; hence, the development of cavity and wake zones, as well as for an isolated obstacle, is not possible in this case. Interactions lead to the development of a particular zone between the buildings, defined as *skimming flow zone* by Kaplan and Dinar (Kaplan and Dinar, 1996). The development of the skimming flow zone occurs when the mutual *distance between two buildings* $L_s$ is lower than a reference distance $L_s$*, which is defined as:

$$\frac{L_s^*}{H_b} = 1.25 + 0.15\frac{W_b}{H_b} \quad \text{when} \quad \frac{W_b}{H_b} < 2 \tag{4.5}$$

$$\frac{L_s^*}{H_b} = 1.55 \quad \text{when} \quad \frac{W_b}{H_b} \geq 2 \tag{4.6}$$

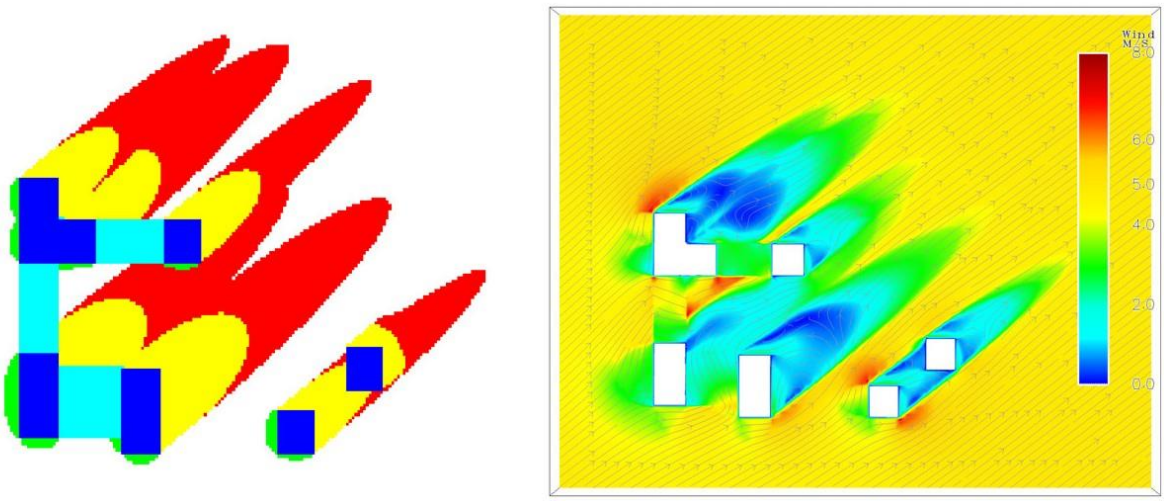


*Figure 19. Zone definition for an obstacle array (left); wind field after the adjustment (right).*

Figure 19 shows how perturbation zones are defined for a given obstacle array: *displacement zones* (green areas), *cavity zones* (yellow areas) and *wake zones* (red areas). In the *skimming zones* (cyan areas), where the development of cavity and wake zones is not possible, flow field is modified according to the following relations (Eqs. 4.7 and 4.8):

$$U_x^m(x_z) = -4U_x(H_b)\cdot\left[\frac{DL}{DN}\left(1-\frac{DL}{DN}\right)\right] \tag{4.7}$$

$$U_y^m(x_z) = \left|\frac{U_y(H_b)}{2}\cdot\left(1-\frac{2DL}{DN}\right)\right|\cdot\left(1-\frac{2DL}{DN}\right) \tag{4.8}$$

$U_x(H_b)$ and $U_y(H_b)$ are the horizontal reference components of wind speed at the building top $H_b$; *DL* and *DN* are defined as in Figure 20. In case of an incoming wind not orthogonal to the skimming zone, only the wind component perpendicular to the building side is modified as specified above. The wind component parallel to the side remains unchanged.

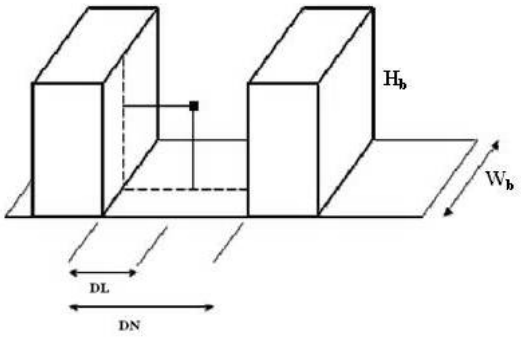


*Figure 20.* $H_b$, $W_b$, DL *and* DN *parameters definition for an array of two obstacles.*

The air recirculation phenomena among buildings, which are generally known as *urban canyons*, are quite complex to be predicted; nevertheless, as shown in the literature by many authors (Hotchkiss and Harlow, 1973; Yamartino and Wiegard, 1986; Hunter *et al.*, 1992; Vardoulakis *et al.*, 2003), such phenomena deeply affect pollutant dispersion at urban micro-scale.

### *4.2.6 Rooftop zone wind modification*

A fifth perturbation zone is established over building rooftops, which are supposed to be flat in Micro-SWIFT model. As shown in Figure 21, the dimensions of rooftop recirculation zone are small, if compared to building dimensions; hence a fine resolution is required in order to get enough grid points for an exhaustive description of air circulation.

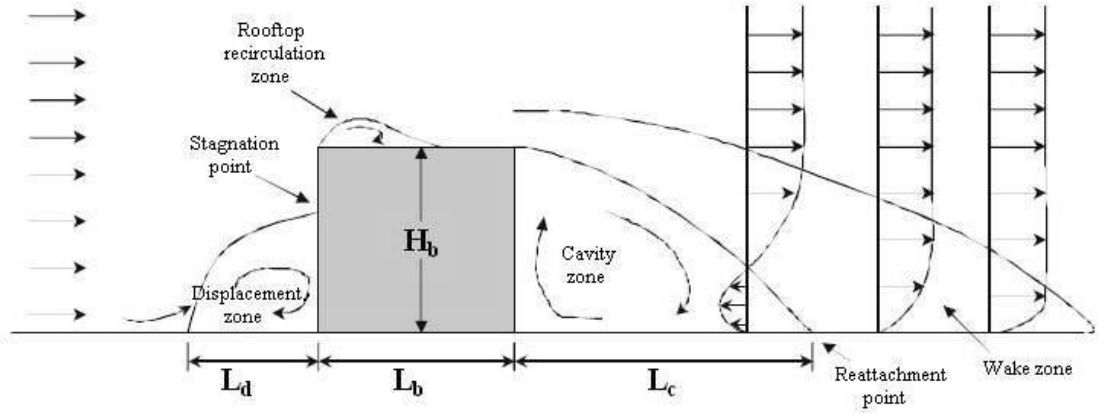


*Figure 21. Vertical cross section of perturbation zones and flow recirculation around a building.*

As shown in Figure 22, a semi-elliptical shape vortex is established from the rooftop towards a height equal to $H_{CM}$, and the velocity profile has a linear trend.

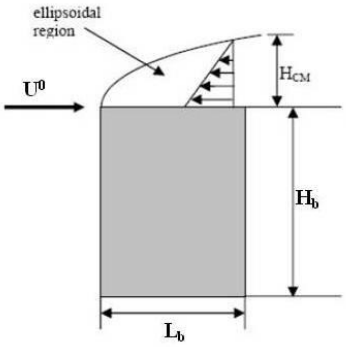


*Figure 22. Vertical cross section of rooftop recirculation zone and velocity profile.*

According to the geometrical parameters $H_b$ (building height) and $H_{CM}$, the horizontal components of velocity $U^m{}_x(x_z)$ and $U^m{}_y(x_z)$ in the rooftop zone can be computed by means of the following formula proposed by Wilson (1979):

$$U^{m}_{x,y}(x_z) = U^{0}_{x,y} \cdot \left( \frac{H + H_{CM} - x_z}{H_{CM}} \right) \tag{4.9}$$

In Eq. 4.9 $U^0_x$ and $U^0_y$ are the horizontal components of the upstream incident wind velocity $U^0$, and $U^m_{x,y}(x_z)$ vary from 0 to $U^0_{x,y}$. When $x_z = H_b + H_{CM}$, i.e. at the top of the recirculation zone, $U^m_{x,y}(x_z)$ is equal to *0*; when $x_z = H_b$, i.e. at the leading edge of the building, $U^m_{x,y}(H_b) = U^0$, and air recirculation is thus of opposite direction, but of equal magnitude to the upstream incident wind. The height $H_{CM}$ and the length $L_{CM}$ of the vortex can be estimated as follows:

$$H_{CM} = 0.22\text{R} \tag{4.10}$$

$$L_{CM} = 0.9\text{R} \tag{4.11}$$

$$R = 0.67B_s \cdot 0.33B_l \tag{4.12}$$

$$\varphi_c = 2.94 \cdot e^{(0.0297 \cdot \omega)} \tag{4.13}$$

In Eq. 4.12, $B_s$ and $B_l$ are the smaller and the larger of upwind building height or width respectively. Such method is applicable when the wind incident angle $\omega$ falls in the range among 70° and 90°; when $\omega$ falls in the range among 30° and 70°, a so-called "*delta-wing*" vortex forms on the rooftop. According to Banks *et al*. (Banks *et al*., 2001), the height $H_{CM}$ and the length $L_{CM}$ of the vortex can be estimated from the *vortex core angle* $\varphi_c$, formed from the vortex core axis line and the leading edge of the roof, as shown in Figure 23.

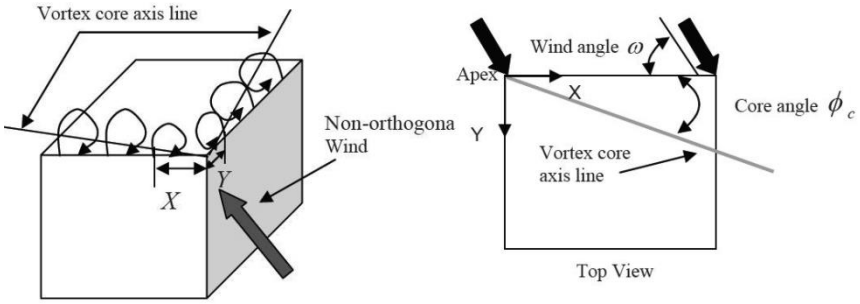


*Figure 23. "Delta-wing" vortex and core angle $\varphi_c$ for a wind incident angle $\omega$ range 70° to 90°.*

The vortex core angle $\varphi_c$ depends upon the wind incident angle $\omega$ according to the exponential relation in Eq. 4.13 (Banks *et al*., 2001). Eqs. 4.14 and 4.15 give the heights $H_{CMx,y}$ and the lengths $L_{CMx,y}$ of the vortex region, according to the local plan Cartesian reference frame *Oxy* of Figure 23.

$$L_{CMx} = \frac{H_{CMx}}{2} = 2X \tan(\varphi_c) \tag{4.14}$$

$$L_{CMy} = \frac{H_{CMy}}{2} = 2Y \tan(\varphi_c) \tag{4.15}$$

where $X$ and $Y$ are the distances of the grid node from the apex of the rooftop edge of the building. A maximum value for $L_{CMx}$ and $L_{CMy}$ has been set to $L_{max} = 10\ m$, so that the vortex zone does not grow indefinitely. As in the case of a wind incident angle between 70° and 90°, the velocity profile is linear, but only the perpendicular component to the side along which the vortex grows is considered; the other component is set equal to 0.

Figure 24 shows the example case of a wind incident angle $\omega = 45°$.

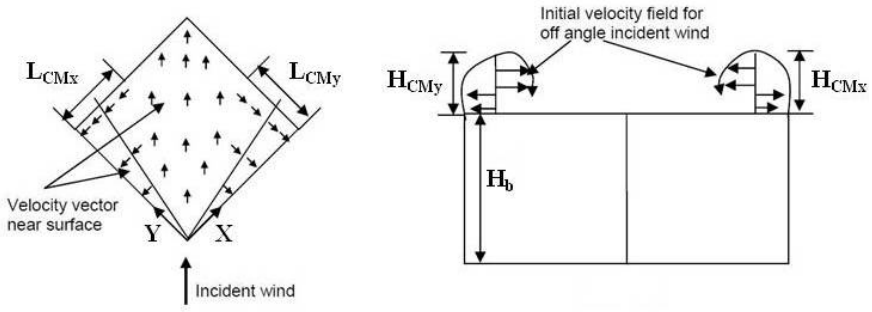


*Figure 24. Plan view (left) and vertical section (right) of wind field for* ω = 45°.

### *4.2.7 Estimation of turbulence parameters $K_x$, $K_y$, $K_z$ and ε*

Due to the interaction of undisturbed wind flow with buildings, the perturbation zones are affected also by the development of a turbulence field, which is strictly dependent on the urban canopy, i.e. building arrangement and geometry. Micro-SWIFT-SPRAY distinguishes the contribution of *background turbulence* from *obstacle-induced turbulence* in influencing air recirculation and pollutant dispersion at urban micro-scale: the former depends on atmospheric stability conditions and surface roughness; the latter depends on urban canopy.

The turbulence field in the perturbation zones surrounding obstacles involves the three-dimensional fields of the *diffusion turbulent coefficients* $K_x$, $K_y$ and $K_z$ ($m^2/s$) and the *dissipation rate of turbulent kinetic energy* $\varepsilon$ ($m^2/s^3$). The computational approach adopted by Micro-SWIFT is similar to the *k-ε* turbulence model, widely adopted in CFD simulations (Wright and Easom, 2003).

As shown in Paragraph 4.2.3 and 4.2.4, the interaction between undisturbed wind flow and urban obstacles involves perturbations of the wind fields surrounding obstacles. Moreover, in the perturbation zones, air circulation is highly unstable because of the strong spatial variation of average wind speed values and leads to the development of a turbulent field. The spatial variations of average wind speed components $\bar{u}_x$, $\bar{u}_y$ and $\bar{u}_z$, involve momentum transport in turbulent flow; thus, a state of stress is generated. At a given point *P(x,y,z)*, in a Cartesian reference frame *Oxyz*, the state of stress of a given turbulent fluid is fully characterized by the *Reynolds stress tensor* τ.

$$\tau = \begin{bmatrix} \tau_{xx} & \tau_{xy} & \tau_{xz} \\ \tau_{yx} & \tau_{yy} & \tau_{yz} \\ \tau_{zx} & \tau_{zy} & \tau_{zz} \end{bmatrix} \tag{4.16}$$

Each of the nine component $\tau_{ij}$ provides an estimation of the momentum flux in turbulent flow, with respect to the Cartesian directions $i,j = x, y, z$. In case of isotropic turbulence, i.e. when the statistical features are equal for all directions, $\tau$ becomes a diagonal tensor; hence, only the diagonal elements are different from zero, i.e. $\tau_{ij} = 0$ when $i \neq j$.

In Micro-SWIFT model the diffusion coefficients $K_x$, $K_y$ and $K_z$ are computed according to the *Mixing length method*, in which the diagonal elements $\tau_{xx}$, $\tau_{yy}$, $\tau_{zz}$ are related respectively to $K_x$, $K_y$ and $K_z$, by means of the ***Prandtl mixing length***, under the assumption of isotropic turbulence. The methodology, as revised by McDonough (2007), is based on the Prandtl theory for turbulence (Prandtl, 1925). Prandtl mixing length $l_m$ (m) can be defined as *"the distance over which a hypothesized turbulent eddy retains its identity"* (McDonough, 2007), i.e. the average distance

travelled by turbulent eddies retaining its motion properties, i.e. before mixing with the surrounding fluid and giving rise to momentum transfer.

In Micro-SWIFT model, mixing length is computed according to the distance between a given node of the calculation grid and the closer solid boundary, being a building front or the ground surface. The maximum allowed value is $l_m = 100\ m$, being 100 m the maximum scale of turbulent eddies according to the present computation scheme.

The calculation of the dissipation rate of turbulent kinetic energy $\varepsilon$ is accomplished by Micro-SWIFT as in $k$-$\varepsilon$ models, i.e. by estimating the energy dissipation phenomena in turbulence fields.

From an energetic point of view, the turbulence field due to the urban canopy involves the development of vortices at different spatial scales and energy transfer from larger to shorter scale eddies, according to the Kolmogorov theory (1941). Large scale eddies extract kinetic energy from average wind flow, and then energy is progressively transferred to short scale eddies.

According to Taylor theory (Taylor, 1921) a length $\eta$ (m), denoted as ***Taylor microscale***, can be defined; $\eta$ is the scale for eddies dimensions at which turbulence diffusion becomes negligible, and viscous phenomena lead to the dissipation of turbulent kinetic energy in heat. Eq. 4.17 defines the Taylor microscale $\eta$:

$$\eta = \left( \frac{\nu k}{\varepsilon} \right)^{1/2} \tag{4.17}$$

where $k$ ($m^2/s^2$) is the *turbulent kinetic energy*, $v$ ($m^2/s$) is the *cinematic viscosity* of the fluid and $\varepsilon$ is the dissipation rate of turbulent kinetic energy.

The following are typical values for the aforesaid parameters (Sozzi, 2003): $k \approx 10^0$ ($m^2/s^2$), $v = 10^{-5}$ ($m^2/s$), $\varepsilon = 10^{-3}$ ($m^2/s^3$), thus $\eta \approx 10^{-1}$ (m). According to the methodology of $k$-$\varepsilon$ turbulence models, $\varepsilon$ is estimated from the *Reynolds average Navier-Stokes* equations (RANS), which can be obtained from the Navier-Stokes equations by applying the Reynolds averaging procedure (McDonough, 2007), in order to provide an exhaustive description of momentum flux and energy transfer in turbulent motion. Further details can be found in the Micro-SWIFT user guide (Aria Technologies, 2010).

## 4.3 Micro-SPRAY

### *4.3.1 Overview of the code*

Micro-SPRAY model is a simulation tool for airborne pollutant dispersion at urban micro-scale, i.e. in the gaps among buildings; the code is designed to be coupled with Micro-SWIFT model, which provides input wind, and turbulence fields, by taking into account obstacle perturbations on airflow.
Being Micro-SPRAY code designed as an advanced version of local scale model SPRAY, the spatial and temporal structure remains unchanged from previous version (Paragraph 2.3 and 2.4.). Moreover, Micro-SPRAY model implements the same equation schemes both for particle motion and plume rise phenomenon (Paragraph 2.2 and 2.5); in addition to SPRAY code, the interactions between particles and urban obstacles are reproduced by extending to the obstacle fronts the same particle bouncing scheme originally developed for topographic surface.
Similarly to SPRAY model, Micro-SPRAY simulation domain consists of a three-dimensional grid, divided in spatial cells (Paragraph 2.3, Figure 5); pollutant concentration fields are periodically computed by sampling particle positions within each domain cell, by applying the same formula as in Eq. 2.10. Vertical and horizontal structure of Micro-SPRAY simulation domain are generated according to the same parameters described in Paragraph 2.2, i.e. $L_x$, $L_y$, $L_z$, $\Delta x$, $\Delta y$, $n_x$, $n_y$, $n_z$ and $h_1$; horizontal domain dimensions are up to 1-2 km and grid resolution is of 1-5 m.
Besides, since the dispersion patterns at micro-scale are influenced more by urban canopy than by topography, the calculations can be performed on a flat topography domain.
The temporal structure of Micro-SPRAY model involves the same parameters $\Delta t_{em}$, $\Delta t_{sync}$ and $\Delta t_{samp}$ of SPRAY model (Paragraph 2.4.), in order to define the time period for particle emissions ($\Delta t_{em}$), synchronization of particle motion equations ($\Delta t_{sync}$) and the samplings of particle positions ($\Delta t_{samp}$).
Further details can be found in the Micro-SPRAY user guide (Arianet, 2010).

### *4.3.2* Background *and* local *turbulence fields*

In SPRAY model, the calculation of the stochastic fluctuation terms $u_i'$ (Eq. 2.4, Paragraph 2.2) requires the statistical features of turbulence fields, which consist of the *Lagrangian time scale* $T_{Li}$ and the velocity variances $\sigma_{ui}$ (Paragraph 1.3), with $i = x, y, z$ Cartesian directions.
In Micro-SPRAY model, $u_i'$ is computed in the same way by means of Eq. 2.4; thus, the statistical parameters $T_{Li}$ and $\sigma_{ui}$ are still required.
When atmospheric circulation and pollutant dispersion are simulated in absence of urban canopy, namely at local scale, turbulence is only affected by thermal atmospheric stability (convective turbulence) and by wind flow interactions with topography. Such contribution is denoted in Micro-SPRAY as *background turbulence*, and it is completely stand-alone from urban canopy.
Conversely, if pollutant dispersion is simulated at urban micro-scale, the *obstacle-induced* or *local turbulence* (Paragraph 4.2.7) cannot be overlooked in the calculation of $T_{Li}$ and $\sigma_{ui}$ parameters.
The distinction operated by Micro-SPRAY between *background* and *local turbulence* lead to the application of two different calculation schemes:

- The *local* turbulence contribution consists in the three-dimensional field of *local velocity variances* $\sigma_{ux}^{local}$, $\sigma_{uy}^{local}$ and $\sigma_{uz}^{local}$ (m/s) that are estimated according to the following equation scheme, as suggested by Rodean (1996):

$$\sigma_{ux}^{local} = \frac{1}{2} C_0 K_x \varepsilon^{0.25}; \qquad \sigma_{uy}^{local} = \frac{1}{2} C_0 K_y \varepsilon^{0.25}; \qquad \sigma_{uz}^{local} = \frac{1}{2} C_0 K_z \varepsilon^{0.25} \qquad (4.18)$$

  Three-dimensional fields of *diffusion coefficients* $K_x$, $K_y$ and $K_z$ ($m^2/s$) and *dissipation rate of turbulent kinetic energy* $\varepsilon$ ($m^2/s^3$), previously estimated By Micro-SWIFT code (Paragraph 4.2.7), are required; $C_0 = 2$ is an *universal empirical* non-dimensional *constant*.

- The *background* turbulence contribution involves vertical profiles of *background velocity variances* $\sigma_{ux}^{bg}$, $\sigma_{uy}^{bg}$ and $\sigma_{uz}^{bg}$ (m/s). The calculation is performed, both in SPRAY and Micro-SPRAY models, by applying the Hanna scheme (Hanna, 1982), which is based on the turbulence scale variables for PBL, namely $z_0$, $L$, $H_{mix}$, $w^*$, $u^*$.
  Nonetheless, because of the restriction of the spatial domain by shifting from a locale-scale to a micro-scale simulation, PBL scale variables are assumed to be constant over the whole

domain; hence, Micro-SPRAY model requires a time series for $z_0$, $L$, $H_{mix}$, $w^*$, $u^*$ values, but not a two dimensional field.

For the present micro-scale study, the input turbulence variables for PBL ($z_0$, $L$, $H_{mix}$, $w^*$, $u^*$) were simulated by means of meteorological mesoscale model CALMET (Deserti *et al.*, 2001), and provided by the Local Environmental Agency (ARPA). CALMET simulations for meteorological data, i.e. mesoscale vertical profiles, were accomplished over a large simulation domain with a large meteorological dataset (Paragraph 3.2.2). Likewise, two-dimensional fields of turbulence scale parameters were estimated on a mesoscale computational domain; subsequently, the required time series for $z_0$, $L$, $H_{mix}$, $w^*$, $u^*$ values was extracted at a point in correspondence of the study area.

It is worthwhile to remind that, as previously shown for other meteorological input data, even the time series of $z_0$, $L$, $H_{mix}$, $w^*$, $u^*$ is required to be spanned over the whole simulation period (usually one day for a micro-scale study); in addition, its time resolution must match closely with model resolution for concentration computing (generally one hour).

By summing local and background turbulence contributions, the *velocity variances* $\sigma_{ux}^{sum}$, $\sigma_{uy}^{sum}$ and $\sigma_{uz}^{sum}$ (m/s) are obtained; the calculation is performed over the whole simulation domain, according to Eqs. 4.19. Hereafter, *Lagrangian time scales* $T_{Lx}^{sum}$, $T_{Ly}^{sum}$ and $T_{Lz}^{sum}$ (s) are computed through the substitution of Eqs. 4.19 in Eqs. 4.20.

$$\sigma_{ux}^{sum} = \sqrt{[(\sigma_{ux}^{local})^2 + (\sigma_{ux}^{bg})^2]} \tag{4.19}$$

$$\sigma_{uy}^{sum} = \sqrt{[(\sigma_{uy}^{local})^2 + (\sigma_{uy}^{bg})^2]}$$

$$\sigma_{uz}^{sum} = \sqrt{[(\sigma_{uz}^{local})^2 + (\sigma_{uz}^{bg})^2]}$$

$$T_{Lx}^{sum} = \frac{2(\sigma_{ux}^{sum})^2}{C_0 \varepsilon}; \qquad T_{Ly}^{sum} = \frac{2(\sigma_{uy}^{sum})^2}{C_0 \varepsilon}; \qquad T_{Lz}^{sum} = \frac{2(\sigma_{uz}^{sum})^2}{C_0 \varepsilon} \tag{4.20}$$

# Chapter 5

# *The case study : pollutant source description*

## 5.1 The urban context and local meteorology

The case study deals with the simulation of airborne pollutant dispersion from a new power plant consisting of a tri-generation unit, equipped with a four-stroke engine, three conventional boilers and two steam generators. All devices are powered by methane gas. The new power plant will be installed in the neighbourhood of the General Hospital of Modena "Policlinico" and the proposer is the Local Health Service Agency (AUSL). The plant is designed to fulfil the energy demand of the General Hospital and to replace an existing and obsolete power plant with three boilers and two industrial steam generators, all also supplied by methane gas. As shown in Figure 25 the power plant is sited close to a densely populated urban area within the urban district of Modena.

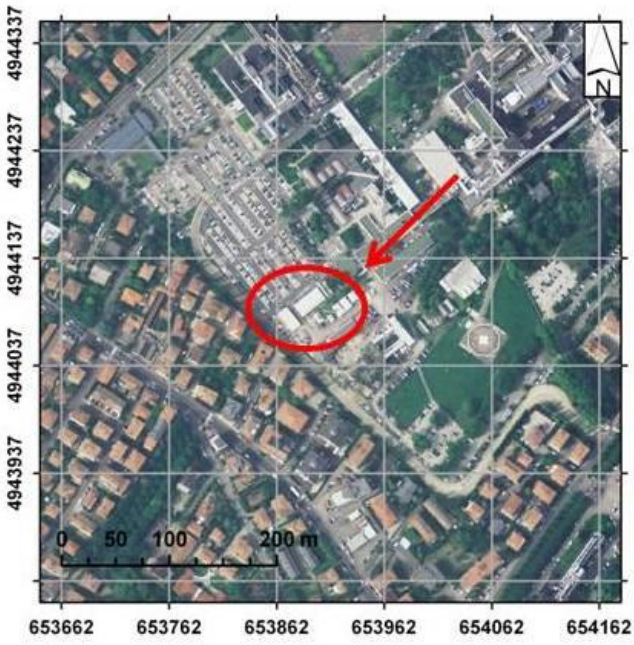


*Figure 25. Modena General Hospital "Policlinico" and the adjacent residential urban area; the position of the existing plant, which will be replaced by new devices, corresponds to the red circle shown by the arrow.*

Modena (185 243 inhabitants) is a town in the centre of the Po Valley (34 m a.s.l.) in Northern Italy, that has a large number of industrial activities (ceramics, automotive, chemistry and food) and high population density. It follows that pollutant emissions from the studied power plant are expected to impact on an urban environment already highly exposed to atmospheric pollution due to anthropogenic emissions, i.e. vehicular traffic, industry and household heating systems.

Moreover, typical meteorological conditions in Modena and in the whole Po Valley are often unfavourable to atmospheric pollutant removal, due to the high frequency of thermal inversion and low wind events, i.e. wind speed values less than 2 m/s, or calms.

The most critical meteorological conditions in the Po Valley are experienced in winter season (Ferrero *et al.*, 2011). Table 1 shows average monthly values for wind speed, air temperature, relative humidity and Mixed Layer height ($H_{mix}$) for year 2010 that significantly represents typical local atmospheric conditions.

It is noticeable that lowest values for average wind speed and $H_{mix}$ were observed in winter season.

| MONTH | Temperature (°C) | Relative humidity (%) | Wind speed (m/s) | $H_{mix}$ (m) |
|---|---|---|---|---|
| **Jan** | 3.2 | 85.9 | 1.23 | 175 |
| **Feb** | 5.6 | 84.1 | 1.82 | 282 |
| **Mar** | 9,4 | 72,7 | 1,91 | 560 |
| **Apr** | 15.0 | 63.5 | 2.04 | 676 |
| **May** | 19.1 | 61.3 | 2.28 | 836 |
| **June** | 23.8 | 58.1 | 2.18 | 906 |
| **July** | 27.7 | 50.4 | 2.29 | 929 |
| **Aug** | 25.3 | 58.3 | 1.69 | 761 |
| **Sept** | 19.9 | 66.4 | 1.55 | 533 |
| **Oct** | 13.8 | 77.8 | 1.43 | 380 |
| **Nov** | 10.2 | 89.8 | 1.72 | 255 |
| **Dec** | 3.1 | 88.0 | 1.85 | 203 |
| **Average 2010** | 14.7 | 71.3 | 1.83 | 543 |

*Table 3. Average monthly values for meteorological parameters for year 2010.*

Meteorological data, i.e. air temperature, wind speed and relative humidity, are by courtesy of Osservatorio Geofisico of Modena and Reggio Emilia University. Mixed Layer height values are by courtesy of Idro-Meteorological Service of Local Environmental Agency (ARPA).

Figure 26 shows a graphical comparison between average monthly values of air temperature and $H_{mix}$ for the year 2010; the similarity in their monthly pattern is quite evident.

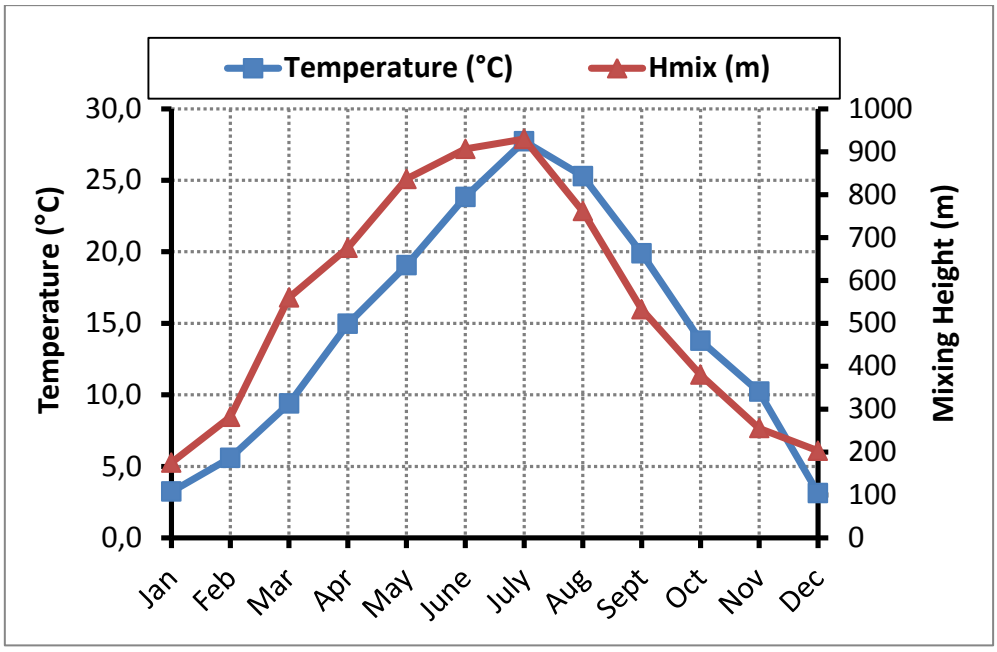


*Figure 26. Monthly pattern for average values of air temperature and $H_{mix}$ in Modena.*

Moreover, the frequency of low wind events (wind speed < 2 m/s) in winter 2010 is equal to 74 %. Maximum hourly value for Mixed Layer height in winter 2010 ranged between 250-600 m, reaching 800 m in late February, consistently with typical Mixed Layer height observations within the Po valley (Ferrero *et al*., 2011; Pernigotti *et al*., 2012).

Furthermore, in winter season, most critical levels of pollutant emission are expected due to the highest fuel consumption for methane fuelled plants and household heating systems. Therefore, the study of atmospheric pollutant dispersion in the present work is mainly focused on winter season, when the most unfavourable conditions for air quality are expected. Meteorological data involve the whole year 2010 as a test period.

## 5.2 Cogeneration: energy benefits and environmental aspects

A key element of environmental sustainability is the renewal of conventional energy production systems, still heavily dependent on fossil fuels, by developing new technologies for energy generation, with high efficiency and low environmental impact.

Combined heat and power (CHP) generation, or cogeneration, is the simultaneous production of heat and electricity in only one process (Dharmadhikari, 1997).An electricity production device, from a primary energy source, is combined with heat recovery equipments that allow to use the thermal energy that cannot be converted in electric energy, due to the limitations imposed by Thermodynamics Second Law. In some cases, the heat recovery system of a CHP power plant is combined with an energy absorber, i.e. a cooling system to meet the cooling needs for summer season. Such facilities are named *tri-generation units*.

CHP technology has undergone a considerable development, since the self-production of electric power enables the satisfaction of energy demand of small-size users, i.e. schools and hospitals.

The economic benefits due to CHP technology have been widely investigated in the literature (Schicktanz *et al*., 2010; Armanasco *et al*., 2012); some authors also proposed optimization models for CHP operational costs (Cho *et al*., 2009) or cost-benefit analysis, with the aim of assessing the technical-economic feasibility of CHP power plants (Ferreira *et al*., 2014).

Although a cogeneration unit is essentially based on an internal combustion engine, usually powered by methane gas eventually produced by biomass fermentation, the heat recovery system allows achieving higher energy conversion efficiencies than in a conventional power plant, where only the electric energy production can be achieved.

Due to the combined generation of heat and electricity, both thermal and electric power is taken into account in the calculation of the global energy conversion efficiency that results to be increased in CHP plants. In fact, assuming to produce equal amounts of thermal and electric power via two separate conventional plants for heat and electricity generation respectively, it is demonstrable that the overall energy conversion efficiency decreases respect to the production of the same energy amount by a CHP plant (Comini *et al.*, 2005).

It has been also estimated that CHP technology, if compared to the energy production in separate ways, leads to a primary energy saving of 35-40% (Caruso *et al.*, 2006). Consequently, the thermodynamic convenience of CHP facilities is quite evident.

According to the Intergovernmental Panel on Climate Change (IPCC), current CHP designs can boost overall conversion efficiencies to over 80 %, leading to cost savings (IPCC, 2007), whereas it never exceeds 40-42 % even for high performance conventional power plants (Cantore, 1999).

In addition, a large-scale diffusion of CHP technology in Italy would lead to a reduction in electricity energy demand from Italian Electric Energy Network (IEEN in the followings), whose plant facilities are still heavily dependent on fossil fuel technologies with high atmospheric impact due to the pollutant emissions, mainly $NO_x$, $SO_x$ and PM10, and greenhouse gas (GHG) emissions. The use of cogeneration facilities is promoted by Italian regulations (D.L. 20/07) that transposed the European Directive 2004/8/EC (E.U., 2004) for the preferment of cogeneration as a low carbon technology. European Commission (E.U., 2009) promotes the "cogeneration" in a perspective of achieving the three long-term goals set out by 2009/29/EC Directive: 20% increase of energy efficiency, 20% increase in use of renewable energies, at least 20% reduction in greenhouse gas (GHG) emissions below 1990 levels by 2020. According to the European Environmental Agency estimation (EEA, 2015b), by doubling the share of cogeneration in gross electricity production for EU-27 from 1994 to 2010, more than 65 Mt of $CO_2$ emissions per year might have been avoided from 2010.

Pollutant ($NO_x$, $SO_x$ and PM10) and GHG emissions due to conventional electricity generation are avoided with self-production of electric power by means of CHP plants. Nevertheless, the effect of a similar reduction in $NO_x$, $SO_x$ and PM10 emissions improves the air quality in the surroundings of the electric energy production plant (Levy and Spengler 2002), that in most cases is very far away from the sites of end use of the electricity, whereas the effects of the reduction in GHG emission have a relevance on a global scale.

Conversely, stack emissions from cogeneration facilities are expected to fall in the surrounding of the plant, hence the impact on local air quality of a tri-generation plant must be assessed by the evaluation of its stack emissions rates. Such an impact cannot be obviously neglected, regardless of the technical and economical convenience on the development of CHP technology.

As mentioned in the previous section 5.1, the new power plant of this case study consists of a tri-generation unit equipped with a four stroke engine, three conventional boilers and two steam generators (auxiliary devices), all supplied by methane gas. The tri-generation unit is designed to fulfil the energy demand of Modena General Hospital, including electricity, heating and cooling of buildings, while the auxiliary devices are designed to meet the peak of General Hospital heat demand usually occurring in winter season.

Italian law sets the regulatory limits for atmospheric emissions of methane supplied internal combustion four-stroke engines and boilers for specific pollutants, e.g.: $NO_x$, $SO_x$, PM10, CO and $CO_2$. $NO_x$, $SO_x$, PM10 and CO are renowned as critical pollutant species in urban environment, whereas greenhouse gas emission (chiefly $CO_2$) has a worldwide influence (Houghton *et al.*, 2001;

Meunier, 2002), but does not affect significantly local air quality in the surrounding of the power plant. Pollutant emissions mainly vary with plant fuel consumption that depends on the operational.
Finally, the potential benefit on local air quality by switching from the existing plant to the new plant must be evaluated by the comparison of their stack emissions rates. In the present case study, the comparison between the two plants is performed by simulating pollutant dispersion phenomena both in the current and in the future in scenario, by means of Lagrangian models.
Several authors (e.g. Trini Castelli *et al*., 2003; Gariazzo *et. al*., 2007; Ghermandi *et al*., 2012, Božnar *et al.*, 2012) used air quality models to simulate pollutant dispersion of stack emissions from power plants or industrial activities.

## 5.3 The existing and the future power plant

The current heating system of Modena General Hospital consists of three conventional boilers and two steam generators for hot water and steam production respectively (Table 4). All the devices are equipped with a burner fuelled with methane gas.

| Device | Thermal power ($kW_{th}$) | Service |
|---|---|---|
| **Boiler 1** | 5 168 | Hot water production |
| **Boiler 2** | 5 227 | |
| **Boiler 3** | 5 227 | |
| **Steam Generator 1** | 2 558 | Steam production |
| **Steam Generator 2** | 3 830 | |

*Table 4. The existing plant: size and service for each device.*

Boilers are equipped with a centrifugal pump, in order to increase the pressure of heated water prior to enter the piping system for heat distribution within the General Hospital. Generally, only three of the five devices are continuously active to provide the required thermal energy, since the plant was oversized with safety criteria.

The new plant consists of a tri-generation unit and five auxiliary devices, three conventional boilers and two industrial steam generators. Auxiliary devices are supposed to be activated in support of the tri-generation unit when the recovered heat from the tri-generator is not enough to supply the whole energy demand of the General Hospital. The new plant, similarly to the existing plant, is oversized according to safety criteria; even when the energy demand reaches the peak, in winter season, only one boiler and one steam generator are expected to be active.

The tri-generation unit that will be installed is a Jenbacher JMS 620 GS-N.L featured by an electrical power of 3349 kWe, a thermal power of 3098 kWt, with an electric efficiency is 44.2 % and a thermal efficiency of 40.9 %. The unit has an internal combustion four-stroke engine powered by methane gas. Sizes of new plant auxiliary devices are reported in Table 5.

| Device | Thermal power ($kW_{th}$) | Service |
|---|---|---|
| **Boiler 1** | 5 653 | Hot water production |
| **Boiler 2** | 5 653 | |
| **Boiler 3** | 3 027 | |
| **Steam Generator 1** | 2 312 | Steam production |
| **Steam Generator 2** | 2 312 | |

*Table 5. The new plant: size and service for auxiliary devices.*

## 5.4 Comparison between pollutant emissions

The tri-generation unit and the auxiliary devices were designed to replace the previously described old obsolete heating system, due to its low energy efficiency and its high atmospheric impact.
The self-production of electric power by means of tri-generation will reduce the electricity energy demand from IEEN; nevertheless, in order to estimate the benefit on local air quality by shifting from the existing to the new plant, the stack emission rates of the two plant facilities are compared.

### *5.4.1 Electric energy needs*

Currently, the total electric energy needs for the General Hospital, which is entirely supplied by IEEN, is equal to 25 494 MWh/y. According to the annual scheduled stop periods for the ordinary maintenance, the tri-generator unit is supposed to be active for 7 010 total annual hours. Therefore, a part of the required electric energy by the General Hospital, which has been prudently estimated up to 4 013 MWhe/y, is still provided by IEEN.
Table 6 reports the comparison between pollutant emissions due to the electrical energy production from IEEN in the current and in the future scenario. It is worthwhile to remark once more that the avoided emissions of $CO_2$ lead to an air quality benefit on global scale, while the avoided emissions of $NO_x$, $SO_x$, and PM10 lead benefit on air quality in the surroundings of the electric energy production plant, which is very far away from Modena.

| **Pollutant specie** | **Emissions from IEEN (t/y)** | |
|---|---|---|
| | **Tri-generation unit** | **Existing plant** |
| **$NO_x$** | 0.95 | 6.04 |
| **$SO_x$** | 0.91 | 5.81 |
| **PM10** | 0.05 | 0.31 |
| **$CO_2$** | 1693 | 10758 |

*Table 6. Comparison among annual pollutant emission due to electric energy production by Italian Electric Energy Network (IEEN) in the current and future scenario.*

Emission values in Table 6 were estimated from the atmospheric emission inventory for electric energy production plants in Italy, according to the following emission factors proposed by the National Agency for Electric Energy (ENEL, 2010) and equal to: $CO_2$ = 422 ($g/kWh_{eq}$), $NO_x$ = 0.237 ($g/kWh_{eq}$), $SO_x$ = 0.228 ($g/kWh_{eq}$), $PM_{10}$= 0.012 ($g/kWh_{eq}$).

### *5.4.2 Annual mass fluxes of pollutants for the existing and the future plant*

The flow rate of the exhaust gas emission from the existing plant has been estimated from the annual fuel consumption of the year 2010 assuming mass conservation, combustion occurring at stoichiometric conditions and that all devices operate at steady state conditions.

In order to estimate the exhaust flow rate, the following data were provided by courtesy of the current plant manager: annual fuel consumption (methane gas) for the year 2010, air excess for methane combustion (2.9%) and exhaust gas temperature at stack exit (150 °C). The fuel consumption value was split between the three out of five devices that continuously operated during year 2010. Methane consumption along year 2010 shows large daily variation, ranging from 22 143 $Sm^3$/day (peak consumption in winter) to 2 067 $Sm^3$/day (minimum consumption in summer)[1]. Therefore, according to seasonality, a high yearly variation of pollutant emission rate occurs. The $NO_x$, CO, $SO_x$ and $PM_{10}$ concentrations in the exhaust gas emission were set equal to the Italian regulatory limits (D. L. 152/06), i.e. $NO_x$ (as $NO_2$) = 350 mg/$Nm^3$, $SO_x$ = 35 mg/ $Nm^3$, $PM_{10}$ = 5 mg/ $Nm^3$, CO = 100 mg/ $Nm^3$, in the exhaust dry gas flow with 3% oxygen ($O_2$)[2].

Pollutant emissions from tri-generation unit were estimated from exhaust dry gas flow data: dry gas flow of 13 920 $Nm^3$/h with 11.2 % oxygen ($O_2$). Pollutant concentration values in the exhaust dry gas flow, with 5% oxygen ($O_2$), are equal to $NO_x$ (as $NO_2$) = 250 mg/$Nm^3$, CO = 300 mg/ $Nm^3$, $PM_{10}$ = 30 mg/ $Nm^3$, specific emission of $CO_2$ = 510 g/kWhe. Plant manufacturer certifies both gas flow and pollutant concentrations. Pollutant concentration values were scaled to the actual oxygen content in the exhaust gas flow, according to the "nominal" operating conditions of the plant.

Assuming a total amount of 7 010 annual hours of activity for the tri-generation unit, the annual mass fluxes for the two plants were computed and reported in Table 7.

| **Pollutant specie** | **Plant stack emissions (t/y)** | | |
|---|---|---|---|
| | **Future scenario** | | **Actual scenario** |
| | *Tri-generation unit* | *Auxiliary devices* | *Existing plant* |
| **$NO_x$ (as $NO_2$)** | 14.94 | 4.57 | 10.62 |
| **CO** | 17.93 | 1.31 | 3.03 |
| **$SO_x$** | - | 0.46 | 1.06 |
| **PM10** | 1.79 | 0.07 | 0.15 |
| **$CO_2$** | 11 347 | 2 522 | 5 865 |

*Table 7. Comparison among annual pollutant stack emissions from the tri-generation unit and the existing plant.*

[1] Standard Conditions ($Sm^3$): T = 15 °C, P = 101 325 Pa.
[2] Normal Conditions ($Nm^3$): T = 0 °C, P = 101 325 Pa.

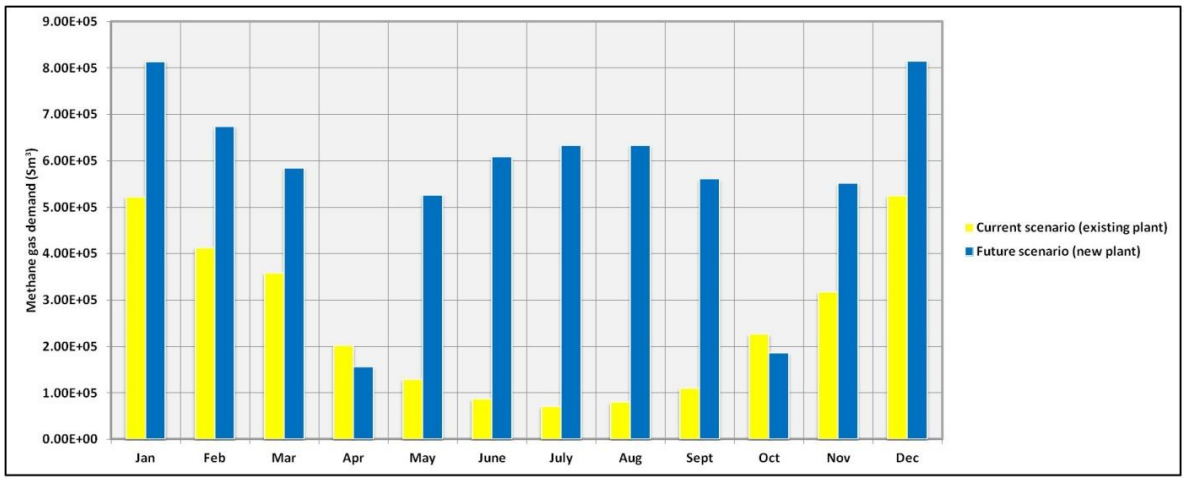


*Figure 27. Monthly pattern of total methane gas demand ($Sm^3$) in the current (existing plant) and in the future (new plant) scenario.*

Stack emission data reported in Table 7 shows that the new plant facilities lead to a higher fuel demand and then to a potentially worse emission scenario on an annual basis than the existing plant, even when pollutant emissions from the two auxiliary devices (boiler and steam generator) of the future plant were not yet taken into account.

However, as showed by Pehnt (2008), commonly occurs that switching from an obsolete power plant to a new tri-generation unit, pollutant emissions are quite modest and the margins of improvement may be small if both fuelled with methane gas.

Nevertheless, the atmospheric impact of pollutant emissions exhibits large seasonality. Figure 27 shows the monthly pattern for the total demand of methane gas ($Sm^3$) in the current (existing plant) and in the future scenario (new plant). In the future scenario both tri-generation unit and auxiliary devices (boiler and steam generator, that will operate, upon request, at a loading rate < 50 %) are taken into account. Figure 28 compares the methane gas demand in every month by heating (boiler), steam generator and tri-generation unit in the new plant configuration.

The increase of methane gas demand by switching from the current to the future scenario, which is clearly visible in Figure 27, is mainly due to the tri-generation unit, as shown in Figure 28.

Due to the seasonal variation of the energy demand of the General Hospital, considerable differences are noticeable from winter to summer season, and the peak of fuel consumption, which is expected in winter, leads to the peak pollutant emission in January and February. Moreover, winter represents the most critical season for air quality, featured by build-up and ageing of pollutant emission in the Po Valley atmosphere (Ferrero *et al*., 2011).

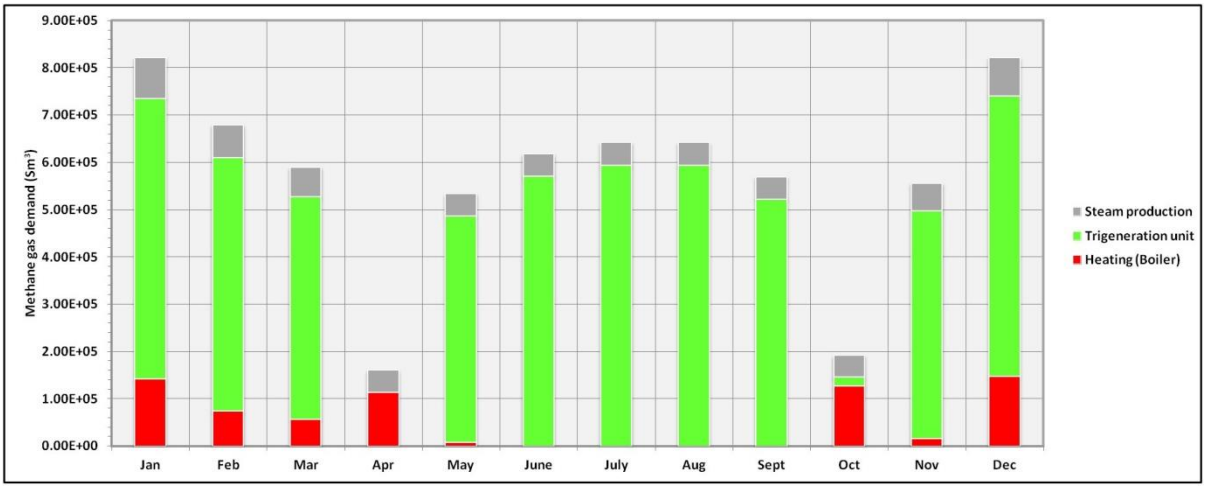


*Figure 28. Single contribution to the monthly methane gas demand* ($Sm^3$) *by heating (boiler), steam generator and tri-generation unit in the new plant configuration.*

Thus, a correct impact assessment must take into account in which way the seasonal variation of both pollutant emission rates and atmospheric mixing conditions affects the dispersion patterns from stack emissions. Simulations of pollutant dispersion scenarios, both for the existing and the new power plant, were performed for winter and summer season, involving 2010 as a test year for meteorology and fuel consumption data; winter was taken as January 1$^{st}$ to March 20$^{th}$ 2010, Summer as June 1$^{st}$ to August 31$^{st}$. However, aiming to investigate the worst-case scenario for air quality impact, the simulations mainly focused on winter season. The simulated pollutant specie was $NO_x$, being $NO_x$ the most critical pollutant specie for methane-fuelled plants.

Furthermore, a recent study on $NO_x$ atmospheric measurements in the urban area of Modena showed $NO_x$ as one of the most critical pollutant species, since hourly average concentration values are frequently close or higher than regulatory limit, especially in winter season and in case of intense vehicular traffic (Bigi *et al*., 2012).

# Chapter 6

# *Simulation results*

## 6.1 Introduction

The atmospheric dispersion of pollutant emissions was simulated both at local and at micro-scale, by means of SPRAY and Micro-SPRAY models respectively. Simulation time step has been set equal to 1 hour, due to the hourly meteorological input data. The simulated plumes are from methane-fuelled power plants; therefore, since $NO_x$ is the most critical pollutant specie for methane-fuelled plants, as previously mentioned, the study is centred on $NO_x$ emissions.

The simulations were performed during year 2010 and mainly focused on the winter season, by taking winter as January 1$^{st}$ to March 20$^{th}$ as a test period. The meteorological dataset consists of both simulated and measured data for wind speed, wind direction, temperature and turbulence scale variables $L$, $H_{mix}$, $w^*$, $u^*$ for PBL. Meteorological measurements were provided by Osservatorio Geofisico of Modena and Reggio Emilia University (Modena, Italy) and by ground station of Local Environmental Protection Agency (ARPA). Meteorological simulated data comprise mesoscale vertical wind profiles and two-dimensional fields of PBL turbulence parameters $L$, $H_{mix}$, $w^*$, $u^*$. The simulation was performed by ARPA by means of the mesoscale meteorological processor CALMET (Deserti *et al.*, 2001); input data for CALMET model consist of ground meteorological measurements and radio sounding profiles, which were acquired on a large simulation domain spanned over the whole Northern Italy.

Topographical and land-use data were outlined from remote sensing images. Ground elevation data were provided by Shuttle Radar Topography Mission through United States Geological Service (USGS); land-use surface data derive from raster images from European CORINE Land Cover 2000 dataset (EEA, 2015a).

In the present chapter, the simulation results are discussed through pollutant concentration maps and vertical concentration profiles. Simulated concentration values are compared with measured data for $NO_x$ concentration, in order to assess the ability of SPRAY and MSS in providing reliable simulations of atmospheric dispersion. Air quality measurements are provided by Local Environmental Protection Agency (ARPA), through fixed-site monitoring stations in Modena.

## 6.2 Local scale simulations

The present section provides a description of model setup, pollutant sources and simulation results for the local scale simulations. Further details can be found in Ghermandi *et al*. (2015).

### *6.2.1 Model setup*

Airborne pollutant dispersion patterns are simulated via Lagrangian Particle Dispersion Model SPRAY (Chapter 2); input meteorology and turbulence fields are provided by mass-consistent diagnostic model MINERVE and turbulence processor SURFPRO respectively (Chapter 3); such simulation models, as well as the Emission Manager tool for pollutant sources processing, are included in the ARIA INDUSTRY software package, by Arianet Ltd.

The local scale study is focused on the comparison of two different emission scenarios, which involve an existing obsolete power plant (current scenario) that will be replaced by a new power plant (future scenario), in order to fulfil the energy needs of Modena General Hospital.

The existing plant consists of five devices, three conventional boilers and two steam generators. Because of the plant was sized with security criteria, only three of the five devices operate continuously; hence, only three stack sources were taken into account in the simulation.

Table 8 reports features of stack geometry and emitted exhaust gas flow for the existing plant; the emitted gas temperature refers to the nominal operating conditions, i.e. 100 % loading rate.

| Device | Thermal power ($kW_{th}$) | Emitted gas temperature (°C) | Stack height (m) | Stack diameter (m) | Service |
|---|---|---|---|---|---|
| **Boiler 1** | 5 168 | 180 | 11.30 | 0.75 | Hot water production |
| **Boiler 2** | 5 227 | 180 | 11.30 | 0.75 | |
| **Boiler 3** | 5 227 | 180 | 11.30 | 0.75 | |
| **Steam Generator 1** | 2 558 | 160 | 11.30 | 0.70 | Steam production |
| **Steam Generator 2** | 3 830 | 160 | 11.30 | 0.70 | |

*Table 8. The existing plant features at nominal conditions (100 % loading rate).*

Values in Table 8 were assigned to SPRAY model as input simulation data for the three operating devices (Boiler 1, Boiler 2 and Steam Generator 2); the flow rate of the exhaust gas was computed from the fuel consumption for year 2010, since no emission monitoring data were available.

In order to represent the worst-case scenario, the current plant is assumed to operate continuously at the maximum daily fuel consumption for year 2010 (i.e. 22,143 $Sm^3$/day, occurred in winter 2010) and corresponding to the highest emission flow. This fuel consumption results in a cumulative dry exhaust flow rate from all three operating devices of the current plant stacks of ≈ 10,000 $Nm^3$/h, with average exit velocity of gas emissions of 3.2 m/s.

The new power plant includes a tri-generation unit and the auxiliary devices: three conventional boilers and two steam generators will be installed. The tri-generation unit operates almost steadily, whereas auxiliary devices are designed to operate in support of the tri-generation unit, i.e. during periods of higher energy demand and during the tri-generation unit maintenance stops. Similarly to the existing plant, the new plant was designed according to safety criteria and only one boiler and one steam generator operate continuously; the remaining devices are generally inactive.

Hence, the simulation of pollutant dispersion in the future scenario involves only three of the five auxiliary devices: the tri-generation unit, Boiler 1 and Steam Generator 1 (Table 9 above). Features and operating conditions of both plant facilities were discussed in Chapter 5.

Table 9 reports the features of the stack geometry and the emitted exhaust gas flow for each device of the new plant at nominal conditions (100 % loading rate).

| Device | Thermal power ($kW_{th}$) | Emitted dry gas flow ($Nm^3$/h) | $O_2$ (%) | Emitted gas temperature (°C) | Stack height (m) | Stack diameter (m) | Service |
|---|---|---|---|---|---|---|---|
| **Boiler 1** | 5 653 | 5 221 | 3 | 170 | 10 | 0.70 | Hot water production |
| **Boiler 2** | 5 653 | 5 221 | 3 | 170 | 10 | 0.70 | |
| **Boiler 3** | 3 027 | 2 811 | 3 | 170 | 10 | 0.70 | |
| **Steam Generator 1** | 2 312 | 1 937 | 3 | 215 | 10 | 0.50 | Steam production |
| **Steam Generator 2** | 2 312 | 1 937 | 3 | 215 | 10 | 0.50 | |
| **Tri-generation unit** | 3 098 | 13 920 | 11.2 | 125 | 15 | 0.70 | Heat recovery |

*Table 9. The new plant features at nominal conditions (100 % loading rate).*

In the new plant configuration, the tri-generation unit is expected to operate almost constantly at 100 % loading rate for all the hours of the day; thus, the pollutant flow rate from the tri-generation unit stack was assumed as constant for the whole simulation period.

On the contrary, the two auxiliary devices operate several hours a day at loading rate < 50 %, with a strong daily variation on fuel consumption. Hence, for each month of the simulation period, average values of the emitted pollutant flow were computed in a ‘‘typical’’ day of operation; besides, the so-

computed values were modulated on hourly basis, according to the daily variation on fuel consumption, which depends on the hourly energy needs of the General Hospital.

The simulation period spans over the whole winter season, from January 1st to March 20th, and involves year 2010 as a test period; as shown in Chapter 5, most critical conditions for pollutant accumulation in the atmospheric environment occur in winter.

The simulation domain is centred at the emission source, i.e., the location of the current and future power plant, close to the General Hospital of Modena. The spatial domain for wind field and turbulence parameters estimation (MINERVE and SURFPRO codes) covers an area of 40 x 40 $km^2$, divided into a horizontal grid of 500 m square cells and into a vertical grid of 30 layers from the ground to 1800 m. For the computation of pollutant concentration fields, the domain is limited to an area of 20 x 20 $km^2$, centred at the emission source and divided into a grid of 250 m square cells. Details about spatial implementation of simulation domain are reported in Chapter 2, for SPRAY model, and Chapter 3, for MINERVE and SURFPRO models.

The emission sources are simulated as continuous point sources. For boilers and steam generators, both in the current and in the future emission scenario, the stack emission rates for $NO_x$ were evaluated assuming the pollutant concentrations always equal to the regulatory limits. For methane-fuelled power plants, with a nominal power lower than 50 MW, the Italian law (D. L. 152/06) sets a maximum value for $NO_x$ concentration in the exhaust dry gas flow equal to 350 $mg/Nm^3$, with 3 % oxygen ($O_2$) and assuming $NO_x$ as $NO_2$. For the tri-generation unit, assuming $NO_x$ as $NO_2$, the plant manufacturer certifies a $NO_x$ concentration value in the exhaust gas flow equal to 250 $mg/Nm^3$, with 3 % oxygen ($O_2$); this is the value assumed as input emission data for the simulations

Table 10 summarizes the regulatory limits for $NO_x$ $SO_x$, CO and Particulate Matter concentrations set by D. L. 152/06, both for thermal power plant with a nominal power lower than 50 MW and for four-stroke internal combustion engines fuelled with methane-gas.

| | **Particulate Matter ($mg/Nm^3$)** | **$NO_x$ ($mg/Nm^3$)** | **$SO_x$ ($mg/Nm^3$)** | **CO ($mg/Nm^3$)** |
|---|---|---|---|---|
| **Thermal plants** | 5 | 350 | 35 | - |
| **Four-stroke engines** | 130 | 500 | - | 650 |

*Table 10. Regulatory limits for pollutant concentrations in the exhaust-gas flow set by* D. L. 152/06.

### *6.2.2 Pollutant concentration maps: the whole plant*

Figure 29 shows the ground concentration maps[3] for the emitted $NO_x$, i.e. in the first atmospheric layer for concentration computing, 10 m deep, for the current (left) and for the future scenario (right). In Figure 29 the SPRAY model hourly output concentrations were averaged over the whole simulation period, namely the 2010 winter season, from January 1st to March 20th 2010.
Both plant stacks are placed in the centre point of the domain.

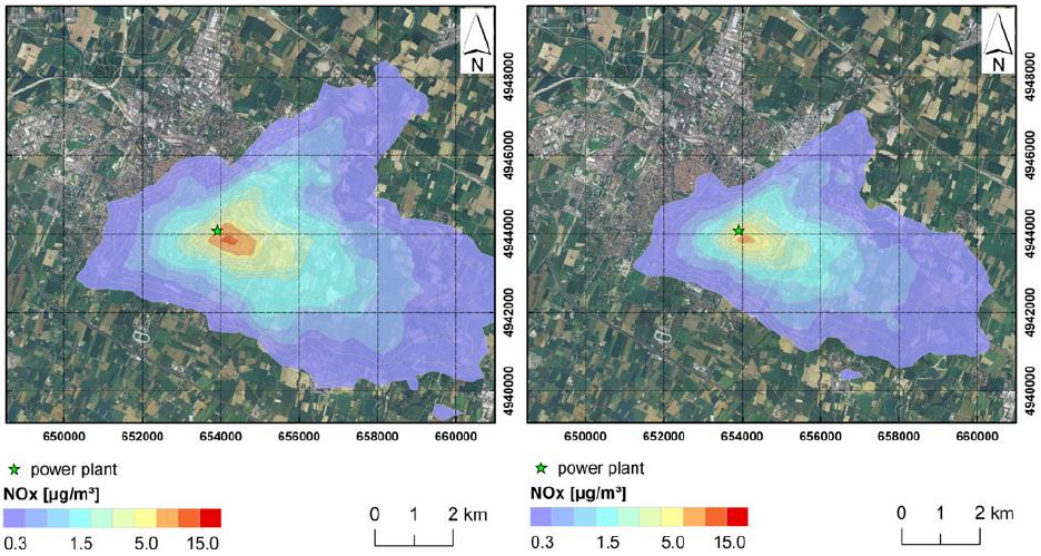


*Figure 29. Average hourly $NO_x$ ground concentration plumes for the current (left) and for the future (right) scenario. The star indicates the location of plant stacks.*

The simulated plumes, both in the current and the future scenario, are stretched along the main wind direction (approximately from North–West to South–East), although the surface representing the area with minimum ground-level concentration is larger in the current than in the future scenario.

| | **Seasonal average ($\mu g/m^3$)** | **Hourly average ($\mu g/m^3$)** | **Regulation hourly limit ($\mu g/m^3$)** |
|---|---|---|---|
| **Current scenario** | 15.0 | 69.0 | 200 |
| **Future scenario** | 7.0 | 21.0 | |

*Table 11. Comparison between seasonal average of maximum simulated values, hourly average values and air quality limit for $NO_x$ concentrations both in the current and in the future scenario.*

[3] The color scales, for all the concentration maps reported in the following, refer to $NO_x$ simulated concentrations; measurement unit is always $\mu g/m^3$.

In Table 11, the average of maximum simulated values for winter and hourly averaged concentrations, for both the current and the future scenario, are compared with the hourly limit for $NO_x$ concentration, according to the European regulation for atmospheric air quality (E.U., 2008).
The average value of concentration maxima for the current plant reaches the 34.5 % of the regulatory limit (200 μg/m$^3$), while for the new plant represents about the 10 % of the regulatory limit. These results indicate that, in winter, atmospheric $NO_x$ concentration in Modena may be significantly affected by the current plant emissions, eventually leading to concentration values closer to the air quality limits in case of weather conditions favourable to pollutant accumulation.
Nonetheless, by switching from the existing to the new power plant, the atmospheric impact of pollutant emissions is reduced. Even in case of a more conservative simulation for the current plant, i.e. by assuming the average daily fuel consumption for winter 2010 instead of its maximum, the simulated $NO_x$ concentrations would result ≈ 27 % lower, but still higher than for the new plant.
The impact of the current plant to the near-ground atmosphere is the largest, also because the exit velocity of gas emissions from the tri-generator is much higher than that from conventional boilers, as shown in Paragraph 6.2.4.

### *6.2.3 Pollutant concentration maps: individual contributions of new plant devices*

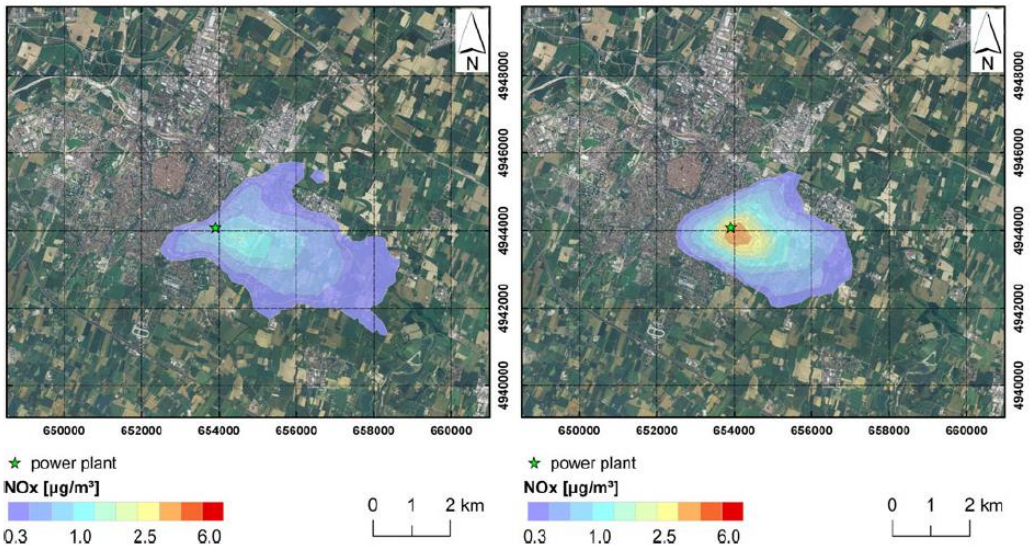


*Figure 30. Average hourly $NO_x$ ground concentration plumes from the individual contributions of the new plant (future scenario); the tri-generation unit (left) and the auxiliary devices (right).*

In Figure 30, the pollutant plume from the new power plant (Figure 29) and for the tri-generation unit is split in two individual contributions: the tri-generator (left) and the active auxiliary devices (right), i.e. Boiler 1 and Steam Generator 2. Ground concentration maps still involve the seasonal (winter) average of hourly-simulated $NO_x$ concentrations, in the first atmospheric layer, 10 m deep.
In Table 12, the maximum simulated values for winter and hourly averaged concentrations from the tri-generation unit and from the auxiliary devices are compared with the hourly limit for $NO_x$ concentration, according to the European regulation for atmospheric air quality (E.U., 2008).

| | **Seasonal average ($\mu g/m^3$)** | **Hourly average ($\mu g/m^3$)** | **Regulation hourly limit ($\mu g/m^3$)** |
|---|---|---|---|
| **Tri-generation unit** | 1.4 | 9.3 | 200 |
| **Auxiliary devices** | 5.6 | 16.1 | |

*Table 12. Comparison between maximum simulated values and air quality limit for $NO_x$ concentrations both in the current and in the future scenario.*

The peak of average $NO_x$ concentrations, from the tri-generator and from the auxiliary devices, occurs at about 400 m and about 220 m from the source respectively. The maximum hourly average concentration values in the maps of the individual sources may fall in different points respect to the maximum for the total plant (Figure 29 right), because each source has its own concentration field.
The $NO_x$ emission rate from tri-generation unit is considerably higher than from the boiler and the steam generator: the ratio between the tri-generator and either the boiler or the steam generator $NO_x$ emission rates ranges between 3.2 and 10 over the whole simulation period, depending on the occurring operational conditions of each unit. In addition, the emissions from conventional boilers have higher temperature than tri-generator exhausts, which are cooled by the heat recovery system (Table 9). Nevertheless, as shown in Figure 30, the impact by conventional devices to near-ground atmosphere is the largest, because the exit velocity of gas emissions from the tri-generator is ten times higher than that from boiler and steam generator. The average exit velocities used in the simulation are 15.10 and 1.56 m/s for the tri-generator and the conventional boilers, respectively. In addition, the stack height of boiler and steam generator is lower than the trigenerator one (Table 9).
Besides, the dynamic plume rise is calculated by SPRAY as reported in Anfossi *et al*. (1993), with a conservative approach, and possible rise enhancement effects due to merged plumes respect to single emissions (Anfossi *et al*., 1978; Anfossi 1985) are not considered.

### *6.2.4 New plant: vertical concentration profiles*

In order to investigate more in detail the combined effect between the exit velocity of the exhausts and the stack heights, the vertical $NO_x$ concentration profiles in the atmosphere are compared.
Such profiles result from the concentration values in the cells of an air column starting at the ground and passing through all the atmospheric layers in which SPRAY structures the 3D domain. The vertical $NO_x$ profiles, obtained for the total emissions from the new plant (tri-generator, boiler and steam generator) and from the individual emission plumes of the tri-generator, the boiler and the steam generator, are shown in Figure 31 (left). These vertical profiles are taken at the peak for $NO_x$ hourly average ground concentration by the total emissions of the new plant (P1, Figure 31, right; 654 106 E, 4 943,881 N, UTM32-WGS84), value occurring 270 m South-East of it.

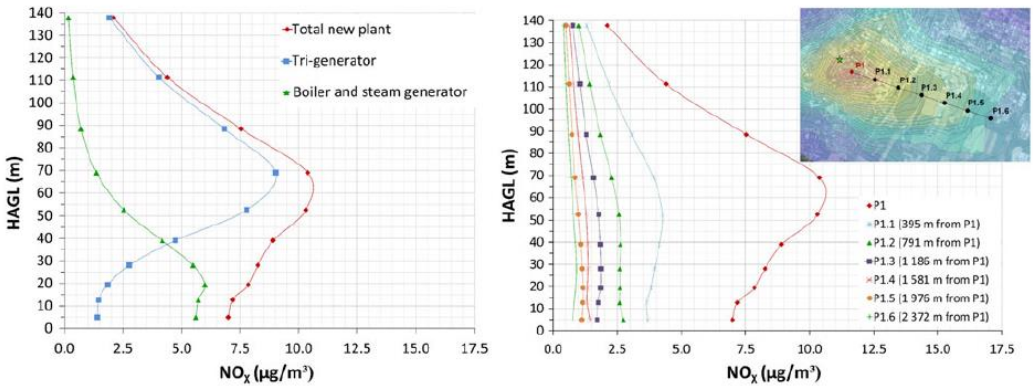


*Figure 31. Vertical profiles of average hourly winter $NO_x$ concentrations.*
Left: *total emissions of the new plant and individual source contributions at point P1.*
Right: *total emissions of the new plant along the main wind direction (points from P1 to P1.6).*

The vertical $NO_x$ profiles show clearly that the boiler and steam generator emissions are the main contributors to the high concentration values at ground level, while their impact decreases rapidly with height. On the contrary, the tri-generation unit emissions cause a significant $NO_x$ concentration peak at almost 70 m above the ground, where total $NO_x$ concentration is about 11 $\mu g/m^3$ and higher than at ground level.
In Figure 31 (right), the trend of the vertical $NO_x$ concentration profile (total new plant emissions) has been investigated along the main wind direction (approximately from North-West to South-East) at the position P1, i.e., at the peak for ground concentration. The concentration profiles were truncated at 140 m above ground level. The profiles result gradually smoothed with the increasing distance from the source: the concentration peak at about 70 m altitude is significantly smoothed at about 2 km from P1. This behaviour is particularly evident in low-wind conditions, when the

vertical dispersion of pollutants, due to the atmospheric turbulence, is widely prevailing over transport along wind direction. To profile smoothing, at increasing distance from sources, might also contribute the attainment of the good mixing that can happen at different distance depending on the atmospheric conditions (Slawson and Csanady 1971).
The trends of vertical concentration profile along other directions are quite similar one each other and do not differ strongly from the trend along the main wind direction reported in Figure 31 (right), because of the moderate wind speed intensities and the very high frequency of low wind events occurring in winter 2010.

### *6.2.5 Comparison with air quality limits and experimental measurements*

Local Environmental Protection Agency (ARPA) provides air quality measurements of atmospheric pollution in urban environment. For the present study, atmospheric $NO_2$ measured concentrations were collected at an urban measuring site in Modena, at about 3 km from the plant location; because of the vicinity to a heavy trafficked road, the contribution of vehicular traffic emissions is predominant. Averaged seasonal values for the year 2010, which are presented in Table 13, can be compared with the simulation outputs for average winter $NO_x$ (as $NO_2$) concentrations (Table 10).

| **Pollutant** | **Winter (µg/m$^3$)** | **Spring (µg/m$^3$)** | **Summer (µg/m$^3$)** | **Autumn (µg/m$^3$)** |
|---|---|---|---|---|
| **$NO_2$** | 80.51 | 50.84 | 42.54 | 57.48 |

*Table 13. $NO_2$ seasonal average atmospheric concentrations in an urban site in Modena (ARPA).*

In seasons other than winter, the fuel consumption from the current plant is lower, leading to lower emissions. The lowest annual atmospheric impact of stack emissions is observable in summer, due to the decrease of thermal energy needs by the General Hospital and since annual maximum values for $H_{mix}$ (Paragraph 5.1) occur and convective atmospheric mixing is enhanced. The average daily fuel consumption, for summer 2010, is ≈ 17.4 % of 2010 average winter value, leading to an analogous reduction in the $NO_x$ emission rate. A comparison of simulation results for each season shows the decreasing of $NO_x$ ground concentrations from winter to summer down to 1 µg/m$^3$ or lower. Given the quite steady tri-generation unit activity, also its emission flow is expected to be quite steady throughout the year. On the contrary, the planned auxiliary device activity is variable throughout the year, with inactivity (the boiler) or very low loading rate activity (the steam generator) in summer, leading to a minimum impact on air quality in summer also for the new plant.

## 6.3 Micro-scale simulations

### *6.3.1 From local scale to micro-scale simulation*

Local scale study showed a reduction of the $NO_x$ emissions impact by switching from the existing plant to the future power plant. Besides, in the future scenario, the atmospheric impact close to the ground level is more affected by the individual contributions of the auxiliary devices (Boiler 1 and Steam Generator 1) than by the tri-generation unit.

Highest $NO_x$ concentration levels in Figure 29 and 30 involve a densely populated urban area, very close to the General Hospital, highly already exposed to emissions from nearby high vehicular traffic and household heating systems. Due to the remarkable presence of buildings in such area, the atmospheric dispersion of pollutant stack emissions are more influenced by plume interactions with urban canopy than by local-scale meteorology; this is particularly noticeable since the stack heights of the new plant devices (Table 9) are similar to the average height of the surrounding buildings.

Hence, the application of a high-resolution micro-scale model is useful for simulating dispersion patterns among urban obstacles, in order to achieve more detailed concentration results in the study area close to the power plant stacks and to the General Hospital.

The simulations were performed by means of micro-scale Micro-SWIFT-SPRAY modelling system (Chapter 4), by taking into account urban canopy.

Main aim of the study is to investigate how building geometry, distance and location can affect airborne pollutant dispersion patterns in different meteorological conditions. Moreover, since the new plant is not yet operational, in order to evaluate the extent of the atmospheric impact of the future emission scenario on the local air quality, the $NO_x$ simulated concentrations and the regulatory limits for air quality were compared.

The comparison of simulation results with measured concentration data for $NO_x$ highlights the ability of MSS in providing reliable simulations of atmospheric dispersion. The following section summarizes the model setup and the findings for micro-scale simulations; further details can be found in Ghermandi *et al*. (2014).

### *6.3.2 Model setup*

The simulations were performed under two different atmospheric scenarios: a low wind (i.e. wind speed < 2 m/s) event and a case of wind speed significantly above the average winter value. The meteorological dataset involves the 2010 winter season, i.e. the most critical season in the Po Valley (Ferrero *et al*., 2011), because of the high frequency of low wind and thermal inversion events. Two days, January 14$^{th}$ and February 6$^{th}$, were selected in order to obtain simulations under widely differing meteorological conditions. Figure 32 shows the daily patterns for hourly wind speed and for mixed layer height ($H_{mix}$) in the two test days. In 2010, average winter values of wind speed and mixing height in Modena resulted of 1.7 m/s and 310 m, respectively.

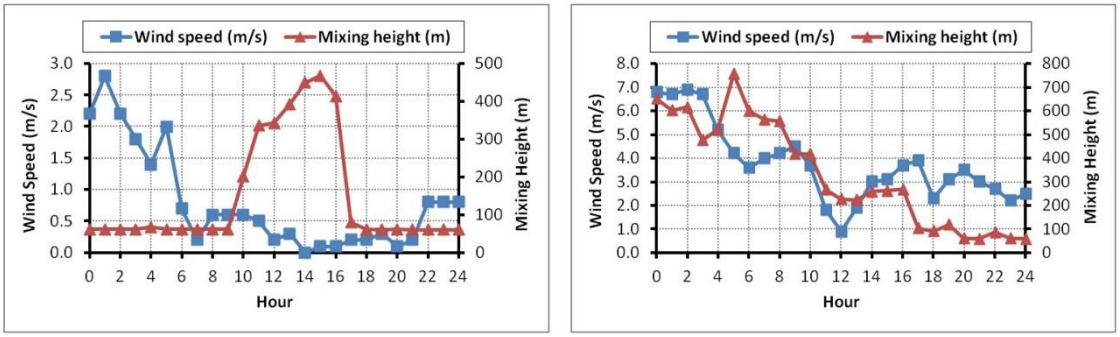


*Figure 32. Meteorological dataset: hourly wind speeds and mixed layer heights for January 14$^{th}$ (left) and February 6$^{th}$ (right) 2010.*

January 14$^{th}$ is characterized by low winds (prevalent condition at the studied site) and atmospheric stability. The Mixed Height ($H_{mix}$) pattern (Figure 32, left) shows that stable conditions occur early in the morning and at nightfall, while thermal convection prevails only in the middle of the day. Similar atmospheric conditions, in which stability occurs for most of the day, are unfavourable to pollutant dispersion and are fairly frequent during the winter in the Po Valley (Bigi *et al*., 2012).
On the contrary, on February 6$^{th}$, wind speed values are higher than the average measured value for the whole 2010 winter season, and the irregular trend of the mixing height is due to clouds and rainy periods (daily precipitation is 8 mm). This day has been chosen in order to evaluate the dispersion patterns in conditions of moderate wind, which infrequently occur in the studied area.
Input meteorology for micro-scale simulations consists of both simulated and measured meteorological data. Osservatorio Geofisico of Modena and Reggio Emilia University (Modena, Italy) collected measured data, for wind speed, wind direction and temperature, at a meteorological station located near pollutant sources. Simulated dataset, i.e. a vertical wind profile and time series

for $L$, $H_{mix}$, $w^*$, $u^*$ values, were provided by ARPA by means of a CALMET model simulation (Deserti *et al.*, 2001), by using ground meteorological measurements and radio sounding profiles as input data. Both the vertical wind profile and the time series of turbulence parameters were extracted at two points in correspondence of the study area.

The study is focused on the $NO_x$ stack emissions from the new power plant. Features and operating condition are the same as shown in Paragraph 6.2.1 and in Chapter 5. The emitted exhaust gas flows calculation was based on the hourly average fuel consumption planned for the monthly "typical" day in January and February. For the auxiliary devices (Boiler 1 and Steam Generator 1), the $NO_x$ concentration in the exhaust gas flow was set equal to the regulatory limit (D. L. 152/06), i.e. 350 $mg/Nm^3$, with 3 % oxygen ($O_2$) and assuming $NO_x$ as $NO_2$. For the tri-generation unit, $NO_x$ concentration in the exhaust gas flow was assumed equal to the certified value by the plant manufacturer, i.e. 250 $mg/Nm^3$, with 3 % oxygen ($O_2$) and assuming $NO_x$ as $NO_2$.

Since the simulation spans over a daily period (24 hours), the hourly variation on fuel consumption and on the pollutant flow rate, deeply affects the concentration model outputs, especially on a micro-scale domain. Therefore, a specific hourly modulation of emission patterns for the boilers and for the steam generator was considered. For the tri-generation unit, which operates at steady-state conditions, the emission pattern was assumed to be constant throughout the day.

Table 14 reports daily average for exhaust gas temperature and velocity at the exit of the three device stacks during the two test days. Stack features and thermal power of Boiler 1 and Steam Generator 1 are reported in Table 9 (Paragraph 6.2.1). The emitted gas flow temperatures are different from values in Table 9 (nominal conditions, 100 % loading rate) since, both in the in the monthly typical day of January and February, the auxiliary devices operate at loading rate < 50 %.

| **Device** | **Exhaust Gas Conditions – Jan. 14th** | | **Exhaust Gas Conditions – Feb. 6th** | |
|---|---|---|---|---|
| | **Temperature (°C)** | **Velocity (m/s)** | **Temperature (°C)** | **Velocity (m/s)** |
| **Boiler 1** | 93 | 2.3 | 76 | 1.3 |
| **Steam Generator 1** | 195 | 2.5 | 190 | 2.3 |
| **Tri-generation unit** | 125 | 16.1 | 125 | 16.1 |

*Table 14. Exhaust gas temperature and velocity (average daily values) at the exit of the three device stacks on January 14th and February 6th 2010.*

The simulation was performed over a 500 m x 500 m horizontal domain, centred at plant position, and divided into a regular grid of cells with size of 2 m x 2 m. This domain represents the urban area surrounding the General Hospital, where the highest atmospheric impact from the future power plant is expected. The vertical domain is divided into a grid of 20 layers, with variable thickness

from the ground to 200 m (domain top): the first vertical layer is 2 m thick. The MSS simulation time step for the output concentration fields has been set to one hour, consistently with the acquisition time step of meteorological input data.

### *6.3.3 Pollutant concentration maps*

Figure 33 shows the maps of daily average $NO_x$ concentration (i.e. the average of the 24 hourly runs of the MSS simulation) in the first atmospheric layer (2 m above ground level), for the two test days; wind roses were drawn on the basis of the daily dataset (24 hourly average values for wind speed and wind direction).

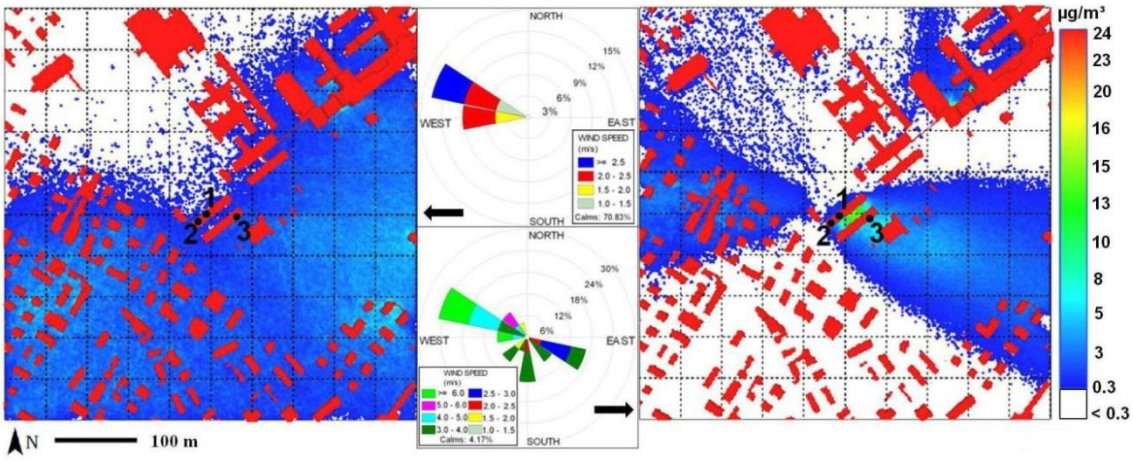


*Figure 33. $NO_x$ daily average concentration maps: concentration values were computed on January 14$^{th}$ (left) and February 6$^{th}$ (right) 2010, in the first atmospheric layer (2 m from the ground level), from all plant sources. The wind roses for the two days are also reported.*

Because of low wind conditions occurring on January 14$^{th}$, the plumes are mainly driven by dispersion and spread at ground with no preferential direction. On the contrary, on February 6$^{th}$, the prevailing wind direction is clearly visible, since moderate wind conditions occur. It would be expected the pollutant accumulation to be higher in the 14$^{th}$ January scenario, when in fact the maximum hourly simulated $NO_x$ concentration value (80.5 µg/m$^3$) results and is reached at 23:00. Nevertheless, the average daily concentration maximum is higher during the February case than in January (23 µg/m$^3$ and 9 µg/m$^3$ respectively).

### *6.3.4 Micro-scale stagnation effects*

Pollutant stagnation phenomena clearly occur on February 6th, due to the building shielding effect, and to the building location with respect to the wind direction. Therefore, $NO_x$ exhibits a local increase of concentration between two parallel buildings, which form an urban canyon very close to the power plant. The pattern of daily average $NO_x$ concentrations, within the urban canyon, was estimated by interpolation of the simulation outputs at 19 points along a longitudinal cross-section of the canyon (Figure 34, left); the concentration gradient between the cavity and the open field is quite evident (Figure 34, right). The canyon effect is enhanced since wind direction is near perpendicular to the canyon axis.

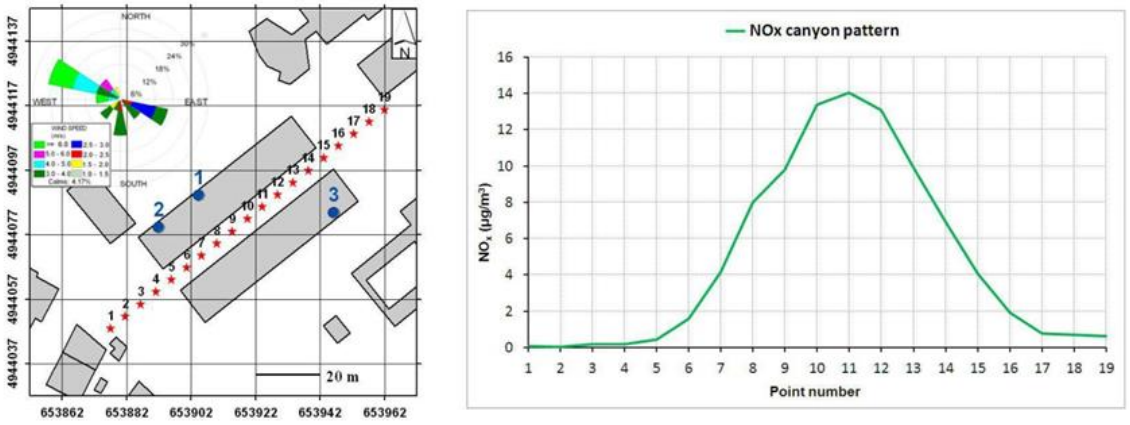


*Figure 34. Focus on the urban canyon: position of the interpolation points on the map and wind rose for February 6th 2010 (left); $NO_x$ daily average concentration pattern on February 6th 2010 within the urban canyon (right).*

According to Oke (1987) and Vardoulakis *et al*. (2003), different air-flow conditions within urban canyons can be classified by means of the *building aspect ratio* $H_{can}/W_{can}$ (see also Paragraph 4.2.4), where $H_{can}$ is the canyon height and $W_{can}$ is the street width; in this case $H_{can} = 8$ m and $W_{can} = 7$ m, so that $H_{can}/W_{can} \approx 1$. Following this classification, in which also wind direction respect to the canyon axis is taken into account, this is a condition of *skimming flow canyon*, where the formation of a single eddy occurs and, thus, turbulent recirculation prevents pollutants removal.
Simulations performed separately for the emission sources, auxiliary devices and tri-generator unit (Ghermandi *et al*., 2013), show that the concentration increase in the canyon is caused mainly by the auxiliary device, since the vertical dispersion is prevented by the wind forcing. The tri-generator emissions appear almost unaffected by building because of their plume rise due to the higher tri-generator stack height and the gas exit conditions (Ghermandi *et al.*, 2015).

Notwithstanding the plant now is not yet operational, the impact of its stack emissions to the near-ground atmosphere may be preliminarily assessed by the comparison between the $NO_x$ simulated concentration and the regulatory limits for air quality. Given that regulatory limits for air quality are set by the European Directive 2008/50/EC (EU, 2008) for $NO_2$ (maximum hourly concentration 200 $\mu g/m^3$) instead of $NO_x$, due to the higher toxicity of the former, and that the simulated emissions are $NO_x$ (as $NO_2$), this comparison leads to a precautionary approach, since $NO_x$ includes both $NO_2$ and NO. Furthermore, the previously mentioned maximum value of hourly-simulated concentration (80.5 $\mu g/m^3$) is much lower than the regulatory limit.

### *6.3.5 Comparison with $NO_x$ measured atmospheric concentrations*

The MSS performances in simulating pollutant dispersion patterns may be investigated from the comparison between the simulation outputs and the $NO_x$ atmospheric concentration measurements, provided by the local Environmental Agency (ARPA) with fixed-site monitoring stations in Modena. Given that the MSS outputs represent the expected contribution to air quality only of the new power plant emissions and no other $NO_x$ emitting source is included in the simulation, this comparison has the aim to evaluate the model reliability in simulating the effect due to the atmospheric dynamics and the $H_{mix}$ daily evolution on the ambient $NO_x$ concentration field.

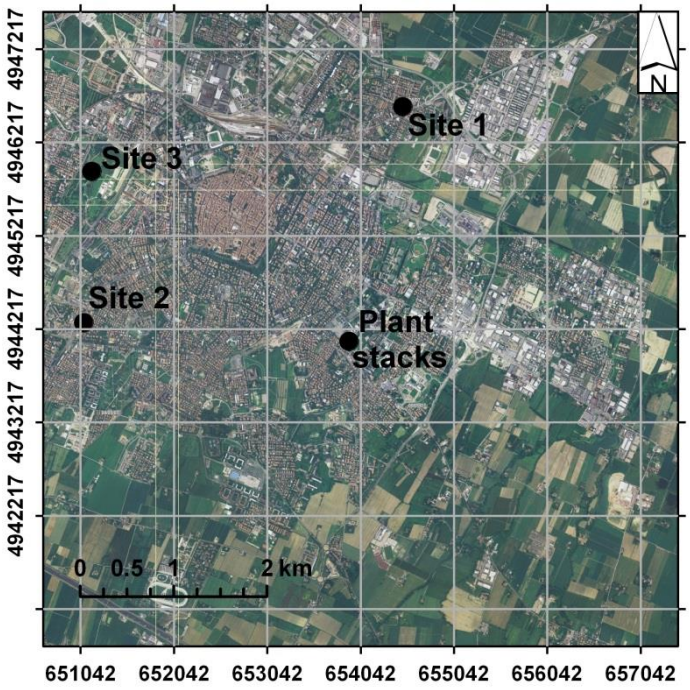


*Figure 35. Geographical map with power plant stack and fixed site monitoring station position.*

Therefore, as shown later (see Figure 36), the simulated concentrations represent only a small fraction of the measured atmospheric $NO_x$, which instead results from the contribution of several urban sources, as vehicular traffic and domestic heating.

The $NO_x$ concentration measurements were compared with the MSS maximum hourly concentrations, i.e. the spatial maximum value from every average hourly concentration map**.** In this comparison, the spatial maximum instead of the spatial average of simulated concentrations was preferred, because the latter is affected by the large number of cells having very low or zero concentration over the whole simulation period (Figure 33). This would lead to an impairment of the temporal comparability between the time series of spatial averages and the time series of measurements at the monitoring stations.

The comparison was carried out only for January 14$^{th}$, 2010, when low wind conditions occurred. The atmospheric $NO_x$ concentrations used in the comparison were measured by local ARPA at a hourly time resolution, at three different fixed-site monitoring stations (Figure 35): two of them (1 and 2) are representative for urban traffic conditions while the third (3) is an urban background site located in the largest city park. These $NO_x$ concentration measurements were compared with the MSS maximum hourly-simulated concentrations in the lowest atmospheric layer (2 m above ground level). Maximum hourly patterns from MSS simulation have been outlined for the overall contribution of the plant and separately for each source, i.e. for the auxiliary devices (Boiler 1 and Steam Generator 1) and for the tri–generation unit.

Figures 36 (left) and 36 (right) show the hourly patterns of measured and maximum simulated $NO_x$ concentrations on January 14$^{th}$. The measured concentration peak during the hours of heavy traffic is quite evident for sites 1 and 2.

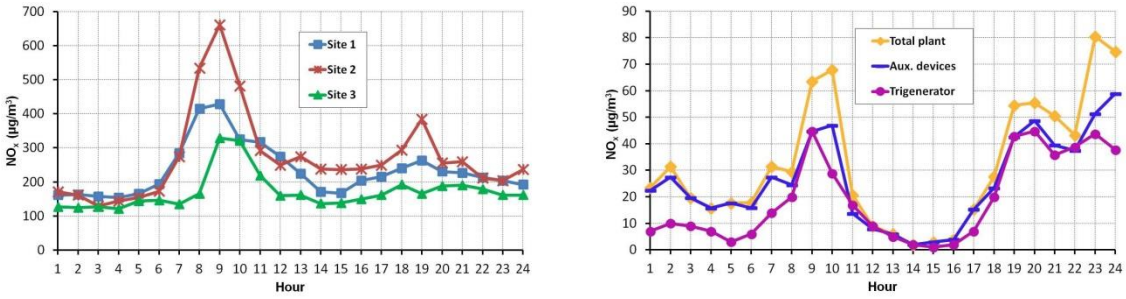


*Figure 36. $NO_x$ hourly concentration patterns on January 14$^{th}$ 2010 outlined from the three measuring sites (left), and from the simulated data (right).*

The comparison was quantitatively evaluated by the Pearson's linear correlation coefficient *r*, between hourly measured data at each site and hourly maximum concentrations for each source

contribution. The correlation has been studied over two time slots: from 01:00 to 24:00 and from 01:00 to 18:00. The results are shown in Table 15. The two data sets exhibit a good and significant ($p$-value < 0.05) (Montgomery and Runger, 2007) correlation between 01:00 and 18:00, while the correlation decreases for the time slot from 01:00 to 24:00. This is due to the high value of simulated concentrations in late afternoon and evening for cells adjacent to the buildings (Figure 36, right), where the local atmospheric stability reduces air mixing, leading to pollutant accumulation. Moreover, the ARPA stations for air quality monitoring, as required by the European Directive on ambient air quality (E. U., 2008), are not placed very close to buildings. As shown by Tinarelli *et al.* (2009) the representativeness of air quality measurements in urban environment can be deeply affected by atmospheric flow perturbations due to the urban canopy. Consequently, the measured data show a maximum during traffic rush hours (from 06:00 to 09:00, Figure 36, left) and an almost steady trend for the rest of the day.

| **Emitting Source** | **01:00-24:00** | | | **01:00-18:00** | | |
|---|---|---|---|---|---|---|
| | **Site 1** | **Site 2** | **Site 3** | **Site 1** | **Site 2** | **Site 3** |
| **Whole plant** | 0.33 | 0.38 | **0.53** | **0.63** | **0.69** | **0.80** |
| **Auxiliary Devices** | 0.27 | 0.32 | **0.45** | **0.55** | **0.60** | **0.69** |
| **Tri-generation unit** | **0.42** | 0.45 | **0.54** | **0.83** | **0.86** | **0.87** |

*Table 15. Pearson's correlation coefficient comparison between measured data and hourly maximum concentration peaks for the $NO_x$ emission over two time slots: from 01:00 to 00:00 and from 01:00 to 18:00. Boldfaced values indicate statistically significant correlation (p-value<0.05).*

Best correlations are obtained for site 3, since it is less influenced by traffic emissions and is representative of urban background conditions, i.e. also for residential urban areas, as it is the case of the simulation domain. Concerning the contribution of the different sources, the maximum correlation occurs for the tri-generation unit, which operates at constant loading rate throughout the day: given the steady emission rate from this unit stack, the strength of its impact on air quality will be mainly driven by meteorological conditions. On the contrary, the auxiliary devices operate at variable loading rate during the day, with highs in the early morning, and their impact will be significantly affected by their emission rate trend. The correlation shown in Table 15 further improves and maintains its significance if only the time slot from 08:00 to 16:00 is considered ($r$ always larger than 0.85 and $p$-value < 0.05) although in this case the number of data used is limited: in this time slot the auxiliary devices operate at less variable loading rate and atmospheric conditions are more favourable to dispersion. These outcomes confirm the reliability of MSS to simulate the daily evolution of atmospheric dispersion pattern (Tinarelli *et al.*, 2012).

# *Conclusions*

This study investigates the atmospheric impact of pollutant emissions from a power plant, by simulating the airborne dispersion patterns via a Lagrangian particle dispersion model.

The plant, which includes a tri-generation unit and the auxiliary devices, will be installed in the urban area of Modena (central Po valley, Northern Italy), in order to supply the energy demand of the city General Hospital (heat, electricity and cooling system for buildings). Auxiliary devices consist of three conventional boilers and two industrial steam generators that operate in support of the tri-generation unit during periods of higher energy demand and during the tri-generation unit maintenance stops.

The new power plant is designed to replace an existing and obsolete power-plant, which currently provides for thermal energy production of the General Hospital with conventional boilers.

The existing plant emissions show a strong seasonality, with a peak in winter.

As regards new plant, the tri-generator emissions are fairly steady throughout the year, while the auxiliary devices, which operate during high energy demand periods, have higher pollutant emissions in winter season.

Both the power plants are fuelled with methane gas. Hence, being $NO_x$ the most critical pollutant specie for methane-fuelled plant stack emissions, the simulation focused on $NO_x$ emissions.

Primary aim of the study was to compare the current and the future air quality impact scenarios, due to the existing and to the new power plant respectively. The comparison between the total mass flux of pollutants yearly emitted from the existing and from the future power plant showed a higher annual emission for the new plant than for the existing plant. Nevertheless, the impact on local air quality of stack emissions strictly depends on the pollutant dispersion phenomena, which are affected by many factors: the plant stack height, the emitted pollutant flow rate, the meteorology and the interactions between the emitted pollutant plume and the urban canopy (buildings).

The city of Modena experiences high concentration levels of atmospheric pollutants due to a strong pressure by anthropogenic emissions, e.g. manufacturing activities, vehicular traffic and household heating system, along with topographic and meteorological conditions unfavourable to pollutant dispersion: calm wind events, thermal inversions and strong atmospheric stability.

The simulation of $NO_x$ dispersion was performed by the software package ARIA INDUSTRY that includes: the dispersion model SPRAY, the diagnostic meteorological model MINERVE and the turbulence model SURFPRO. SPRAY is a Lagrangian stochastic model for the simulation of the dispersion of passive pollutants in complex terrain under non-homogenous conditions.

The dispersion patterns of $NO_x$ stack emissions were simulated both in the current and future scenario, by using winter 2010 as test period. Meteorological dataset was provided by courtesy of the Osservatorio Geofisico of Modena and Reggio Emilia University (Modena, Italy) and Local Environmental Protection Agency (ARPA).

Local scale simulation results showed that $NO_x$ emissions from the existing power may lead to $NO_x$ local ground concentration, in the first atmospheric layer, 10 m deep, close to the regulatory limits and significantly higher than the concentration due to the new plant emissions. The tri-generator emissions do not significantly affect local air quality at the ground while the impact from the auxiliary devices, results relevant at the ground, mainly because of the low exit velocity of the exhaust gas from their stacks.

Since the plant is placed within a residential urban area, pollutant dispersion phenomena are more influenced by the interactions of the emitted plume with buildings, than by local-scale meteorology. Therefore, in order to assess more in detail the atmospheric impact from the new power plant, by focusing on the urban zone more susceptible to the stack emissions, the simulation of pollutant dispersion at urban micro-scale was performed by means of the Micro-SWIFT-SPRAY.

Micro-SWIFT and Micro-SPRAY codes, which were developed as two advanced versions of MINERVE and SPRAY models, reproduce air circulation fields and pollutant dispersion patterns in presence of buildings, i.e. by taking into account turbulent perturbations due to the urban canopy.

Two simulations were performed over two daily periods (24 hours), which were chosen by analysing the winter 2010 meteorological dataset. The goal was to identify the different role of urban obstacles in affecting dispersion patterns under different meteorological scenarios, depending on whether low or moderate wind conditions occur.

When atmospheric conditions are unfavourable for dispersion (January $14^{th}$), pollutant plumes tend to stagnate and merge in the surroundings of the sources. Under the February $6^{th}$ meteorological scenario, when windy conditions occur, plumes appear more stretched along wind prevailing direction and building influence on air flow becomes significant: a skimming flow canyon phenomenon causes a local increase of $NO_x$ concentration.

However, the simulated $NO_x$ concentrations due to plant emissions are much lower than regulatory limits and also than atmospheric $NO_x$ observations in Modena, where near-ground air quality is strongly affected by traffic emissions. The qualitative comparison carried out on January $14^{th}$ between hourly patterns of maximum concentration peaks and measured data in urban environment show a good correlation, especially during daylight hours, indicating the MSS reliability in simulating both the atmospheric mixing conditions and the dispersion patterns within an urban environment.

Finally, the study shows how switching from the existing to the new plant will improve the air quality in the surroundings of the power plant, where its emission plume disperses. Furthermore, the present study stresses the role of the plume rise in reducing the emitted pollutant impact at ground level, also in meteorological condition favourable to pollutant accumulation in atmosphere: the tri-generation unit contribution to ground concentration is lower because of its higher stack height and higher exhaust gas velocity. This result leads to recommend stack designs increasing the plume rise, notwithstanding the raise in plant costs. In addition, the case study confirms the effective reduction in Green House Gas (GHG) emission in atmosphere switching from the existing to the new plant, due to the Combined Heat and Power (CHP) self-production of electric power.

The micro-scale simulation shows that the combined effect of urban obstacles with stacks emissions may cause pollutant stagnation in urban canyons, especially in windy conditions when, on the contrary, more favourable conditions for pollutant dispersion should be expected.

European Directives (E.U., 2008) encourage air quality modelling in order to provide supplemental information to air quality monitoring, and much more comprehensive information as regards public exposure, supports identification of sources and future projections based on different measures scenarios. Use of modelling has been also developed under specific initiatives such as HARMO (HARMO, 2015). A Forum for Air Quality Modelling (FAIRMODE, 2015) of modellers and users has been established to support the widespread and harmonised use of models through model validation and intercomparison exercises (E. C., 2015).

Furthermore, air quality modelling gives a relevant support to public authorities within atmospheric impact assessment and authorization procedures for atmospheric emissions.

# References

**Papers on journals, books and conference proceedings**


Agugiaro G. (2014). I modelli digitali 3D di città come hub informativo per simulazioni energetiche a scala urbana, *Proceedings of the Italian Society of Remote Sensing (ASITA) XVIII National Conference*, 14th-16th October 2014, Florence, Italy. (in Italian)

Anfossi D., Tinarelli G., Trini Castelli S., Nibart M., Olry C., Commanay J. (2010). A new Lagrangian particle model for the simulation of dense gas dispersion. *Atmospheric Environment*, Vol. 44, No. 6, pp. 753-762.

Anfossi D., Desiato F., Tinarelli G., Brusasca G., Ferrero E., Sacchetti D. (1998). TRANSALP 1989 experimental campaign-I. Simulation of a tracer experiment with Lagrangian particle models. *Atmospheric Environment*, Vol. 32, No. 7, pp. 1157-1166.

Anfossi D., Ferrero E., Sacchetti D., Trini Castelli S. (1997). Comparison among empirical probability density functions of the vertical velocity in the surface layer based on higher order correlations. *Boundary Layer Meteorology*, Vol. 82, No. 2, pp. 193-218.

Anfossi D., Ferrero E., Tinarelli G., Alessandrini S. (1996). A simplified version of correct boundary conditions for skewed turbulence in Lagrangian Particle Models. *Atmospheric Environment*, Vol. 31, No. 2, pp. 301-308.

Anfossi D., Ferrero E., Brusasca G., Marzorati A., Tinarelli G. (1993). A simple way of computing buoyant plume rise in Lagrangian stochastic dispersion models. *Atmospheric Environment*, Vol. 27A, No. 9, pp. 1443-1451.

Anfossi D. (1985). Analysis of plume rise data from five TVA steam plants. *Journal of Climate and Applied Meteorology*, Vol. 24, pp. 1225-1236.

Anfossi D., Bonino G., Bossa F., Richiardone R. (1978). Plume rise from multiple sources: a new model. *Atmospheric Environment*, Vol. 12, No. 9, pp. 1821-1826.

Armanasco F., Colombo L. P. M., Lucchini A., Rossetti A. (2012). Techno-economic evaluation of commercial cogeneration plants for small and medium size companies in the Italian industrial and service sector. *Applied Thermal Engineering*, Vol. 48, pp. 402-413.

Armand P., Commanay J., Nibart M., Albergel A., Achim P. (2007): 3D simulations of pollutant atmospheric dispersion around the buildings of an industrial site comparison of Mercure CFD approach with Micro-Swift-Spray semiempirical approach. *Proceedings of the 11th International*

*Conference on Harmonisation within Atmospheric Dispersion Modelling for Regulatory Purposes*, July 2nd-5th, 2007, Cambridge, UK.

Banks D., Meroney R. N. (2001). The applicability of quasi-steady theory to pressure statistics beneath roof-top vortices. *Journal of Wind Engineering and Industrial Aerodynamics*, Vol. 89, pp. 569-598.

Bigi A., Ghermandi G., Harrison R. M. (2012). Analysis of the air pollution climate at a background site in the Po Valley. *Journal of Environmental Monitoring*, Vol. 2, No. 14, pp. 552-563.

Božnar M. Z., Mlakar P., Grašič B., Tinarelli G. (2012). Environmental impact assessment of a new thermal power plant Šoštanj Block 6 in highly complex terrain. *International Journal of Environmental Pollution*, Vol. 48, Nos. 1/2/3/4, pp. 136-144.

Briggs G. A. (1984). *Plume rise and buoyancy effects.* Atmospheric Science and Power Production, D. Randerson Ed., DOE/TIC-27601, US Department of Energy.

Briggs G. A. (1973). *Diffusion estimation for small emissions, in environmental research laboratories*. Annual Report of the Air Resources Atmospheric Turbulence and Diffusion Laboratory of the National Oceanic and Atmospheric Administration (NOAA), USAEC ATDL-106 NOAA.

Brusasca G., Tinarelli G., Anfossi D., Ferrero E., Tampieri F., Trombetti F. (1994). Development of a Lagrangian Stochastic Model for Dispersion in Complex Terrain. *Air Pollution Modelling and its Application X*, NATO-Challenges of modern Society, Vol. 18, pp. 329-337.

Cantore G. (1999). *Macchine*. Esculapio, Bologna, Italy, pp. 328. (in Italian)

Carson D. J. (1973). The development of a dry inversion-capped convectively unstable boundary layer. *Quarterly Journal of the Royal Meteorological Society*, Vol. 99, No 421, pp. 450-467.

Caruso G., De Santoli L., Mancini F., Caricchia M., Giamminuti F., Sodani P. (2006). Aspetti energetici e ambientali di un impianto di trigenerazione. *Proceedings of the 24th National Conference on Heat Transfer*, 21st-23rd June 2006, Naples, Italy. (in Italian)

Chandrasekar A., Philbrick C. R., Clark R., Doddridge B., Georgopoulos P. (2003). Evaluating the performance of a computationally efficient MM5/CALMET system for developing wind field inputs to air quality models. *Atmospheric Environment*, Vol. 37, pp. 3267-3276.

Cho H., Mago P. J., Luck R., Chamra L. M. (2009). Evaluation of CCHP systems performance based on operational cost, primary energy consumption, and carbon dioxide emission by utilizing an optimal operation scheme. *Applied Energy*, Vol. 86, No. 12, pp. 2540-2549.

Comini G., Cortella G., Croce G. (2005). *Energetica Generale*. S.G.E., Padova, Italy, pp. 446. (in Italian)

Cox R. M., Sontowski J., Dougherty C. M. (2005). An evaluation of three diagnostic wind models (CALMET, MCSCIPUF, and SWIFT) with wind data from the Dipole Pride 26 field experiments. *Meteorological Applications*, Vol. 12, No. 4, pp. 329-341.

Cox R. M., Sontowski J., Fry R. N., Dougherty C. M., Smith T. J. (1998). Wind and diffusion modelling for complex terrain. *Journal of Applied Meteorology*, Vol. 37, No. 10, pp. 996-1009.

Dharmadhikari S. (1997). Consider tri-generation techniques for process plants. *Hydrocarbon Processing*, Vol. 76, No. 7, pp. 91-100.

Deserti M., Savoia E., Cacciamani C., Golinelli M., Kerschbaumer A., Leoncini G., Selvini A., Paccagnella T., Tibaldi S. (2001). Operational meteorological pre-processing at Emilia Romagna ARPA meteorological service as a part of a decision support. *International Journal of Environmental Pollution*, Vol. 16, No. 1/2/3/4/5/6, pp. 571–582.

Desiato F., Finardi S., Brusasca G., Morselli M. G. (1998). TRANSALP 1989 experimental campaign-I: simulation of 3D flow with diagnostic wind field models. *Atmospheric Environment*, Vol. 32, No. 7, pp. 1141-1156.

Du S. (1997). Universality of the Lagrangian velocity structure function constant ($C_0$) across different kinds of turbulence. *Boundary Layer Meteorology*, Vol. 83, No. 2, pp. 207-219.

Ferreira A. C., Nunes M. L., Teixeira S., Martins L. B. (2014). Technical-economic evaluation of a cogeneration technology considering carbon emission savings. *International Journal of Sustainable Energy Planning and Management*, Vol. 2, pp. 33-46.

Ferrero L., Riccio A., Perrone M. G., Sangiorgi G., Ferrini B. S., Bolzacchini E. (2011). Mixing height determination by tethered balloon-based particle soundings and modelling simulations. *Atmospheric Research*, Vol. 102, No. 1/2, pp. 145-156.

Ferrero E., Alessandrini S. (2009). A hybrid Lagrangian Eulerian particle model for reacting pollutant dispersion in non-homogeneous non-isotropic turbulence. *Physica A: Statistical Mechanics and its Applications*, Vol. 388, No. 8, pp. 1375-1387.

Ferrero E., D. Anfossi (1998). Comparison of PDFs, closure schemes and turbulence parameterizations in Lagrangian stochastic models. *International Journal of Environmental Pollution*, Vol. 9, No. 4, pp. 384-410.

Ferrero E., Anfossi D., Tinarelli G., Trini Castelli S. (1997). An intercomparison of two turbulence closure schemes and four parameterizations for stochastic dispersion models, *Il Nuovo Cimento*, Italian Society of Physics, Vol. 20, No. 3, pp. 315-329.

Finardi S., Tinarelli G., Faggian P., Brusasca G. (1998). Evaluation of different wind field modelling techniques for wind Energy applications over complex topography. *Journal of Wind Engineering & Industrial Aerodynamics*, Vol. 74, pp. 283-294.

Finzi G., Pirovano G., Volta M. L. (2001). *Gestione della qualità dell'aria*. Modelli di simulazione e previsione. Mc Graw-Hill, pp. 400.

Gariazzo C., Pelliccioni A., Bogliolo M. P., Scalisi G. (2004). Evaluation of a Lagrangian Particle Model (SPRAY) to Assess Environmental Impact of an Industrial Facility in Complex Terrain. *Water Air and Soil Pollution*, Vol. 1, No. 155, pp. 137-158.

Gariazzo C., Tinarelli G., Demichela A. M., Pellicioni A., Amicarelli A. (2008): Analisi delle conseguenze su microscala di rilasci di sostanze tossiche da impianti industriali: confronto dei risultati ottenuti con modelli Lagrangiani a particelle, CFD e Gaussiani. *Proceedings of the 6th Conference on risk assessment and management in the civil and industrial settlements*, 14th-16th October 2008, Pisa, Italy. (in Italian)

Gariazzo C., Papaleo V., Pelliccioni A., Calori G., Radice P., Tinarelli G. (2007). Application of a Lagrangian particle model to assess the impact of harbour, industrial and urban activities on air quality in the Taranto area, Italy. *Atmospheric Environment*, Vol. 41, No. 30, pp. 6432-6444.

Gariazzo C., Pelliccioni A., Bogliolo M. P., Scalisi G. (2004). Evaluation of a Lagrangian Particle Model (SPRAY) to Assess Environmental Impact of an Industrial Facility in Complex Terrain. *Water Air and Soil Pollution*, Vol. 1, No. 155, pp. 137-158.

Geai P. (1987). *Methode d'interpolation et de reconstitution tridimensionelle d'un champ de vent: Le code d'analyse objective MINERVE*. Report ARD-AID: E34-E11, EDF, Chatou, France. (in French)

Ghermandi G., Teggi S., Fabbi S., Bigi A., Zaccanti M. (2015). Tri-generation power plant and conventional boilers: Pollutant flow rate and atmospheric impact of stack emissions. *International Journal of Environmental Science and Technology*, Vol. 12, No. 2, pp. 693-704.

Ghermandi G., Teggi S., Fabbi S., Bigi A., Zaccanti M. (2014). Micro scale simulation of atmospheric emissions from power-plant stack in the Po Valley. *Atmospheric Pollution Research*, DOI: 10.5094/APR.2015.042, *available on line 05 December 2014*, pp. 1-7.

Ghermandi G., Teggi S., Fabbi S., Bigi A., Zaccanti M. (2013). From local-scale to micro-scale assessment of the atmospheric impact of the pollutant plume emitted from a power-plant stack. *Proceedings of the 15th International Conference on Harmonisation within Atmospheric Dispersion Modelling for Regulatory Purposes*, 6th-9th May 2013, Madrid, Spain.

Ghermandi G., Teggi S., Fabbi S., Bigi A., Cecchi R. (2012). Model comparison in simulating the atmospheric dispersion of a pollutant plume in low wind conditions. *International Journal of Environmental Pollution*, Vol. 48, No. 1/2/3/4, pp. 69-77.

Gifford F. A. (1961). Use of Routine Meteorological Observations for Estimating Atmospheric Dispersion. *Nuclear Safety*, Vol. 2, No. 4, pp. 47-51.

Green A. E., Singhal R. P., Venkateswar R. (1980). Analytic extensions of the Gaussian Plume Model. *Journal of the Air Pollution Control Association*, Vol. 30, No. 7, pp. 773-776.

Hanna S. R., Chang J. C. (1982). Boundary-layer parameterizations for applied dispersion modelling over urban areas. *Boundary-Layer Meteorology*, Vol. 58, No. 3, pp. 229-259.

Hanna S., White J., Trolier J., Vernot R., Brown M., Gowardhan A., Kaplan H., Alexander Y., Moussafir J., Wang Y. S., Williamson C., Hannan J., Hendrick E. (2011). Comparisons of JU2003 observations with four diagnostic urban wind flow and Lagrangian particle dispersion models. *Atmospheric Environment*, Vol. 45, pp. 4073-4081.

Hanna S. R. (1982). *Applications in air pollution modelling*, Atmospheric turbulence and air pollution modelling, Ed. by Nieuwstadt S.T.M. and van Dop H., Reidel, pp. 275-310.

Holtslag A. A. M., Van Ulden A. P. (1983). A simple scheme for daytime estimates of the surface fluxes from routine weather data. *Journal of Applied Meteorology and Climatology*, Vol. 22, No. 4, pp. 517-529.

Homicz G. F. (2002). *Three-Dimensional Wind Field Modeling: a Review*, Edited by Sandia National Laboratories Albuquerque, NM, and Livermore, CA, U.S.A.

Hotchkiss R. S., Harlow F. H. (1973). *Air pollution transport in street canyons*. EPA-R4-73-029.

Houghton J. T., Ding Y., Griggs D. J., Noguer M., van der Linden P. J., Dai X., Maskell K., Johnson C. A. (2001). *Climate change 2001: the scientific basis*. Cambridge University Press, Cambridge, pp. 82.

Hunter L. J., Johnson G. T., Watson I. D. (1992). An investigation of three-dimensional characteristics of flow regimes within the urban canyon. *Atmospheric Environment*, Vol. 26B, No. 4, pp. 425-432.

Irwin J. S. (1983). Estimating Plume Dispersion-A Comparison of Several Sigma Schemes. *Journal of Climate and Applied Meteorology*, Vol. 22, pp. 92-114.

Irwin J. S. (1979). *Estimating Plume Dispersion, a recommended generalized scheme.* U. S. Environmental Protection Agency (EPA), Washington, D.C., EPA/600/J-79/022.

Jackson B., Chau D., Gurer K., Kaduwela A. (2006). Comparison of ozone simulations using MM5 and CALMET/MM5 hybrid meteorological fields for the July/August 2000 CCOS episode. *Atmospheric Environment*, Vol. 40, pp. 2812-2822.

Kaplan H., Olry C., Moussafir J., Oldrini O., Mahe F., Albergel A. (2014). Chemical reactions at street scale using a Lagrangian particle dispersion model. *International Journal of Environment and Pollution*, Vol. 55, No. 1/2/3/4, pp. 157 – 166.

Kaplan H., Dinar N. (1996). A Lagrangian dispersion model for calculating concentration distribution within a built-up domain. *Atmospheric Environment*, Vol. 30, No. 24, pp. 4197-4207.

Kolmogorov A. N. (1941). The local structure of turbulence in incompressible viscous fluid for very large Reynolds numbers. *Proceedings of the USSR Academy of Sciences*, Vol. 30, pp. 299-303.

Krauß T., Reinartz P. (2009). Refinement of Urban Digital Elevation Models from Very High Resolution Stereo Satellite Images. *Proceedings of the International Society for Photogrammetry and Remote Sensing (ISPRS) Hannover Workshop 2009, High-Resolution Earth Imaging for Geospatial Information*, June 2nd-5th, 2009, Hannover, Germany.

Levy J. I., Spengler J. D. (2002). Modelling the benefits of power plant emission controls in Massachusetts. *Journal of the Air and Waste Management Association*, Vol. 52, No. 1, pp. 5-18.

Louis J. F. (1979). A parametric model of vertical eddy fluxes in the atmosphere. *Boundary-Layer Meteorology*, Vol. 17, No. 2, pp. 187-202.

Luhar A. K., Britter R. E. (1989). A random walk model for dispersion in inhomogenous turbulence in a convective boundary layer. *Atmospheric Environment*, Vol. 23, pp. 1911-1924.

Mac Lain (1976). Two dimensional interpolation from random data. *The Computer Journal*, Vol. 19, No. 2, pp. 178-181.

McDonough J. M. (2007). *Introductory lectures on turbulence; Physics, Mathematics and Modeling*. Departments of Mechanical Engineering and Mathematics University of Kentucky, pp. 174.

Meunier F. (2002). Co- and tri-generation contribution to climate change control. *Applied Thermal Energy*, Vol. 22, No. 6, pp. 703-718.

Monin A. S., Yaglom A. M. (1971). *Statistical fluid mechanics: mechanics of turbulence*, Vol. 2, MIT Press, Cambridge, UK, pp. 874.

Montgomery D. C., Runger G. C. (2007). *Applied Statistics and Probability for Engineers*, John Wiley & Sons Inc., USA, pp. 768.

Moussiopoulos N., Flassak T., Knittel G. (1988). A refined diagnostic wind model. *Proceedings of the Envirosoft 88, 2nd International Conference*, Porto Carras, Greece, September 1988.

Nieuwstadt, F. T. M. (1980) Application of mixed-layer similarity to the observed dispersion from a ground-level source. *Journal of Applied Meteorology*, Vol. 19, pp. 157-162.

Oke T. R. (1987). *Boundary Layer Climates*. Routledge, Cambrigde, UK, pp. 435.

Pasquill F. (1961). The estimation of the dispersion of windborne material. *The Meteorological Magazine*, Vol. 90, No. 1063, pp. 33-49.

Pehnt M. (2008). Environmental impacts of distributed energy systems: the case of micro cogeneration. *Environmental Science Policy*, Vol. 11, No. 1, pp. 25-37.

Pernigotti D., Georgieva E., Thunis P., Bessagnet B. (2012) Impact of meteorology on air quality modelling over the Po valley in northern Italy. *Atmospheric Environment*, Vol. 51, pp. 303-310.

Prandtl L. (1925). Bericht űber Untersuchungen zur ausgebildeten Turbulenz. *Zeitschrift für Angewandte Mathematik und Mechanik*, Vol. 5, pp. 136-139. (in German)

Ratto C. F., Festa R., Romeo C. (1994). Mass consistent models from wind fields over complex terrain: the state of art. *Environmental Software*, Vol. 9, No. 4, pp. 247-268.

Reynolds O. (1895). On the dynamical theory of incompressible viscous fluids and the determination of the criterion. *Philosophical Transaction of the Royal Society of London*, Vol. 186, pp. 123-164.

Rockle R. (1990). *Bestimmung der Stomungsverhaltnisse im Bereich komplexer Bebauungsstrukturen*. Ph. D. thesis, Vom Fachbereich Mechanik, der Technischen Hochschule, Darmstadt, Germany. (in German)

Rodean H. C. (1996). Stochastic Lagrangian Models of Turbulent Diffusion. *Monographs of American Meteorological Society (AMS)*, Vol. 26, pp. 84.

Schicktanz M. D., Wapler J., Henning H. M. (2011). Primary energy and economic analysis of combined heating, cooling and power systems. *Energy*, Vol. 36, No. 1, pp. 575-585.

Scire J. S., Robe F. R., Fernau M. E., Yamartino R. J. (2000). *A User Guide for the CALMET Meteorological Model (Version 5)*. Earth Tech Inc., Concord, MA, U.S.A.

Slawson P. R., Csanady G. T. (1971). The effect of atmospheric conditions on plume rise. *Journal of Fluid Mechanics*, Vol. 47, No. 1, pp. 33-49.

Song C. K., Kim C. H., Lee S. H., Park S. U. (2003). A 3-D Lagrangian particle dispersion model with photochemical reactions. *Atmospheric Environment*, Vol. 37, No. 33, pp. 4607-4623.

Sozzi R. (2003). *La micrometeorologia e la dispersione degli inquinanti in aria*. Centro tematico Nazionale Atmosfera Clima Emissioni. (in Italian)

Stull R. B. (1989). *An introduction to Boundary layer meteorology*. Springer Science & Business Media, pp. 666.

Sutton O. G. (1947). The problem of diffusion in the lower atmosphere. *Quarterly Journal of the Royal Meteorological Society*, Vol. 73, pp. 257-276**.**

Taylor G. I. (1921). Diffusion by Continuous Movements. *Proceedings of the London Mathematical Society*, Vol. 20, pp. 196-211.

Tennekes H. (1979). The exponential Lagrangian correlation function and turbulent diffusion in the inertial subrange. *Atmospheric Environment*, Vol. 13, No. 11, pp. 1565-1567.

Thomson D. J. (1987). Criteria for the selection of stochastic–models of particle trajectories in turbulent flows. *Journal of Fluid Mechanics*, Vol. 180, pp. 529-556.

Tinarelli G., Mortarini L., Trini Castelli S., Carlino G., Moussafir J., Olry C., Armand P., Anfossi D. (2012). Review and validation of microspray, a Lagrangian particle model of turbulent dispersion. *Lagrangian Modeling of the Atmosphere*, Geophysical Monograph Series, 200, edited by American Geophysical Union (AGU), Grindelwald, Switzerland, pp. 311-327.

Tinarelli G., Piersanti A., Radice P., Clemente M., De Maria R. (2009). Microscale modelling simulations for the site characterization of air quality stations in an urban environment. *Radiation Protection Dosimetry*, Vol. 137, Nos. 3-4, pp. 294-299.

Tinarelli G., Anfossi D., Trini Castelli S., Albergel A., Ganci F., Belfiore G., Moussafir J. (2008). Development of a Lagrangian Particle Model for Dense Gas Dispersion in Urban Environment. *Air Pollution Modeling and Its Application XIX*, NATO Science for Peace and Security Series Series C: Environmental Security, pp. 28-36.

Tinarelli G., Anfossi D., Bider M., Ferrero E., Trini Castelli S. (2000). A new high performance version of the Lagrangian Particle Dispersion Model SPRAY, some case studies. *Air Pollution Modelling and its Application XIII*, edited by Grying S. E. and Batchvarova E., Kluver Academic plenum Publishers.

Tinarelli G., Anfossi D., Brusasca G., Ferrero E., Giostra U., Morselli M. G., Moussafir J., Tampieri F., Trombetti F. (1994). Lagrangian Particle Simulation of Tracer Dispersion in the Lee of a schematic Two-Dimensional Hill. *Journal of Applied Meteorology*, Vol. 33, No. 6, 744-756.

Trini Castelli S., Mortarini L., Tinarelli G., Anfossi D. (2010). Development and application of the microscale Lagrangian particle dispersion model MicroSpray for the simulation of hydrogen accidental releases. *Proceedings of the 13$^{th}$ International Conference on Harmonisation within Atmospheric Dispersion Modelling for Regulatory Purposes*, 1$^{st}$-4$^{th}$ June, Paris, France.

Trini Castelli S., Anfossi D., Ferrero E. (2003). Evaluation of the environmental impact of two different heating scenarios in urban area. *International Journal of Environmental Pollution*, Vol. 20, Nos. 1/2/3/4/5/6, pp. 207-217.

Turner D. B. (1967). *Workbook of Atmospheric Dispersion Estimates*, PHS Publ. No. 999, AP-26, Cincinnati, OH, pp. 84.

Vardoulakis S., Fisher B. E. A., Pericleous K., Gonzalez-Flesca N. (2003). Modelling air quality in street canyons: A review. *Atmospheric Environment*, Vol. 37, No. 2, pp. 155-182.

Venkatram A. (1980): Estimating the Monin-Obukhov length in the stable boundary layer for dispersion calculations. *Boundary-Layer Meteorology*, Vol. 19, No. 4, pp. 481-485.

Weil J. C. (1990). A diagnosis of the asymmetry in top-down and bottom-up diffusion using a Lagrangian stochastic model. *Journal of Atmospheric Science*, Vol. 47, No. 4, pp. 501-515.

Wilson D. J. (1979). Flow pattern over flat-roofed buildings and application to exhaust stack design, *Transactions of the American Society of Heat, Refrigeration and Air Conditioning Engineering (ASHRAE)*, Vol. 28, No. 2, pp. 284-295.

Wright N. G., Easom G. J. (2003). Non-linear k-e turbulence model results for flow over a building at full-scale. *Applied Mathematical Modelling*, Vol. 27, No. 12, pp. 1013-1033.

Yamartino R. J., Wiegard, G. (1986). Development and evaluation of simple models for the flow, turbulence and pollutant concentration fields within an urban street canyon. *Atmospheric Environment*, Vol. 20, No. 11, pp. 2137-2156.

Yim S. H. L., Fung J. C. H., Lau A. K. H., Kot S. C. (2007). Developing a high resolution wind map for a complex terrain with a coupled MM5/CALMET system. *Journal of Geophysical Research: Atmospheres*, Vol. 112, No. D5.

**Regulations**

E. U. (2009). Directive 2009/29/EC of the European Parliament and of the Council of 23 April 2009 amending Directive 2003/87/EC so as to improve and extend the greenhouse gas emission allowance trading scheme of the Community (Text with EEA relevance). Official Journal of the European Union, L Serie, L140/63-L 140/87.

E. U. (2008). Directive 2008/50/EC of the European Parliament and of the Council of 21 May 2008 on Ambient Air Quality and Cleaner Air for Europe, Official Journal of the European Union, L152/1–L152/44.

E. U. (2004). Directive 2004/8/EC of the European Parliament and of the council of 11 February 2004 on the promotion of cogeneration based on a useful heat demand in the internal Energy market and amending Directive 92/42/EEC. Official Journal of the European Union, L Serie, L52/50-L52/60.

D. Lgs. 3/4/2006 n. 152, Norme in materia ambientale, Official Gazzette of the Italian Republic 14-4-2006, n. 88. (in Italian)

D. Lgs. 8/2/2007 n. 20, Attuazione della direttiva 2004/8/CE sulla promozione della cogenerazione basata su una domanda di calore utile nel mercato interno dell'energia, nonché modifica alla direttiva 92/42/CEE, Official Gazzette of the Italian Republic 6-3-2007, n. 54. (in Italian)

**Technical Reports**

Aria Technologies (2010). SWIFT Wind Field Model, General Design Manual.

Aria Technologies (2001). MINERVE Wind Field Model - Version 7.0, User's Manual.

Arianet (2010). SPRAY5 - General Description and User's Guide.

Arianet (2008). Emission Manager User's guide.

Arianet (2007). SPRAY 3.1 User's guide.

Arianet (2006). SURFPRO - Version 2.2.10, User's guide.

National Agency for Electric Energy (ENEL, 2010). Rapporto ambientale ENEL 2010.

Local Office for Cadastre and Topography (E. R., 2011). Database topografico 2011, regione Emilia-Romagna, versione 0.1.

**Web references**


ENVI (2004) User's guide, Version 4.1,
http://aviris.gl.fcen.uba.ar/Curso_SR/biblio_sr/ENVI_userguid.pdf
Last access: 11th March 2015.

ESRI, ArcGIS Resources, http://resources.arcgis.com/en/home/.
Last access: 10th March 2015.

European Environmental Agency (EEA, 2015a), Corine Land Cover,
http://www.eea.europa.eu/publications/COR0-landcover.
Last access 10th February 2015.

European Environmental Agency (EEA, 2015b), Energy efficiency in transformation (ENER 011),
http://www.eea.europa.eu/data-and-maps/indicators/en19-efficiency-of-conventional-thermal-1.
Last access: 9th March 2015.

European Commission (E. C.), Implementation of ambient air quality legislation.
http://ec.europa.eu/environment/air/quality/legislation/assessment.htm.
Last access: 11th March 2015.

European Topic Centre on Air Pollution and Climate Change Mitigation (ETC/ACM),
http://acm.eionet.europa.eu/databases/MDS/index_html.
Last access: 11th March 2015.

Forum Air Quality Modelling in Europe (FAIRMODE), http://fairmode.jrc.ec.europa.eu/
Last access: 11th March 2015.

HARMO, Initiative on "Harmonisation within Atmospheric Dispersion Modelling for Regulatory Purposes". http://www.harmo.org/default.asp.
Last access: 12th March 2015.

Intergovernmental Panel on Climate Change (IPCC), 2007: Contribution of Working Group III to the Fourth Assessment Report of the Intergovernmental Panel on Climate Change,
http://www.ipcc.ch/publications_and_data/ar4/wg3/en/ch4s4-3-5.html.
Last access: 3rd March 2015.

Italian Major Institute for Environmental Research and Protection (ISPRA),
http://www.isprambiente.gov.it/it/temi/biodiversita/documenti/europea-e-mediterranea/corine-land-cover-clc.
Last access: 10th February 2015.

Wikipedia: LAI index, http://en.wikipedia.org/wiki/Leaf_area_index.
Last access: 2nd March 2015.

# Acknowledgements

I express my sincere gratitude to my tutor Professor Grazia Ghermandi, who gave me the opportunity to undertake this research, to Professor Sergio Teggi, to my co-tutor Engineer Alessandro Bigi, to Engineer Sara Fabbi and to Luca Lombroso for the technical support in computational operations, language revising, meteorological data providing and managing.

Emission data about the studied plants are by courtesy of Local Health Service Agency (AUSL) of Modena “Policlinico” and by CPL Concordia group.

Meteorlological data are by courtesy of Osservatorio Geofisico of Modena and Reggio Emilia University and by Idro-Meteorological Service of Local Environmental Protection Agency (ARPA Emilia-Romagna).